UNIVERSITY OF GENOA, ITALY

DITEN - Department of Electrical, Electronics and Telecommunication Engineering and Naval Architecture

Ph.D. in Science and Technology for Electronic and Telecommunication Engineering - Cycle XXXIII (2017-2020)

Novel Approaches to the Representation and Analysis of 3D Segmented Anatomical Districts

Ph.D. Thesis

Tutor: Dr. Michela Spagnuolo
Tutor: Dr. Giuseppe Patanè
Tutor: Prof. Silvana Dellepiane

Ph.D. Candidate: Martina Paccini

Coordinator of the Ph.D. Course: Prof. Mario Marchese

Abstract

Nowadays, image processing and 3D shape analysis are an integral part of clinical practice and have the potentiality to support clinicians with advanced analysis and visualization techniques. Both approaches provide visual and quantitative information to medical practitioners, even if from different points of view. Indeed, shape analysis is aimed at studying the morphology of anatomical structures, while image processing is focused more on the tissue or functional information provided by the pixels/voxels intensities levels. Despite the progress obtained by research in both fields, a junction between these two complementary worlds is missing. When working with 3D models analyzing shape features, the information of the volume surrounding the structure is lost, since a segmentation process is needed to obtain the 3D shape model; however, the 3D nature of the anatomical structure is represented explicitly. With volume images, instead, the tissue information related to the imaged volume is the core of the analysis, while the shape and morphology of the structure are just implicitly represented, thus not clear enough.

The aim of this Thesis work is the integration of these two approaches in order to increase the amount of information available for physicians, allowing a more accurate analysis of each patient. An augmented visualization tool able to provide information on both the anatomical structure shape and the surrounding volume through a hybrid representation, could reduce the gap between the two approaches and provide a more complete anatomical rendering of the subject.

To this end, given a segmented anatomical district, we propose a novel mapping of volumetric data onto the segmented surface. The grey-levels of the image voxels are mapped through a volume-surface correspondence map, which defines a grey-level texture on the segmented surface. The resulting texture mapping is coherent to the local morphology of the segmented anatomical structure and provides an enhanced visual representation of the anatomical district. The integration of volume-based and surface-based information in a unique 3D representation also supports the identification and characterization of morphological landmarks and pathology evaluations.

The main research contributions of the Ph.D. activities and Thesis are:

- *the development of a novel integration algorithm that combines surface-based (segmented 3D anatomical structure meshes) and volume-based (MRI volumes) information. The integration supports different criteria for the grey-levels mapping onto the segmented surface;*
- *the development of methodological approaches for using the grey-levels mapping together with morphological analysis. The final goal is to solve problems in real clinical tasks, such as the identification of (patient-specific) ligament insertion sites on bones from segmented MR images, the characterization of the local morphology of bones/tissues, the early diagnosis, classification, and monitoring of muscle-skeletal pathologies;*
- *the analysis of segmentation procedures, with a focus on the tissue classification process, in order to reduce operator dependency and to overcome the absence of a real gold standard for the evaluation of automatic segmentations;*
- *the evaluation and comparison of (unsupervised) segmentation methods, finalized to define a novel segmentation method for low-field MR images, and for the local correction/improvement of a given segmentation.*

The proposed method is simple but effectively integrates information derived from medical image analysis and 3D shape analysis. Moreover, the algorithm is general enough to be applied to different anatomical districts independently of the segmentation method, imaging techniques (such as CT), or image resolution. The volume information can be integrated easily in different shape analysis applications, taking into consideration not only the morphology of the input shape but also the real context in which it is inserted, to solve clinical tasks. The results obtained by this combined analysis have been evaluated through statistical analysis.

Dedication

A Elisa, che mi ha accompagnato in questo viaggio rimanendo al mio fianco passo dopo passo.
Dico grazie Sai.

I must not fear
fear is the mind killer
when the fear is gone
only I will remain. (F. Herbert)

Acknowledgements

It is difficult to express with proper words what it meant to me being a PhD student. These years clearly represented more than the sole academic experience. During this amazing and challenging journey, I had the opportunity to grow and learn from passionate and valuable people that supported me toward this achievement.

Undoubtedly my special appreciation goes to my principal supervisors. To Dr. Michela Spagnuolo, who gave me this opportunity in the first place, for her encouragement, sincerity, and perseverance even in the hardest times. To Dr. Giuseppe Patanè, who has been a patient mentor, for helping me through the use of the right words at the right time. I would like to thank also Dr. Silvana Dellepiane for her enthusiasm, her availability, and precious advice. Moreover, my appreciation is addressed to Softeco Sismat S.R.L for the technical support during my years of research.

All the colleagues from CNR-IMATI have been the greatest fellows I could hope for and became real friends, able to move away stress and fatigue with sincere and loud laughter. I really enjoyed all our past and present experiences together, looking forward to many other crazy days.

My deepest gratitude goes to my family who accompanied me through all these years. I will always be grateful to my parents for their unconditional love and support in every aspect of my life and for believing in me even when I did not. A sincere thank goes to my brother Filippo, who has always been by my side, and to my sister Costanza, that, from the very first time, has been able to put me back on my feet. I would like to express my sincere appreciation also to Prof. Marina Pizzi, that many times reminded me of the beauty of scientific research. An exceptional thank goes surely to my friends “rattipennughi” that literally, always have my back.

Table of Contents

List of Figures **4**

List of Tables **8**

I Representation & Analysis of 3D Anatomical Districts **9**

Chapter 1 Thesis Overview **10**

1.1 Images and 3D models in medicine 10

1.2 Motivations 11

1.3 Research goals, contributions, and novelties 12

1.3.1 Research questions and goals 13

1.3.2 Research contributions and novelties 15

1.4 Thesis structure 16

1.5 Future directions 17

1.6 Publications 18

Chapter 2 Volume Images and Surface Models Analysis in Radiology **19**

2.1 Introduction 19

2.2 Image segmentation overview 21

2.3 Shape characterization for Semantic Annotation 25

2.3.1 Shape-based characterization: a review in anatomy 26

2.3.2 Image-based characterization 26
2.4 State of the art on anatomical landmark identification 27
2.4.1 3D Shape models for landmarks identification 28
2.4.2 Use of image analysis for landmarks identification 29

Chapter 3 Research Context and Case-Studies **32**
3.1 Data set overview 32
3.2 MRI basics and system 34
3.2.1 Low-field MRI 39
3.2.2 The DICOM standard 42
3.2.3 MRI pixel intensity informative content 43
3.3 The carpal district 45
3.4 Rheumatic pathologies 48

Chapter 4 Grey-levels Mapping **51**
4.1 Aim of the hybrid representation 51
4.2 The bridge data sctucture 53
4.2.1 Surface mesh 53
4.2.2 Volume image 59
4.3 Single vertex correspondence identification algorithm 61
4.4 Texture mapping 64

II Applications and Clinical Studies **67**

Chapter 5 Clinical Applications of Grey-levels Mapping **68**
5.1 Clinical aspects of early diagnosis in rehumatology 68
5.1.1 Ligament insertions 69
5.1.2 Enthesis localization in the case-study 72

5.1.3 Articulation regions 73
5.2 Ligament insertion localization with texture analysis 75
5.3 Articulation region characterization 76
5.3.1 Feature-based carpal characterization 77
5.3.2 Integration of shape and grey-levels analysis results 81
5.4 Clinical aspects of rheumatic pathologies monitoring 83
5.4.1 Image-based erosion identification methods 84
5.4.2 Shape-based erosion identification methods 85
5.5 Comparison of erosion evaluation method on the case-study 86
5.6 Erosion identification integration method 91

Chapter 6 Grey-levels Mapping for Segmentation **97**
6.1 Evaluation and comparison of segmentation methods 97
6.2 Tissue relation with segmented surfaces 101
6.3 Unsupervised segmentation evaluation proposal 103

Chapter 7 Contributions and Future Work **110**
7.1 Thesis contributions to anatomical representation and clinical applications 110
7.2 Research and development directions 114

Bibliography **116**

List of Figures

1.1 Summary of the proposed framework. 12

3.1 Imaging technologies in medicine 33
3.2 Spin and magnetic moment concepts 34
3.3 Net magnetization vector generation and nucleus precession concept 36
3.4 $90°$ RF pulse and relaxation phase 37
3.5 (a) T_1 relaxation time [Rid15], (b) T_2 relaxation time [Rid10]. 38
3.6 MRI spatial encoding 39
3.7 [JKP+19] Spin echo typical acquisition sequence. 40
3.8 [Gib08] DICOM standard multi-document organization. 42
3.9 $T_1 - weighted$ low field MRI of the carpal district. (a) 3D view, (b) 2D slice representation. 44
3.10 $T_1 - weighting$ and $T_2 - weighting$ pixels/voxels intensities in MRI. 45
3.11 Wrist bones. 46
3.12 Wrist movements. 47
3.13 Intrinsic (right) and extrinsic (left) ligaments of the wrist. 48
3.14 Rheumatoid Arthritis anatomical deformation. 49

4.1 Volume rendering (a) and surface rendering (b) of the hand. 52
4.2 Bones surfaces represented as triangular meshses. 53
4.3 Non-manifold edge, vertex and handling 54

4.4 Mesh description methods. (a) Indexed triangle sets option. (b) Toy example of the correspondent mesh. (c) Description of the same mesh through list of triangles. 55

4.5 3D MRI volume. 56

4.6 Analogy between the regular 3D grid describing the volume and the 2D stack of slices composing the volume MRI. 57

4.7 Data structure of the input voxel grid 58

4.8 The main idea of the integration method 59

4.9 Initial visualization: superimposition of the volume image and the surface model. 60

4.10 Vertex-voxel correspondence identification 61

4.11 Surface mapping obtained with the vertex-voxel correspondence metrics: (a) Euclidean mapping, (b) internal mapping, (c) external mapping. 62

4.12 Grey-levels mapping graphical evaluation 63

4.13 Application of the mapping algorithm to the hand district: (a) Euclidean mapping, (b) external mapping, and (c) internal mapping. 64

5.1 [ADD+14] Tissue composition of fibrocartilaginous different zones. 69

5.2 [ADD+14] The four zones of the enthesis on an histological section of a mouse supraspinatus. 70

5.3 Carpal bones relations in wrist movements. 71

5.4 Ligament insertion grey-level analysis 72

5.5 Ligament insertion sites comparison with reference altas 73

5.6 Anatomical landmarks on carpal bones: (a) articulation facets between hamate (yellow) and capitate (pink); (b) hook of hamate, prominent bony feature (orange). 74

5.7 Shadow map descriptor concept 78

5.8 Conceptualisation of the `articulatesWith` relation in the Carpus Ontology on the left, Corresponding visualisation on the 3D model on the right. 79

5.9 Shadow map computation results 80

5.10 Shadow map on the case-study 80

5.11 Articulation areas texture hystograms and visualization 81

5.12 Articulation areas quantitative characterization 82

5.13 Registration process result. (a) Original situation, (b) after centroid translation, (c) final result obtained with ICP. 83
5.14 Erosion localization through distance distribution thresholding 84
5.15 Workflow of texture-based follow-up analysis 85
5.16 3D surface texture changes in follow-up exams 86
5.17 Bone erosion evolution in time 87
5.18 Texture and geometrical follow-up analysis result comparison on the Scaphoid bone 88
5.19 Statistica analysis of grey-levels distribution changes in follow-up exams 89
5.20 Negative texture difference semantic explanation 90
5.21 Pipeline of the follow-up integration method. 91
5.22 Scaphoid bone follow-up analysis of a patient with Rheumatoid Arthritis 92
5.23 Inaccuracies of the registration method (a) with the relative influence on the identification of erosion regions (b). 93
5.24 Erosion localization results in the texture-based approach 94
5.25 Follow-up analysis approaches results comparison 95
5.26 Linear combination integration results 95

6.1 [ZFG08] Calssification of segmentation evaluation methods. 98
6.2 3D segmented surface (red) superimposed to the volume slices: in some regions, the darker tissues constituted by synovial structures and cortical bone lie inside the surface (green arrows). 101
6.3 Cortical tissue localization in relation to the segmented surface 102
6.4 Cumulative histogram of the absolute difference between internal and external mapping 103
6.5 Pieline of the developed unsupervised segementation evaluation method. 104
6.6 Gradient outer estimation mapping 105
6.7 Gradient Euclidean estimation mapping 105
6.8 Cumulative gradient histograms (CGH) results 107
6.9 Average difference values with respect to the quartiles (Qrt) and percentiles (Prt). 108

7.1 Overview of the novel approach 111
7.2 Overview of the developed framework. 114

List of Tables

3.1 Advantages and disadvantages of low-field MRI scanning systems. 41

5.1 Bone-based properties: a list of state-of-the-art methods. 77

Part I

Representation & Analysis of 3D Anatomical Districts

Chapter 1

Thesis Overview

1.1 Images and 3D models in medicine

Medical imaging is a broad term used to define the technologies which permit the visualization of the human body. Thanks to the information content brought by images, imaging techniques have been extensively used for diagnosis, monitoring, and treatment purposes. Technological development brought the creation and improvement of different types of imaging procedures. Namely, medical images can be categorized into two main classes: *morphological images*, which permit to observe the internal composition of the human body, and *functional images*, which provide information on the functioning principle of the organs.

In both cases, images are created by the interaction of a form of energy with the anatomical structures, or human body. This interaction results in a physical quantity that must reproduce, with its spatio-temporal distribution, the distribution of other physical quantities in the structure (e.g. density, acoustic impedance, or composition of the tissues). For this reason, depending on the form of energy and the interaction studied, the image will bring different informative content since it will provide measures of a distinct physical property of the structure. As a result, each image will be a partial representation of reality, no matter the technology that provided it. [CDV12]

In recent years, technological innovation has permitted the development of 3D imaging, able to obtain not only a section of the human body but a series of them, showing a volumetric representation of the structures of interest. Indeed, the intrinsic 3D nature of the body's internal structure can be represented through a stack of cross-sectional images, leading to an increase of information. Such an amount of informative content implies that physicians and radiologists must analyze and interpret a much higher quantity of data with respect to a single 2D slice [WD19]. Unfortunately, abnormalities can be small compared to the overall size of the image, posing the problem of how to navigate and examine the volume image in an efficient way. Indeed, visual-

ization instruments able to highlight pathological evidence, even if small, help the radiologist in the evaluation of volume images and their high quantity of informative content, focusing his/her attention on the most relevant areas.

Along with the development of 3D imaging technologies recent years have seen a huge development of Computer Graphics, Computer Vision, and image processing techniques. Consequently, the reconstruction of the 3D object from images had represented a big source of research also in the medical field. Numerous techniques to extract 3D models from images have been proposed and adapted to the use in medicine and their definition, analysis, and usage in diagnostic processes boosted a relevant amount of research, with many and still open problems.

The main underlying innovation process is related to the possibility of devising the so-called *3D Patient-Specific Models* (3D PSMs), which are computational reconstructions of the anatomy, mirroring accurately the patient's organs in the 3D space, with the aim to support digital and complete simulations of the patient's clinical state. The introduction of these models could have a huge impact on different aspects of medical practice. Indeed, anatomical variability (both inter and intra-subject) has always been one of the most established challenges in medical data analysis. If the evolution of pathologies could be linked and correlated with the evolution of 3D PSMs, the diagnosis, follow-up, and analysis processes could rely on quantitative and well-documented facts. Also, it happens frequently that in the early stages of pathologies, morphological abnormalities are difficult to identify as *normality* is documented by a general 3D model of the organ or structure, such as an anatomical atlas, that hardly reflects the intrinsic variability of the human body. 3DPSM could work, instead, as personalized atlases of the patient able to provide specific and personalized information about the body state.

The application of such models is, nowadays, sought in almost any application of medical practice from teaching, computer-aided diagnosis to virtual surgery, and biomechanical simulations. Moreover, with the introduction and diffusion of Virtual or Augmented Reality systems, the use of 3D-PSMs will be further applied in the near future. The challenge is to integrate and possibly fuse adequately all sources of data and information and devise a presentation of 3DPSM suitable to support the various healthcare fields, from radiology to cardiology and neurology. 3DPSMs are therefore seen as a core ingredient to support new personalized care approaches, whose adoption is highly recommended and fostered by the scientific community.

1.2 Motivations

The development of medical image analysis and 3D shape modeling favored largely the progress in the field. Due to the complexity, importance, and delicacy of the healthcare environment, the development of patient-specific approaches is still challenging and nourishes very lively research areas. Almost all medical branches nowadays require the use of image and/or model visualization techniques and quantitative analysis tools that can support the diagnosis and monitoring of

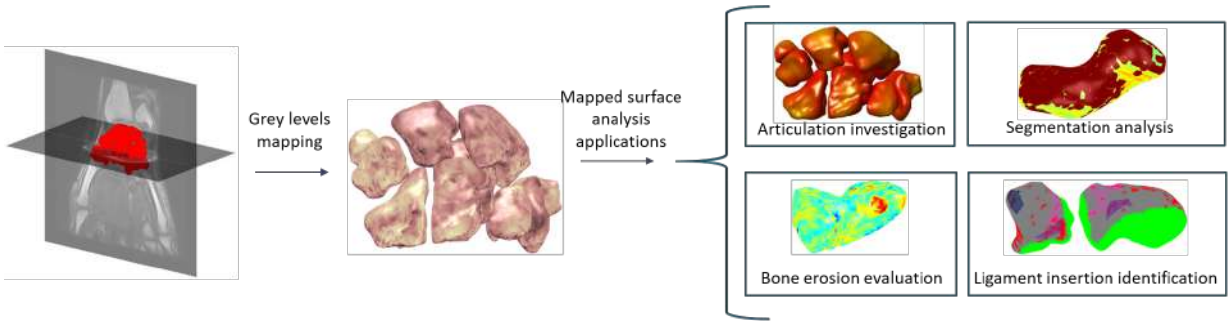

Figure 1.1: Summary of the proposed framework.

the patient's situation. One of the main challenges is the high variety of anatomical structures that compose the human body and the diversification of markers that characterize pathological conditions of the different anatomical districts.

Medical image analysis is a fundamental base for the definition of 3D PSMs, which, in turn, leads to personalized therapy and interventions [NK10]. As previously mentioned the techniques applied to generate 3D PSMs are various, meaning that different medical imaging techniques are at the root of 3D PSMs generation. Indeed, starting from an image scanning and proceeding with post-processing techniques it is possible to obtain a surface model with a plethora of segmentation methods [VP02].

With the growth of 3D visualization techniques, the necessity and the potentiality of assisted interpretation tools soon raised as well. The huge quantity of information that needs to be analyzed within a 3D volume image or surface model is one of the main reasons that supported this research branch. Moreover, the limited time that can be dedicated to the analysis of images and models, especially in the medical field, makes the presence of efficient visualization and interpretation instruments even more needed. Since the interpretation of such exams can influence the health of the subject or the patient, even the variation of the observer can impact the result, indeed a perceptual error, lack of training and fatigue are aspects that must not be underestimated.

1.3 Research goals, contributions, and novelties

Image features and descriptors are derived from signs inside an image and are typically represented as alphanumeric data. The two main classes of visual features contained in an image are *photometric (or texture-based) features* and *geometric features*. The first class is based on color and texture cues and typically do not need many operations to be extracted, since they are present on the raw pixels/voxels intensities. The second class, instead, exploits shape-based signs that

cannot be directly linked to pixels/voxels intensities but need to be deducted with proper processing.

In the medical field, texture-based features are particularly relevant since they can mirror the fine details contained in the image. Moreover, some of those features are below the threshold of applicability of the human eye but do not go unnoticed by computers. Indeed, usually, radiology images are described by grey-levels pixel intensities. The human eye is able to categorize an extremely low range of shades. For this reason, the computer-aided extraction of texture features is fundamental. On the one hand, the image raw data are not able to provide direct information on the shape of the imaged object since the 3D nature of the structure is still represented only implicitly. On the other hand, texture information is extremely useful to provide information on the tissue composition or the functionality of the anatomical structure being imaged.

Shape-based features aim to highlight edges, contours, joints, and other cues from the image. In this case, typically, the first step consists of the extraction of a proper shape representation from the pixels/voxels intensities to represent the 3D nature of the object explicitly. This is done with three well-known operations: region-of-interest detection, segmentation, and grouping. Geometrical features are fundamental and typically reliable in the detection of lesions. Nevertheless, the requirement of a segmentation process is the major obstacle to their use in clinical practice, since anatomical structure are embedded in complex and variable backgrounds that make the automatic segmentation quite challenging. Moreover, the segmentation process isolates the anatomical structures from the volumetric context in which they are immersed. This means that by changing perspective from volumes to surfaces, the volumetric information is lost.

We are, then, in front of two rather separate worlds that are equally relevant for the improvement of the clinical practice: on the one side, the possibility to retrieve information from the raw pixels values, on the other hand, the possibility to study a shape extracted from the image, that is, from its context. Huge developments have been made on both aspects but what is missing is an approach that, in a unique method, combines volume-based and surface-based information, to render the complete patient's situation. Indeed, most of the researches has addressed the improvement of Computer Graphics or image processing techniques separately.

1.3.1 Research questions and goals

In the context of 3D medical data and visualization methods applied to the clinical practice, the research proposed in this Thesis will focus on the gap between the world of shape analysis and texture processing. Different branches of the medical field could take advantage of integration among those heterogeneous kinds of data. From Computer-Aided Diagnosis to surgical planning and follow-up of patients, the visual information of the subject's health status is fundamental. In particular, rheumatology, dealing often with chronic or degenerative diseases, is one of the medical fields that could benefit from an integration of surface and volume information. Searching for

the possibility to integrate the information belonging to each separate approach, the main question that represented the starting point of this work was: **is it possible to devise an approach to represent segmented surfaces augmented with information about their volumetric context?** To address this question (Chapter 4), a hybrid representation, based on a data structure that functions as a bridge between surface and volume, can be obtained mapping the volume's grey-levels onto the 3D model.

Nevertheless, the possibility to quantify information, rather than just visualizing them is as well extremely crucial in the medical field. The more information can be retrieved in an accurate modality, the better the situation will be studied. For this reason, the other open problem analyzed (Chapter 5) in this Thesis started from the following question: **Is it possible to apply together methods of shape analysis and texture analysis on the integrated approach result, in order to make medical tools more reliable and accurate?**

Further analysis of the real case applications of the proposed approach highlighted the problem of identifying key information needed by physicians to improve the diagnosis and follow-up process. Indeed, the research focused on how additional information on ligaments, articulation regions, tissue erosion, and segmentation phase could be extracted through an integrated approach (Chapters 5, 6). Indeed, the last question that this research addresses is: **which kind of information is it possible to retrieve from the integrated model in real practice?**

The answers to these three research questions are the main contribution of this Thesis, which aims to facilitate the work of physicians and surgeons especially in the field of rheumatic diseases.

Research goals The main research goal of this Ph.D. Thesis is the study and development of innovative methods for the integration of surface-based with volume-based information of segmented anatomical districts, for the identification of landmarks and/or ligament insertion sites, and the improvement of segmentation techniques, with applications to computer-assisted diagnosis and biomedicine (Fig. 1.1). Indeed, the integration of heterogeneous clinical data, in particular of volume images information, with morphological information retrieved from shape analysis, has been the first focus of the project. The integration has been performed through a mapping of the grey-levels of the volume image onto the 3D surface model extracted from the image itself. With this integration, a novel enhanced visualization method of 3D patient-specific anatomical models have been developed. A method that can be applied to different human body anatomical structures and without restriction on how the 3D surface models are obtained from the images. The integration of these methods is supported by a simple but effective graphical user interface. In a field that is constantly changing and where reliability and accuracy are more than ever necessary, the simplicity of the applicability to real cases is often the aspect that will favor an innovation.

1.3.2 Research contributions and novelties

The combination of shape analysis techniques with the information provided by the texture of the model permitted to extend the application of the visualization tool in different areas, each of which represents a different contribution. Indeed the overall contributions of this work are:

- the development of a novel algorithm for integrating surface-based (i.e., segmented 3D meshes of anatomical structures) and volume-based (i.e., original MRI volume) information, based on different criteria for mapping grey-level values onto the segmented surface;
- the development of methodological approaches and algorithms for the use of grey-levels mapping in morphological analysis of the segmented anatomical structures, and the implementation of software and graphical user interfaces to perform analysis and evaluation of the results. Addressed applications are:
  - the *identification of (patient-specific) ligament insertion sites and articulation areas on bones from segmented MR images*, that allows the characterization of the local morphology of bones/tissues, and the early diagnosis and classification of muscle-skeletal pathologies. The identification and characterization of anatomical areas through the help of the integrated method represents an application where the limits of shape analysis alone can be overcome with the use of image information. Landmark identification represents a huge challenge in the analysis of the anatomical structures. Indeed, the intra- and inter-subject high variability have always represented a big obstacle in pursuing this scope. Often anatomical landmarks, such as articulation regions, are not placed in areas with particular morphological characteristics. Thus, an analysis based solely on shape features will fail in the identification. With the additional information given by the gray levels of the texture, it is possible to retrieve some clues on where the landmark can be placed for the specific patient.
  - the *analysis of multiple segmentations of a given anatomical district* in order to reduce operator dependency and to overcome the absence of a real gold standard for the evaluation of automatic segmentations. The segmentation analysis, carried over by the information added to the surface by the texture, permits to evaluate where the boundaries of the structure have been placed. Since segmentation has always represented one of the most challenging areas of medical image processing, the possibility to understand the structures placed around the segmented object provide helpful information for further anatomical analysis.
  - the *evaluation and comparison of (unsupervised) segmentation methods*, in collaboration with Prof. Silvana DellePiane and Marco Trombini (Ph.D. student) at UNIGE-DITEN.
  - the application of the integration result for *follow-up analysis* and monitoring of the patient. The possibility to provide support on the analysis of follow-up situations

in patients is one of the main problems of the clinical practice, especially for degenerative or recurrent diseases. The contribution of the developed techniques also includes the correction of possible errors through the use of integrated information and augmented visualization.

Research novelties As the main novelties and contributions of the Thesis with respect to previous work in the biomedical domain, the proposed approach:

1. effectively integrates information derived from medical images and 3D shape analysis;
2. applies to different anatomical districts independently of the acquisition methodology (e.g., MR, CT) and of the 3D segmentation methods;
3. has potential applications in the diagnosis process and easy integration with already established clinical workflows.

1.4 Thesis structure

The Thesis is divided into two parts. The first part describes the motivation, background, state of the art, and the main approach developed (Chapters 1, 2, 3, 4). The second part focuses on the clinical application of the integration approach results (Chapters 5, 6, 7).

Chapter 2 contains an overview of the state-of-the-art techniques involved in the different aspects addressed in the research. The topics that intersect and provide the basis for this work are: segmentation, semantic annotation, shape characterization, and anatomical landmark identification.

Chapter 3 provides an overview of the specific case-studies addressed in the Thesis. In particular, the focus is on the description of the selected data sets of MR images, with an analysis of the various components and related information. Moreover, the Chapter provides both the anatomical and pathological background relevant to the overall understanding of the work.

Chapter 4 presents the novel method developed for the integration of surface-based and volume-based medical data, along with the various data structures involved and developed. Furthermore, the Chapter provides an analysis of the results, with the description of the integration's clinical relevance.

Chapter 5 focuses on the clinical application of the integration method. In particular on both early diagnosis and monitoring support. Ligaments insertion sites and articulation regions are characterized using a combination of texture and shape analysis methods in order to augment

the information provided to rheumatologists. Moreover, follow-ups analysis is taken into consideration given the degenerative nature of most rheumatic diseases and, thus, the importance associated with the monitoring phase.

Chapter 6 discusses the analysis of the segmentation from both an anatomical and an evaluation point of view, considering state-of-the-art evaluation methods and the challenging aspects of medical segmentation. In this context, the Chapter presents a solution for the visual description of the tissues distribution around the segmented object, which indirectly provides information on the segmentation decisions. Moreover, in the Chapter are described the main results of the development of an unsupervised segmentation evaluation method, in collaboration with Professor Dellepiane and Marco Trombini, University of Genova.

Finally, **Chapter 7** summarizes the results of the work in terms of novelties and contributions, providing also the possible future directions of this research.

1.5 Future directions

Regarding the study on the segmentation results and evaluation, starting from the work developed with the University of Genova, the idea is to define a novel segmentation method for low-field MR images and for the local correction/improvement of a given segmentation.

Moreover, even if in this Thesis has been performed a statistical analysis of the results, a wider clinical validation could further support our conclusions. This research could benefit from clinical evaluation of the results, not only for the carpal district but also for other musculoskeletal structures.

Moreover, future work will focus on the improvement of the follow-up exams integration approach. The idea is to move toward a fully automatic parameter setting, integrated with a quantitative measure of the erosion. A higher number of monitoring exams, increasing the data set related to the single patient, could help the automatic adjustment of the parameter.

Finally, since the method can be applied to different imaging techniques, and given the progress of medical imaging toward image fusion techniques, a valid perspective could be to proceed in this direction. A 2-years research fellowship at CNR-IMATI and in collaboration with Esaote SPA on a research project focused on image fusion will be a good opportunity to expand the work described in this Thesis. The title of the research is, ”Image-fusion study and development of innovative approaches to fusion, analysis, and visualization of MRI low field images and ultrasound for the improvement of musculoskeletal pathologies diagnosis” and it will permit to extend the application of the method developed to other imaging techniques and scenarios.

1.6 Publications

The contribution described in the previous paragraph have been published in:

International Journal paper:

- **M. Paccini**, G. Patané, M. Spagnuolo *Analysis of 3D Segmented Anatomical Districts through Grey-Levels Mapping*. Published in Elsevier **Computers** & **Graphics** volume 91 pp 179-188 Special Section on 3DOR 2020. This paper regards the description of the mapping method developed and the different real clinical applications considered. In particular, the article concerns articulation regions analysis, ligament insertion identification, and follow-up analysis. **Chapters 4 and 5** addresses the content of this paper.

  SCOPUS & **WoS Journal** indexing. DOI: https://doi.org/10.1016/j.cag.2020.07.015

Conference proceedings:

- Imon Banerjee, **Martina Paccini**, Enrico Ferrari, Chiara Eva Catalano, Silvia Biasotti, and Michela Spagnuolo *Feature-based Characterization of Patient-specific 3D Anatomical Models*. Published in Italian Chapter Conference 2019 - **Smart Tools and Applications in Graphics, STAG 2019**. This article concerns the integration of machine learning methods with geometrical analysis for characterizing anatomical landmarks on patient-specific 3D carpal bone models. Geometrical features, extracted from the 3D model, constitute the input to a machine-learning algorithm. The goal is to identify anatomical landmarks on new patient's bones, finding which set of features performs better in the anatomical characterization.

  SCOPUS indexing. DOI: https://doi.org/10.2312/stag.20191362

- **M. Paccini**, G. Patanè, M. Spagnuolo *Mapping grey-levels on 3D Segmented Anatomical Districts*. Poster presented at Italian Chapter Conference 2019 - **Smart Tools and Applications in Graphics, STAG 2019**. Which describes the mapping method and the early results obtained. The content of this publication is described in **Chapter 4**

  SCOPUS indexing. DOI: https://doi.org/10.2312/stag.20191371

- **M. Paccini**, G. Patanè, M. Spagnuolo *Comparison and Integration of Erosion Evaluation Methods in Rheumatic Degenerative Diseases*. Conference poster presented at Italian Chapter Conference 2020 - **Smart Tools and Applications in Graphics, STAG 2020**. This poster focuses on the analysis of follow-up with a comparison between different approaches: geometry-based approach, texture-based approach, and integration of geometric and texture information. **Chapter 5** addresses the topic presented in this poster.

  SCOPUS indexing. DOI: https://doi.org/10.2312/stag.20201249

Chapter 2

Volume Images and Surface Models Analysis in Radiology

2.1 Introduction

In medicine, imaging techniques are currently one of the most used and important tools for diagnosis and monitoring, especially in the radiological field, where images represent the core instrument and starting point of different medical evaluations. Compared to the consumer domain, medical images present several challenges: they contain various and subtle features that result relevant for medical diagnosis and, thus, need to be correctly assessed and deepened. Moreover, given the delicacy of the purposes for which medical images are provided, the interpretation accuracy must be maintained at high levels while maximizing efficiency. Indeed, with the increasing of exams number and of the information provided by each exam, the time-consuming operations that must be carried on to properly analyze all the acquired data must be supported by automatic or semi-automatic instruments.

In this context, the term Computer-Aided Diagnosis (CAD) systems include a class of methodologies that have been studied and improved for years now. Such systems are designed to show the perceptual component of the data in order to favor the interpretation of the underlying information. Another class of methodologies that have been established in the past years to support the radiology interpretation is Content-Based Image Retrieval (CBIR), which aims to find similarities in image content. The role of such a branch of research is particularly interesting in terms of efficiency in image analysis and support to CAD systems. At the root of CAD and CBIR systems, there is the necessity to analyze the information contained in the image data and to extract image features or descriptors, which represent texture, spatial and geometric characteristics of the input image.

Medical image analysis can be thought of as a means toward a variety of goals. The investigation of image content, indeed, has been studied for many years and today a huge amount of clinical tasks is performed automatically or semi-automatically, from image segmentation (Section 2.2) and shape characterization (Section 2.3) to landmark identification (Section 2.4). Moreover, with the development of Computer Graphics techniques (e.g., iso-surface extraction, segmentation) it is possible to extract 3D shape models, which support an improved visualization and analysis of the case study. For this reason, 3D models are used as support of image analysis along with image processing algorithms. The segmentation can be performed using both algorithms that work on images, as well as shape models. In the same way, shape characterization and landmark identification take advantage of image processing and shape models.

Processing medical images, however, represents a challenge for three main reasons. Firstly, the image obtained can be of poor quality, as some image scanning techniques use harmful radiation to produce the desired signal; indeed, it is necessary a trade-off between acquisition speed and quantity of radiation transmitted to the patient. Moreover, patient physiological movements, such as respiratory or cardiac motion, or involuntary changes in position can introduce artifacts in the resulting image. Secondly, for all the principal imaging techniques there is a huge quantity of settings that lead to a large variety of image appearance and intensity distributions. For this reason, the automatic or semi-automatic solution to clinical problems should be as general as possible, in order to apply to different scanning modalities. Last but not least, human anatomy is highly complex: it presents various tissues and organs different in shape, size, and composition that appear in different manners on the image. Moreover, the anatomy of each individual presents its peculiarity and is subjected to changes over time. The variability of human anatomy, indeed, is not just an inter-subject but also an itra-subject issue. For those three main reasons, the automation of clinical tasks through image analysis is still an open and productive branch of research.

It is well known, that Artificial Intelligence approaches, such as machine learning and deep learning are widely applied to various medical branches. In particular, it is evident how these techniques have spread in every aspect of medical image analysis. The application of learning methods, especially deep learning, to the medical field has seen a rapid growth between 2015 and 2016. However, despite their quite recent use in the clinical environment, such approaches have shown remarkable performance improvements and outstanding results. Nevertheless, it is also clear that learning algorithms present several challenges and drawbacks, especially in the medical image analysis field. The first problem is the lack of large data sets associated with a relevant annotation. In fact, other than the difficulty to obtain the annotation of a wide data set from experts, often, such annotation can be noisy, limiting the algorithm development. Another typical challenge is called *class imbalance* and is linked to the fact that the anatomy of interest, or the lesion to be identified, occupies only a small portion of the image. This leads to biases in the trained networks toward the backgrounds since most of the image patches belong to it, while small organs and abnormalities should have greater importance [HJHK19]. When dealing with small data sets, overfitting represents a possible problem. This means that the trained model is

able to capture patterns in the training set but tends to fail with unprocessed instances [HJHK19]. Besides, once more, the medical field represents a peculiar environment since useful information for the final goal, often, are contained not only in the images but also in other data: patient history, age, demographics, and so on. Thus, a proper balance between image and clinical features relevance must be found [LKB+17]. For these, and other challenges, different solutions have been proposed and are currently being studied [LKB+17], [HJHK19]. Such solutions, however, are focused on the image analysis scope and do not consider the integration of image information with 3D shape model analysis.

This Chapter aims to provide an overview of the principal goals of image analysis and 3D models in the radiology environment with a focus on the main applications that will be later treated in this thesis. Finally, we discuss how the clinical practice paradigm is changing toward a personalized approach. A specific literature review for each application in relation to the case-studies can be found in the introduction of the relative Chapters of the thesis.

2.2 Image segmentation overview

In general terms, the segmentation consists in the process of image partition in distinct and homogeneous regions, in order to obtain an efficient representation of the region of interest. Since it does not exist a generic and automatic image segmentation, the type of image and its content highly affect the performances of current segmentation algorithms. This problem is even more felt in medical images, due to the high variability of anatomical districts in terms of tissues, features, pathologies, patients' characteristics.

The main methods for the segmentation of medical images can be subdivided in the following classes [FM16]:

- threshold bases methods;
- region based methods;
- clustering and classification methods;
- deformable models methods.

Threshold based methods These approaches assume that different objects in the image have different intensity values. Thus, the intensities of objects are compared with respect to one or more thresholds. In the single threshold case, we talk about *global thresholding*. It is the case of images that present a bimodal histogram, where a single threshold is enough to separate the background from the foreground. When leveraging more than one thresholds, we refer to *local*

thresholding. Usually, more than one threshold is required in presence of abnormalities or when the goal is to separate different types of objects at the same time [FM16]. This approach does not provide any spatial or location information since the thresholds are usually extracted from an analysis of the image histogram. This is the main reason why thresholding methods are quite sensitive to noise and inhomogeneities; indeed, there is the possibility that the pixels identified through thresholding are not contiguous.

In *global thresholding*, all the pixels above the threshold are set equal to one, while those ones below the threshold are set equal to zero. Considering $f(x, y)$ the intensity of the pixel positioned in (x, y), T the threshold value, the *global thresholding* can be described as [GWE04]:

$$g\left(x,y\right)=\begin{cases}1 & f\left(x,y\right)\geq T\\ 0 & \text{otherwise}\end{cases}, \tag{2.1}$$

where $g(x, y)$ is the resulting binary value of the pixel.

The core difference between the various algorithms resides in the method used to identify the proper value of the threshold automatically. The Otsu thresholding methods [Ots79] is one of the most established and used algorithms: it assumes that the image histogram is bimodal and recursively finds the optimal threshold value as the one that minimizes the overlap between object and background.

In *local thresholding*, instead, the value of the threshold changes through the space of the image, according to the following condition

$$g\left(x,y\right)=\begin{cases}1 & f\left(x,y\right)\geq T\left(x,y\right)\\ 0 & f\left(x,y\right)<T\left(x,y\right)\end{cases}. \tag{2.2}$$

The local threshold is computed considering both local and global information such as statistical properties as in [SK07], or even dividing the image into sub-images [Cha16]. *Local thresholding* techniques can also compensate for changes in the image illumination that represent one of the obstacles for the application of *global thresholding* approaches [Cha16].

Even if these methods are particularly indicated for images that are characterized by homogeneous regions and where the separation between background and foreground is well defined, they have problems with low contrasted images or in presence of noise. In this case, the integration of the threshold approach with other techniques able to refine the result could be a solution as proposed in [ZYCO10] and [BHR$^+$15].

Region-based methods Region-based methods divide the image into different regions, which are obtained by merging neighboring pixels according to predefined similarity criteria such that:

- every region is spatially connected;

- the union of the regions composes the whole image (exhaustive property);
- the regions are not overlapping;
- every region satisfy a homogeneity criterion;
- two and not neighboring regions do not satisfy the homogeneity criterion.

The *region growing* [AB94] algorithm is one of the most famous techniques in the field of segmentation methods. It is an iterative method that requires at least one seed located in the region of interest of the image. Given the seed, the method proceeds to compare it to neighboring pixels, adding them to the region if they satisfy the similarity criterion. The process stops when no other pixel of the image can be added to the region. This method is simple and intuitive but the result highly depends on the seed initialization that can be automatized through the use of a Clustering algorithm. This technique is also quite error-prone if the image present low contrast and high noise. In this case, new features for similarity criterion improvement can be introduced [SCW12].

Clustering and classification methods Classification methods typically take advantage of training data and can be either supervised or unsupervised. The training data is exploited to find characteristic patterns in the image, then the classifier able to recognize those patterns is used to cluster the image pixels in the feature space. A clusterization consists in the division of the data to have high intra-class similarity and low inter-class similarity. Usually, what determines the value of similarity is an appropriate distance measure [FM16].

The *Fuzzy C-means (FCM)* clustering methods are typically unsupervised and able to divide the input data into two or more clusters, meaning that FCM algorithms can perform the segmentation of more than one object at the same time. Relying the decision on the distance between the analyzed data point and the cluster, the algorithm assigns each data point to a cluster center. Thus, the nearer is the data point to a cluster center the higher is the possibility for that data point to acquire the membership to that cluster center. Since this algorithm applies recursive processing of the input data, its cost is rather high. For this reason, different, faster, and more robust variations of these techniques have been studied; for a comparison of improved FCMs, we refer the reader to [CK16].

Markov Random Field (MRF) is another approach to image segmentation that performs data clustering. It introduces spatial information into the clustering procedure reducing the problem of image noise influence as well as the problem of overlapping clusters. The application of MRF to images was proposed in [GG84] through the use of tags associated with the nodes of a graph-based representation of the image. Those tags are applied through an optimization process that corresponds to a maximum posterior probability. The segmentation of such graph representation, then, consists of an appropriate cutting of the graph.

Artificial Neural Networks (ANN) are at the core of most of the machine learning and deep learning approaches that, nowadays, are applied to an extremely high variety of tasks. Among those different problems, solved with the use of artificial intelligence (AI) techniques, the segmentation of medical images is one of the most studied [MSZ11]. The architecture of those algorithms is usually based on a network, whose input nodes receive the features that will be processed, through mathematical operation, in the following layers of the net (hidden layers). Finally, the result is extracted at the output nodes. The complexity of the network depends on the number, the connections, and the sequence of hidden layers. Indeed, hidden layers, allow the modeling of non-linear dependencies in the input data. These techniques, other than providing an end-to-end approach to the segmentation process, are also non-parametric approaches since no parametric distribution of the data is assumed. Through the use of ANNs, it is possible to create a high variety of AI algorithms from the simplest machine learning approach to the most articulated deep learning method. A description of the most important and recent deep learning based algorithms for image segmentation can be found in [MBP+20]. A focus on the medical images highlights how Convolutional Neural Networks (CNNs), U-nets, fully Convolutional Neural Networks (fCNNs), and Recurrent Neural Networks (RNNs) are the most diffused and studied networks for segmentation purposes. A description of their architecture, working principles, and applications is presented in [LKB+17] and [HJHK19].

Deformable models methods Deformable models are used to segment anatomical structures in medical images exploiting a connected and continuous mode, which takes into account an a-priori knowledge about location, size, orientation, and shape of these structures [FM16]. The deformability of such models permits their adaptation to the significant variability of biological structures. The general idea is to evolve a curve, subject to constraints based on the characteristics of the object to be segmented, deforming it from an initial configuration until it fits the edges of the object. The two main classes of deformable models are *parametric models*, which describe the contour through the use of parametric curves, and *geometric models*, which describe the contour movement implicitly as the evolution of the levels of a function. Indeed, in the geometric case, the contour evolves to fit and track objects of interest by modifying the underlying embedding function instead of modifying the parametric curve function. Since these methods are quite sensitive to the initialization phase, especially in problems where the boundaries of different objects are closed to each other, the seeds represent the initial points from which the contours evolve and have to be accurately placed.

In literature, there are different approaches for the definition, evolution, and control of the curves. The first approaches were based on *Snakes*, later *Active Contour* [KWT88] and *Active Region* have been proposed. With the development of research in the field, *Geodesic Active Contour* have been developed [CKS97]. Finally, the use of *active shape models* has been introduced, starting the application of models based on a-priori knowledge of the anatomy [Lev00]. Knowledge-based techniques allow the user to overcome problems related to low contrast or high noise level, which are the main source of errors in segmentation algorithms. For this reason, the use of

Statistical Shape Models and *Active Shape Models* for the segmentation of volume images have become well-established segmentation techniques [HM09].

2.3 Shape characterization for Semantic Annotation

Generally, we can talk about two main standard classes of visualization methods for a medical volume data set: *surface rendering* and *volume rendering*. *Volume rendering* is typically used for the 3D visualization of the volume through its original grey-levels, thus providing information on density or tissue composition. *Surface rendering* techniques provide a 3D visualization of object's surfaces starting from a segmented image and highlighting the morphology of the segmented regions.

The value brought by the 3D reconstruction is not limited to the sole visualization but extends to the extraction of other valuable characteristics of the segmented image (Section 2.3.1). Thanks to technology development, it is also possible to formalize the knowledge on the field in order to support the analysis and the automatic reasoning on this wide range of data. Indeed, computer-aided medicine exploits such a structured organization of the digital data, through the application of knowledge and visualization technologies. To perform comprehensive reasoning, the knowledge of anatomical structure is not enough, as the formalization should take into account temporal changes in anatomical structure, functional behavior, and pathologies of organs and systems. In particular, the comparison of clinical images from different patients with similar anatomical or pathological characteristics can help not only the diagnosis phase but also treatment planning and monitoring (Section 2.3.2). To perform such a comparison, it is necessary to annotate images exploiting clinical ontologies. In recent years, the use of ontologies in the medical practice has evolved, thanks to a huge work of research on how to efficiently utilize them in patient-specific data management, clinical decision-support systems, and patient healthcare planning.

In this context, ontologies are used for the management of structural and functional information obtained by medical data. Some ontologies have been developed with a computational framework for clinical diagnosis support [PA06] or for human anatomy and organ functional behavior study [PBJ+09] and with properly developed scale levels for the support of specific pathologies, such as musculoskeletal ones. Moreover, a survey on recent approaches to the access and presentation of medical data has been presented in order to describe how knowledge-driven data organization may support real clinical task management [BCRS14].

In the clinical field, the annotation process consists of associating information related to the application domain to a volume image or a 3D surface model of an anatomical structure, providing a link between conceptual and geometric levels. In this case, the conceptual level is represented by the medical knowledge, while the geometric level can consist of pixels, voxels, and triangles that belong to a region of interest for the physician. The semantic annotation is a process that does not belong exclusively to the medical field, indeed it has been studied in different research

areas along with the multi-scale representation. However, once more, the clinical environment presents particular challenges since usually the data to be considered are heterogeneous, volumetric, and highly variable. Image or shape characterization is a fundamental requirement for a correct annotation process.

2.3.1 Shape-based characterization: a review in anatomy

Shape characterization has been a widely studied topic in the field of 3D shape modeling, where surfaces are typically represented as triangular meshes or point-clouds. The majority of the approaches to *shape segmentation* can be seen as optimization methods of the segmentation of a triangular mesh, where the criteria used for the optimization concerns some geometric property [Sha08]. Region growing, clustering, spectral analysis techniques, are the main methods to approach the optimization problem. Those methods typically involve a homogeneity criterion based on geometric properties that characterize the segmented element. In the work presented by [HS97], *implicit methods* identify the contours of the regions of interest and work on the properties that characterize the shape changes. The basic hypothesis, here, is that the shape is perceived through the identification of its relevant parts, characterized by the lines on the shape on which a drastic change in the curvature occurs.

Thanks to the development of the 3D shape analysis framework, it is now possible to quantify the deformation of a structure shape into another in terms of the variation of real functions. This has changed the perspective of similarity assessment and opened new possibilities. Indeed, while the classical approaches to similarity mainly quantify it as a numerical score, map-based methods also define (dense) shape correspondences. The work by [BCBB16], presents the theoretical foundations underlying these approaches and a classification based on their most salient features, such as the kind of structure and invariance properties they capture, or the distances and the output modalities according to which the similarity between shapes is assessed and returned. The same paper also describes the usage of these methods in a number of 3D shape application domains, among which annotation and segmentation.

As an example, regarding the characterization of anatomical districts, a study for the annotation of functional parts, considers the extraction of different geometry features to guide the identification of the region of interest on the bone [BCPS16]. Moreover, the work introduces two novel features able to describe not only the single bone morphology but also the whole district characteristics.

2.3.2 Image-based characterization

If the annotation is performed exploiting volume images, then a fundamental step, similar to what happens for 3D shape models, is to retrieve information on the image in order to identify

the region of interest that has to be annotated. Even in this case, there are different ways to perform the task, as described in [ARN+11]. The paper points out that, if the center of the characterization is the image, then the features will focus on visual property, whether local or global. The similarity between sets of features helps to identify the clinically relevant parts of the image and to characterize them. Where, as similarity, is intended the distance between the sets of features: a shorter distance indicates higher similarity. The selected metric depends on the type of features or descriptors and on their representation. The descriptors used in this field can be *general*, as color, texture, pixel gradient, or histograms, which do not need any prior domain-specific knowledge in order to be computed.

As for the model-based anatomical characterization, in recent years, different researches have been conducted in image-based characterization. Since most of the features are related to texture and color, the characterization is focused mostly on the tissue that composes the district, rather than on the geometrical features presented by the morphology. Anyhow, the information retrieved from this kind of characterization is considered for the annotation process.

Examples of the type of information provided by an image-based characterization in the radiology environment can be found in works such as the one proposed by [LYV+12]. The paper presents a semi-automatic imaging technique that provides quantitative characterization of bone marrow edema pattern (BME) in wrist joints of patients with Rheumatoid Arthritis (RA), including volume, signal intensity changes, and perfusion properties. The characterization of bone density comparing two imaging techniques results, instead, have been studied by [WCK+14]. Those are just two focused examples of the high variety of anatomical characterizations that can be performed on medical images.

2.4 State of the art on anatomical landmark identification

In radiology, regions or points of an anatomical structure that present peculiar shape characteristics or functional importance are called landmarks. Their accurate localization on each patient or subject has huge importance in different medical areas. The search of those points of reference on each subject can be seen as a part of the anatomical characterization since it provides the placement of regions associated with specific clinical knowledge. Indeed, such points provide information on the functionality and morphology of the anatomical structure of interest. Landmarks are relevant, first of all, as a guidance and a reference for surgical planning and interventions. Moreover, diagnosis and monitoring of patient status benefit from the correct location of such reference points. In literature, it is well established that accurate localization of 3D landmarks is fundamental in different clinical aspects [SRA09]. The usefulness of such references goes from biomechanical studies and computer-integrated surgery (both for the planning and the navigation of execution phase) to the design and positioning of customized implants and prostheses (e.g. [GKT+14]). They are also extremely helpful for joint kinematics study

(e.g., [MMPL07], [ML17]), deformities assessment (e.g., [HBGD18]), and registration in shape models [HM09].

Landmark identification is another task that can benefit from both image content extraction (Section 2.4.2) and 3D model morphology evaluation (Section 2.4.1). Thus, both images and 3D shape models can be considered useful instruments to support the landmark identification task. The main challenges related to landmarks identification are linked to the fact that these landmarks are influenced by bone morphology, and hence prior knowledge of anatomical landmarks helps in identify them precisely. Moreover, since landmarks are not clearly identifiable discrete points, but rather small or large areas, there is always a positional uncertainty to deal with [SRA09].

Since the manual localization of landmarks is error-prone and extremely time-consuming, the research related to automatic localization methods is highly active. Automated approaches (e.g. [PHAN06], [YZY+15]), mitigate the inter and intra-rater variability exploiting an objective and efficient process without manual interference. Therefore, many automated localization methods have been proposed, with varying degrees of robustness, reliability, and generalization potential. Although the automatic methods achieve high accuracy, they are either dependent heavily on initial manual localization or likely lack of geometric distinctiveness in the prediction.

2.4.1 3D Shape models for landmarks identification

Some of the clinically relevant anatomical points are placed in regions with a peculiar morphological characteristic. In this case, exploiting a 3D model that mimics the anatomy of the specific subject can be considered the best way to identify such landmarks accurately. Indeed the advances in medical imaging, image analysis, and computational capabilities permit to explore shape properties in order to support landmark localization.

Surface regions can be classified based on their shapes exploiting different geometric measures such as curvatures, extreme points, and higher-order derivatives. Surfaces can be classified into various regions such as ridges, umbilicus, and singular lines [SRA08]. Self-contained frameworks to generate landmarks on surfaces extracted from volumetric data can be found in the literature. As an example, the pipeline presented in [ZBLR17], is composed of three phases: surface construction, crest line extraction, and landmark identification. Examples of studies applied to human anatomy, and regarding the identification of reference points on 3D models have been proposed in [EHPP04]. In this work, the authors use predefined templates to locate landmarks on 3D hip models for surgery planning. In this case, however, it is necessary to accurately morph and register the atlas model with the patient model. A method for extracting anatomical landmarks on the cylindraceous body surface, in particular for extraction of curvatures, has been presented in [LKD04]. The paper provides an evaluation of prominent features on the foot and lower leg surface, which could be used in motion analysis or in medical treatment. In this work, the surface is scanned by FastSCAN (Polhemus, Colchester, Vermont, USA) and is described

by scattered three-dimensional surface points. The method consists of several steps producing a parameterized representation of the foot surface with regularly distributed data points, each providing coordinates, derivatives, and curvatures, thus allowing the maps of mean and Gaussian curvature to be plotted. To separate convexity from concavity, the Koenderink shape index is applied, and by checking curvature maps, the landmarks are characterized and discriminated.

In literature different methods to identify anatomical landmarks on images through the use of 3D models are present, an overview can be found in [SKH+09]. The paper analyzes three different approaches, with different degrees of generality in terms of applicability to other anatomical landmarks and of required amount of training data. The first method is problem-specific and based on the convex hull of the pelvis. The second method is a more generic approach based on a statistical shape model, including the landmarks of interest, for every training shape. The third method presents the most generic approach, where only a small set of training landmarks was required.

A systematic approach to identify anatomical landmarks on a knee joint has been studied by [SRA09]. It is based on their general geometric characteristics (curvature analysis) and the adjacency relationship between the landmarks (rules). Another study focuses on the extraction of anatomical features curve (AFC) from 3D hip bone models through the use of Computer Graphics methods [LQZ15]. In particular, they use direct curvature scale space-based technique to extract anatomical feature points (AFP) in every contour, using anatomical structure information as prior knowledge so that only AFPs are extracted. Then, corresponding AFPs are linked in different contours and AFC is generated. Moreover, anatomical landmarks have been used to guide prosthesis placement [dARF+17], with an automated workflow for femoral orientation and landmark extraction from a 3D surface mesh. The method concentrates on parameters that allow the surgeon to establish the correct position of bony cuts to restore leg length, and femoral offsets such as the femoral neck axis, the femoral middle diaphysis axis, both trochanters, and the center of the femoral head. Moreover, the definition of the medullary canal endosteal wall is used to position the prosthesis' stem. The final goal is to implement prosthesis alignment and sizing methods to provide the surgeon with presurgical information about the performance of each of the patient-specific femur-implant couplings

2.4.2 Use of image analysis for landmarks identification

Other than on the 3D shape models, the anatomical landmarks can be identified also directly on images, especially in those cases where the relevant feature is not characterized by a peculiar morphology, but rather by a relevant functional property or specific tissue. Indeed, anatomical landmarks can be defined on different tissue interfaces in medical images according to various clinical routines or studies [XDH+15].

The search for automatic methods for anatomical landmark identification has been going on for

years. Some works rely on the use of traditional image processing techniques, such as in the neurological field (e.g. [PHAN06]). In [WR06], the localization of anatomical landmarks in 3D MR and 3D CT images is based on 3D parametric intensity models that are directly fitted to 3D images. To efficiently model tip-like, saddle-like, and sphere-like anatomical structures, the authors introduce analytic intensity models based on the Gaussian error function in conjunction with 3D rigid transformations as well as deformations. Moreover, a new method for the selection of an optimal 3D ROI size for the effective fitting of a deformable model exploits the detection of the image gradient in the neighborhood of the landmark position. The proposed algorithm automatically initializes the model parameter through the use of differential properties (e.g., gradient and curvature) as well as other properties of the landmark structure in the image. Moreover, there are examples of approaches for cardio-vascular applications, such as the work presented by [EWvK+16].

Many other automatic approaches, instead, rely on the use of expanding machine learning and deep learning techniques. Indeed, In recent years, ground-breaking advancements with neural networks have been achieved in various domains, allowing for automatic learning of discriminative features for the problem. A survey of discriminative learning methods for appearance modeling, as well as their corresponding search strategies, has been presented by [Zho14], which discusses how they leverage the anatomical context embedded in the medical image for more effective and more efficient detections. Convolutional neural network (CNN) and graph cut optimization have been used in a novel framework to automatically locate femur landmarks from the 3D MR images [YZY+15]. Here, during the process of localization, both the global shape and local surface curvatures are taken into consideration, because they define the geometric features of landmarks. Another work objective, instead, has been to develop a new scheme of landmark detection, capable of dealing with MR images with various contrasts, patient positioning, and health conditions of the knee joint [XDH+15]. As a learning-based technique, the proposed method uses a set of manually placed landmarks to describe their appearance characteristics and, then, applies a boosting system to combine detection results obtained using different sets of training landmarks.

To the class of learning approaches belongs a work that follows a different paradigm by simultaneously modeling both the object appearance and the parameter search strategy as a unified behavioral task for an artificial agent [GGM+16]. In particular, the method combines the advantages of behavior learning, achieved through reinforcement learning, with effective hierarchical feature extraction, achieved through deep learning. Given only a sequence of annotated images, the agent can automatically and strategically learn optimal paths that converge to the sought anatomical landmark location as opposed to exhaustively scanning the entire solution space. Moreover, an approach based on the combination of two recurrent neural networks in a coarse-to-fine approach has been developed [APAC17]. The first network determines a candidate neighborhood by analyzing the complete given image volume. The second network localizes the actual landmark precisely and accurately in the candidate neighborhood. As previously mentioned, the problem with learning approaches in medicine is the lack of accurate and reliable data-sets that

are the core of an unbiased and complete training phase. Overall, the most common techniques among learning approaches seem to rely on 2D imaging classification with CNNs. However, recently, different studies proposed modified learning processes for a direct localization with good results. An overview of the latest approaches can be found in [LKB+17].

Chapter 3

Research Context and Case-Studies

3.1 Data set overview

In this Chapter, we focus on computational methods to support the study, diagnosis, and monitoring of rheumatic diseases, based on the integration of image processing and Computer Graphics techniques. Even if the method developed (Chapter 4) is quite general in terms of the input anatomical district and imaging modalities, it is important to focus on the specific contest on which the work has been developed. Traditionally, it is possible to identify four main types of imaging modalities according to the technology used to obtain them (Fig. 3.1):

In particular, the data set on which the research has been conducted is composed of Magnetic Resonance Images (MRI) of patients monitored in the Academic Division of Rheumatology of the University of Genoa. Magnetic resonance (MR) scans do not constitute a risk for patients since they use non-ionizing radiation. MR imaging provides both functional and anatomical information. This technology permits to exhibit soft tissue in high resolution evaluating the relaxation times of water molecules exposed to a magnetic field and radio-frequency pulse [WAAV19]. Therefore, it acquires physical quantities characteristic of the tissue with a deep understanding of soft tissues. (see Section 3.2 for an overview of MRI principles). MRIs' acquisitions in the data set are performed with a 0.2T (low-field) extremely dedicated machine (Artoscan, Esaote) using 3D T1 weighted sequences with reconstruction on the axial and sagittal plane [TCB+15].

The MRIs of the 118 subjects are associated with their segmentation performed by medical doctors. 108 subjects suffer from degenerative rheumatoid illnesses at different stages, while 10 of them are healthy subjects. In particular, the examinations were performed between August 2014 and January 2015, each including the hand and the wrist districts (Section 3.3). Among the MR images examined, besides the healthy controls, the patients are affected by either Rheumatoid Arthritis (RA), Psoriatic Arthritis (PSA), Gout, Palindromic Rheumatism (PR), Systemic SClerosis (SSC) (Section 3.4). The patients affected by RA are divided into three groups according to

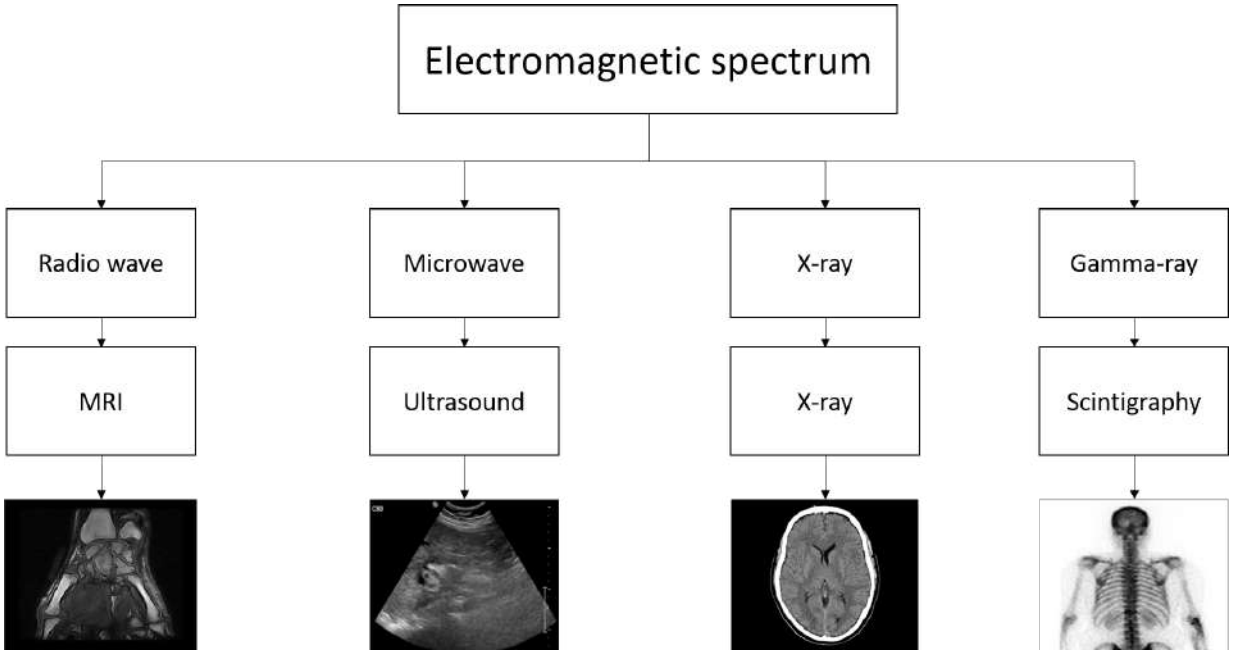

Figure 3.1: Core difference between the image technologies used in the medical practice along with examples of the resulting images.

disease duration, with 8 patients for each group. The first group has a disease duration of fewer than 6 months, the second group between 6 and 36 months, and the third group longer than 36 months. Furthermore, for 6 patients a follow-up examination is available [TCB+15].

The segmentations are carried out by experts, exploiting a CAD (Computer-Aided Diagnosis) system called RheumaSCORE [PCVV14], developed by Softeco Sismat S.r.l.. This system supports the rheumatologists during the segmentation operation, through a semi-automatic tool for bone detection, volume measurement, and 3D reconstruction of the segmented structures. Moreover, the system supports the visualization of the MR images and the selection of the anatomical structure to be segmented. These features of the CAD system help to select the seed point for the initialization of the segmentation, to correct the segmentation during the process, and to refine the results. Moreover, the bone surface is automatically reconstructed during the segmentation process using the Marching Cubes algorithm [LC87].

This data set was available through the Patient Browser: a web application that has been developed by Softeco Sismat S.r.l., to assist and support the user in the diagnosis and follow-up processes of rheumatic diseases. It is a web-based framework that permits to store, search, and visualize MR images and medical data, as well as to access different diagnostic measurements. The basic functionalities include the possibility to [TCB+15]:

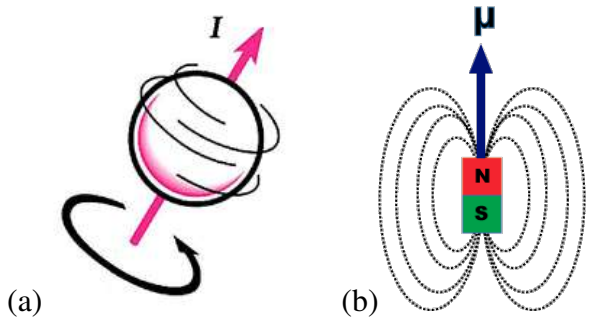

Figure 3.2: (a) Concept of spin as a spinning nucleus, where I is the value of the nuclear spin that can assume only discrete integer or half-integer values ranging from 0 to 8 [Spi]. (b) Magnetic field associated with the dipole, where the vector μ describes the tendency of the nucleus to interact with the external magnetic field [Maga].

- share the data analyzed through RheumaSCORE as 3D models, segmented data, and MRI exams;
- upload and store patient studies exported from RheumaSCORE;
- browse and visualize the results of different patient studies;
- display and compare diagnostic measurement;
- download the original images, segmentation results, and diagnostic measurements.

We will now focus on the description of the different information and content that can be retrieved and exploited from such a data set. Firstly, we will describe the particular imaging technology used to acquire the images that compose the data set. Then, we will focus on the description of the anatomical district that has been at the center of the study, namely the carpal district, followed by an analysis of the implication of rheumatic diseases on such district.

3.2 MRI basics and system

MRI is one of the most used and studied techniques in different branches of medical practice. Its success is due to the capability of acquiring both functional and anatomical images without harmful radiations. Indeed, the trade-off between the number of acquisitions and the possible injuries is no longer a problem in this case. With Computed Tomography (CT) or Positron Emission Tomography (PET), images show either between anatomical or functional information, unless image fusion technologies are involved. This means that the fields of application of MRI technology go from the ones where an accurate description of the anatomy of the subject is

needed, to others where the information required are related to organs or systems functionality or metabolism.

When dealing with medical images it is important to know the standard protocols for image communication (Section 3.2.2). Moreover, to better understand the characteristics of the low-field system (Section 3.2.1) and the informative content of MR images used in this work (Section 3.2.3), it is necessary to briefly describe what composes an MRI system and its functional principles. The core principle on which the MRI is founded is called *Nuclear Magnetic Resonance* and was discovered by Bloch and Purcell in 1946. From this discovery, the technique evolved until it was applied in the clinical environment in the '70s. The nuclear magnetic resonance is the phenomenon for which the nuclei of certain atoms demonstrate the ability to absorb and re-emit radiofrequency energy when placed in a magnetic field [TSS15]. This phenomenon is exploited by employing a strong magnetic field that forces protons in the body to align with that field. A radiofrequency pulsed current is used to stimulates the protons, which spin out of equilibrium, straining against the pull of the magnetic field. When the radiofrequency field is switched off, the MRI sensors detect the energy released as the protons realign with the magnetic field. The time it takes for the realignment, as well as the amount of energy released, changes depending on the environment and the nature of the tissue. Physicians are then able to distinguish between various types of tissues based on these magnetic properties [Magb].

Going deeper into the working principles of MRI, first of all, the nuclei suitable for MRI acquisitions present an odd number of protons or neutrons, meaning that they must have a nuclear charge. Usually, the nuclei of Hydrogens are considered, since they are composed of a single proton. Moreover, Hydrogens are largely present in all biological material and exhibit relatively high MR sensitivity. The fundamental property of such nuclei is called *spin* and depends on the number of protons. The spin can be thought of as the nucleus spinning around its axis. In reality, the nucleus does not spin in the classical meaning but its constituent parts induce a magnetic moment, thus generating a local magnetic field with north and south poles [GTC$^+$15] (Fig. 3.2). In normal conditions, such magnetic moments present random directions, canceling each other out, and thus the net magnetic vector is zero. With the application of an external magnetic field, usually called B_0, the nuclei present one of two possible orientations: parallel or antiparallel to the external field. Parallel alignment is the lower energy state and is thus the preferred alignment, whereas antiparallel alignment is the higher energy state. Thus, a net magnetization vector (M_z) aligned to the external magnet results from the difference between the two populations [VGWdB$^+$99] (Fig. 3.3 (a)). The nuclei will not be exactly aligned but will rotate, or precess, around the B_0 axis, with a fixed frequency of rotation called *Larmor frequency* (Fig. 3.3 (b)). The *Larmor equation* defines such frequency as proportional to the magnetic field strength:

$$\omega_0 = \gamma B_0, \tag{3.1}$$

where γ represents the gyromagnetic constant that is specific for the nucleus considered and gives an idea of the magnitude of the magnetic moment of the nucleus given its spin. Thus, Hydrogen nuclei will precess with the same frequency inside a unique magnetic field. The phase

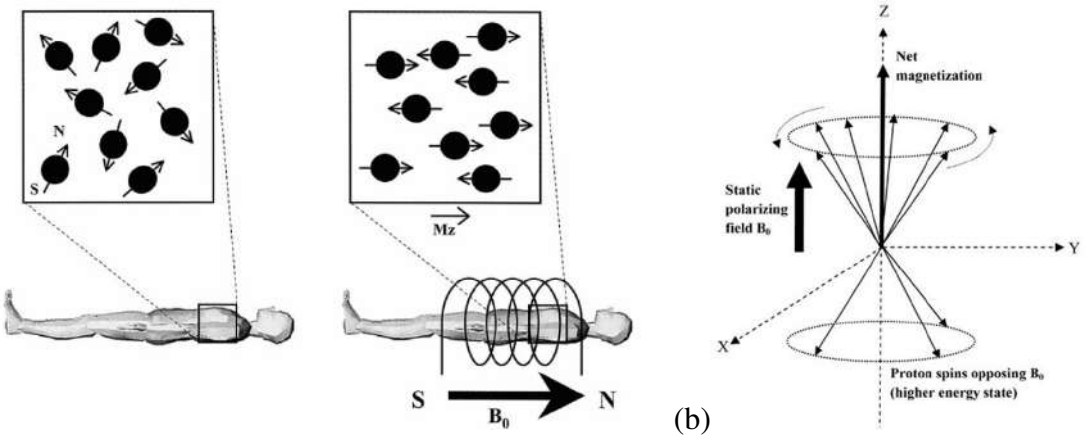

Figure 3.3: (a) [VGWdB$^+$99] Generation of a net magnetization vector M_z due to the application of an external field B_0 influencing the directions of the nuclei magnetic moments. (b) Precession of the nucleus spin axes around the direction of the external field [BGH$^+$11].

of the precession, instead, is different for each nucleus.

To obtain an informative signal from the spins, the direction of the magnetization vector must be changed, and the excitation operation is performed to this scope. Indeed, the application of a second radiofrequency (RF) magnetic field, called, B_1, perpendicular to B_0 excites the nuclei possessing spin. Usually, B_1 is applied in pulses that last microseconds [GTC$^+$15]. Such RF excitation energy is provided at the exact Larmor frequency (also called resonance frequency) and causes two different phenomena: first, enough protons absorb energy to jump from the parallel state to the higher level of the antiparallel state, and second, the spins are forced to precess in phase.

The overall effect is that the net magnetization (M_z) flips $90°$ from the positive z-axis to the transverse plane. Moreover, M_z in the transverse plane rotates around B_0 at the Larmor frequency. This rotating transverse magnetization can be measured because it will induce an alternating current (AC) in the receiver coil placed around the patient [VGWdB$^+$99].

After the excitation phase (RF signal is turned on), a return to equilibrium phase starts (RF signal is turned off). Indeed, when the RF transmitter is switched off, the spins will search the equilibrium state, meaning that the ones in a high energy state will go back to low energy. This causes the magnetization to decay over time, producing a decreasing magnitude of M_z in the transverse plane. Since M_z is responsible for the signal in the receiver coil, this signal will decrease according to the decay of M_z (Fig. 3.4). This phenomenon is called *Free induction decay* (FID) and the time that the signal employs to return to equilibrium is called *relaxation time*. In particular two independent types of relaxations take place. One type is called *longitudinal relaxation*, which regards the process of realignment to B_0 and is characterized by the T_1 relaxation time. T_1 represents the time required for the system to recover 63% of its equilibrium value after a $90°$ RF

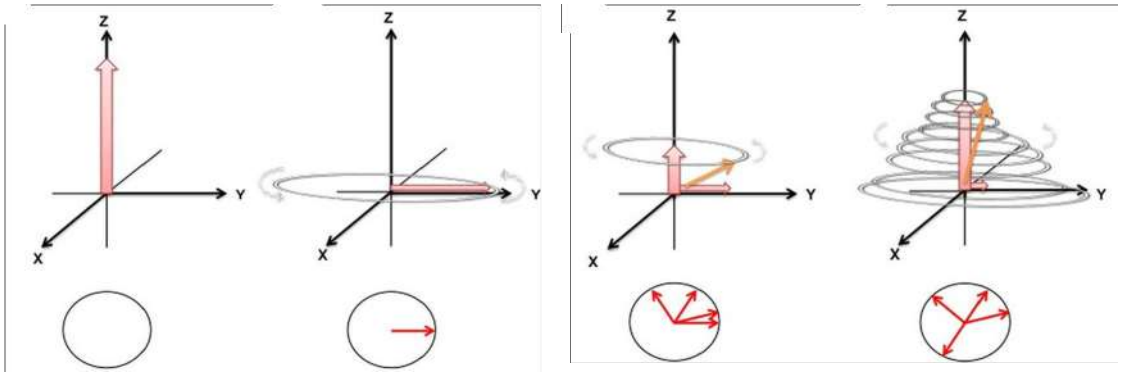

Figure 3.4: [CHC$^+$13] Applicatin of a $90°$ RF pulse producing the transverse magnetization, followed by the relaxation phase where nuclei fall out of phase and the transverse magnetization deminish returning to the equilibrium.

pulse, and has a specific value for each type of tissue (Fig. 3.5 (a)). The second type of relaxation is called *transverse relaxation* and regards the spins precessing around the magnetization vector. The exited spins precess completely in phase but, after the RF signal is switched off, begin to dephase due to small differences in the Larmor frequency, induced by random local magnetic inhomogeneities (due to spin-spin interaction), and inhomogeneity of the main static magnetic field B_0. As a result, the observed signal starts to decrease taking the name of transverse relaxation or *spin-spin* relaxation. T_2 is the relaxation time of this process and corresponds to the time it takes for dephasing to decay the signal to 37% of its original value. More precisely, the overall de-phasing is often called T_2* relaxation, which combines the effect of T_2 relaxation and additional de-phasing caused by local inhomogeneities in the applied magnetic field. T_2 relaxation is the result of spin-spin interactions and due to the random nature of molecular motion, this process is irreversible. T_2* relaxation considers a more rapid decay of the FID signal [Rid10]. Even T_2 depends on the tissue but generally is shorter than T_1 [VGWdB$^+$99].(Fig. 3.5 (b))

For the generation of an image, it is required also the information of the spatial localization of the signal, meaning the position of the Hydrogen nuclei inside the patient. To do so, MR systems leverage slice selection, frequency encoding, and phase encoding. A magnetic gradient is added along the main magnetic field (in caudal to cranial direction) to perform slice selection, in this way, since the Larmor frequency depends on the local strength of the magnetic field, a narrow band of frequencies will only excite a thin slice of spins through the body. Thus, changing the excitation frequency, another parallel slice will be acquired subsequently. Moreover, using combinations of gradients in all three directions, it is possible to acquire a slice in any arbitrary direction.

Once the slice selection is performed, frequency, and phase encoding permit to identify a specific point within a slice, namely the single pixel. With phase encoding, is intended a short temporary change in the magnetic field applied between the RF excitation and the readout of the signal,

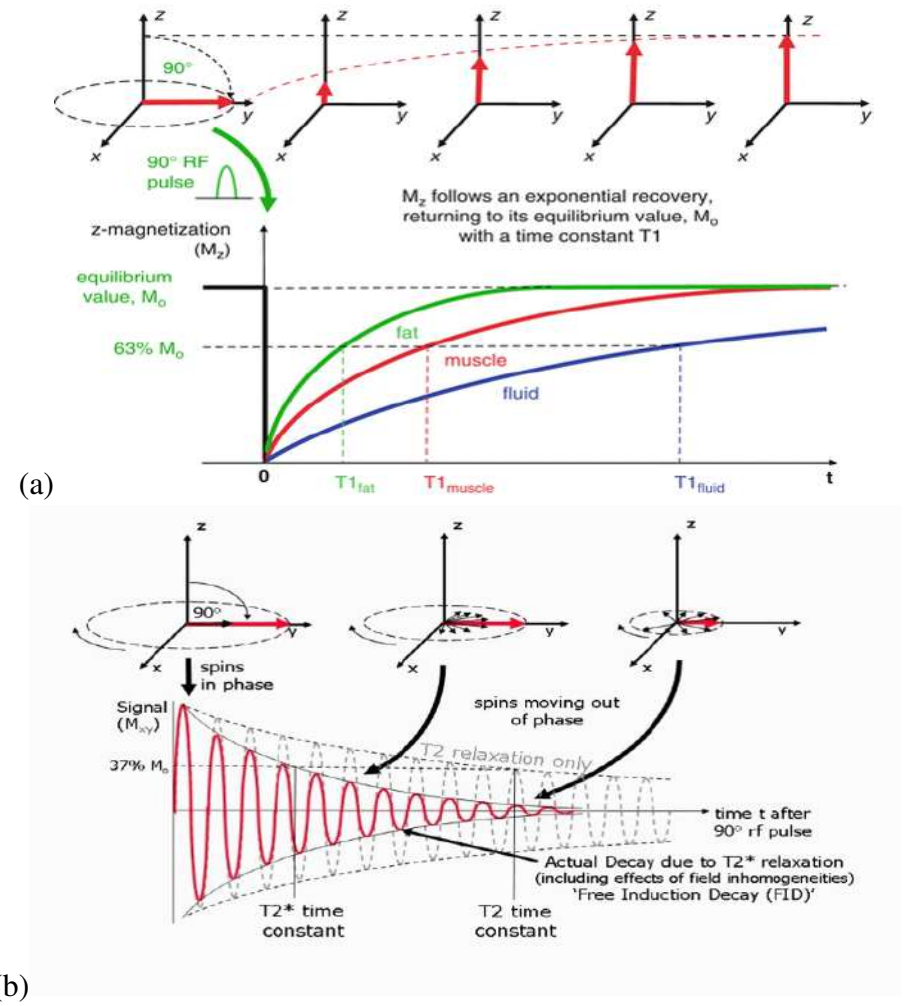

Figure 3.5: (a) T_1 relaxation time [Rid15], (b) T_2 relaxation time [Rid10].

that influences the frequency of precessing resulting in a shift in the precessing phase of the spins, dependent on the duration of this gradient switch. When this process is repeated changing the duration of the temporary gradients, signals with different phase encoding can be acquired. Then, the frequency encoding permits to identify the pixel inside a specific phase encoding. Such frequency encoding is obtained by applying a gradient during the readout of the signal, resulting in a specific shift of the resonance frequency.

The integration of phase and frequency information allows the creation of a grid in which each pixel has a defined combination of phase and frequency codes. *K-space* is the name that has been given to such a grid. Finally, a Fast Fourier Transform, performed in both the frequency and phase directions, converts the data into a curve that represents the intensity of each pixel as a function of the frequency (Fig. 3.6).

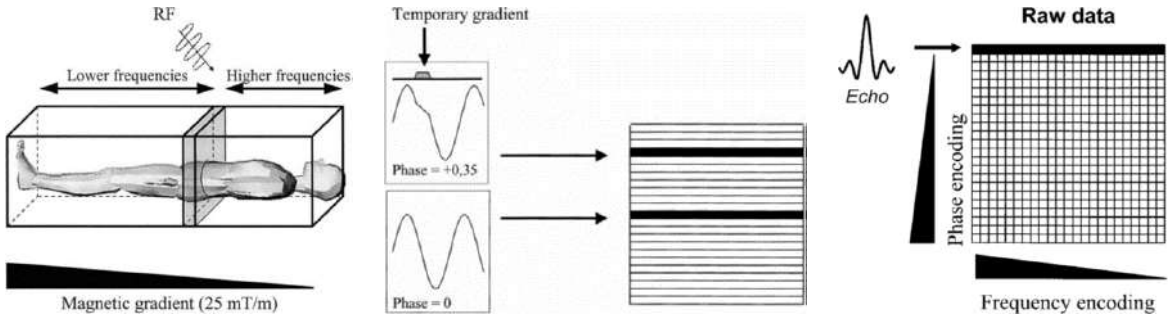

(a) (b) (c)

Figure 3.6: Spatial encoding of MRI images requires:(a) slice selection, (b) phase encoding, (c) frequency encoding applied to identify the location of the pixel emitting the received signal [VGWdB$^+$99].

The evocation of a second AC signal permits to save important acquisition time and to modify the contrast in the images depending on the T_1 and T_2 values of the tissue. For this reason, usually, a second RF pulse is applied in order to flip the spin by $180°$ and reverse the dephasing process. As the spins rephase, the amplitude of the AC signal increases, and this signal, called the echo, is measured at its maximum (time of echo = TE). The kind of MRI techniques that use this combination of a $90°$ and $180°$ pulse to generate the echo signal are called *spin-echo* sequences (Fig. 3.7) [VGWdB$^+$99].

Since T_1 and T_2, are dependent on the specific tissue, MRI is optimal for the contrast between different soft tissues with respect to other imaging techniques. In particular, it permits to regulate the contrast of the resulting image through the control of *Time of Repetition* (TR), namely the time that passes between two repetitions of RF pulses. Indeed, if TR is smaller than the time required for total longitudinal relaxation, then the contrast will be mainly influenced by the difference in T_1 values of the tissues. While, if TR and TE are quite long, the contrast will be depending on T_2 differences. Finally, a combination of long TR and short TE will focus the contrast on the differences in proton density of the tissues [VGWdB$^+$99].

All the parameters and processes that have been described in this Chapter must be considered when acquiring an MRI volume. Part of them is automatically selected by the system, others are set by the expert acquiring the image.

3.2.1 Low-field MRI

As it happens for all the imaging techniques applied in medicine, there are various kinds of MRI acquisition processes from which to choose. Depending on the needs, some are more suited than others. One of the parameters to determine is the strength of the magnetic field of the image scan. Indeed, in commerce, two principal groups of systems are available: with high or low-field

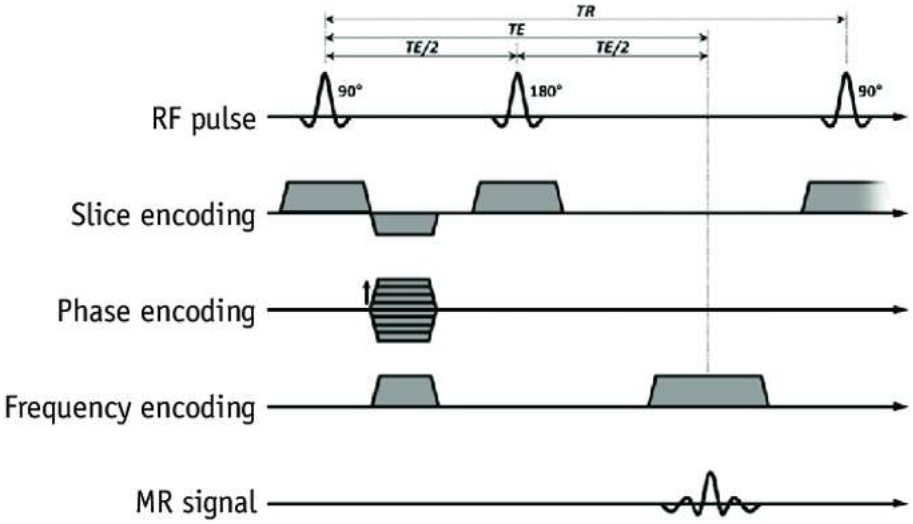

Figure 3.7: [JKP+19] Spin echo typical acquisition sequence.

strength. Intuitively, high magnetic field strength provides additional signal and therefore enables the reduction of imaging time and/or increase spatial resolution [Kle15]. In the following, we will focus on the characteristics of low-field MRI scans, since the data set used for this work has been acquired with such technology. Table 3.1 resumes the principal advantages and disadvantages of low-field MRIs. Moreover, in rheumatology, the carpal district is highly studied and taken into consideration for diagnosis and monitoring purposes through low-field MR images.

The first effect, that a smaller magnetic external field influences, is the Larmor frequency: with smaller B_0 the spin rotation is slower, which is an advantage for some specific application such as mammograms, where the longer spin cycle permits to control better the small-time deviations that change the signal. However, in other applications, such as angiography, this smaller Larmor frequency implies longer acquisition time [Kle15].

A lower field strength influences also the RF signal, which in turn presents a lower frequency, improving the RF pulses tissue penetration. As a consequence, the magnetic field produced by RF (B_1) will be more homogeneous. This characteristic is decisive for a good image quality since it influences directly the spatial resolution. Indeed, spatial encoding is based on the application of gradients and, thus, modulates the local field strength in order to have locally defined resonance frequencies. In this way, with Fourier analysis of the resonance spectrum, each point is represented by a specific resonance frequency. Inhomogeneities in the magnetic field interfere with this process, worsening the image quality [Kle15].

The application of a low external field involves changes in T_1 and, even if with less relevance, also T_2. Indeed, T_1 (longitudinal or spin-to lattice relaxation) shortens along B_0 while T_2 (transversal or spin-spin relaxation) is prolonged. This means that in sequences such as spin-echo (the

Table 3.1: Advantages and disadvantages of low-field MRI scanning systems.

Advantages	**Disadvantages**
Lower RF energy deposition	Lower SNR
Lower energy consumption	No spectroscopy
Better T1 contrast	Inferior spectral fat saturation
Shorter T1 times	
Less dielectric effect	
Low maintenance	
Better patient access/open design	
Less motion artifacts	

so-called T_1 weighted sequences), the signal received from the tissues increases. Moreover, a decrease in T_1 produces a consequent decrease in TR, which will increase the scan speed [Kle15].

The only potential harmful factor of MRI is the *RF energy deposition*, which can induce dangerous tissue heating. The maximum RF energy is limited to a value that causes less than $1°C$ tissue heating. Moreover, the *Specific Absorption Rate*, which expresses the percentage of electromagnetic energy absorbed by the human body when it is exposed to an RF field, must not exceed 4 $W/kg\ body\ weigth$ in 15 min. The SAR increases with the square of the field strength, thus, in lower-field imaging, this problem is less present [Kle15].

An electromagnetic field, such as the one used for magnetic resonance, is composed of an electric component and a magnetic component that oscillate perpendicular to each other and to the direction of wave propagation. The electric component can interact with the tissues as does the magnetic one. This interaction is called *dielettric effect*. At a high level of the magnetic field, the RF shorter wavelength interaction with tissues can create the *dielettric artifacts*, which results in abnormal dark or bright areas. While, with a lower field, the image presents less possibility to show such artifacts [Die].

The relation between signal strength and noise level called *Signal to noise ratio* (SNR) is the key indicator of image quality. The noise must be reduced as much as possible, while the acquisition of the signal must be optimized. Since the resonance signal increases with the field strength, systems with high-fields present higher SNR and, thus better image quality. However, SNR is influenced not only by field strength. A variety of other parameters are important such as receiver bandwidth, echo spacing, and coil design. An optimal set of such a parameter can improve the SNR of low-field MRI scans [Kle15].

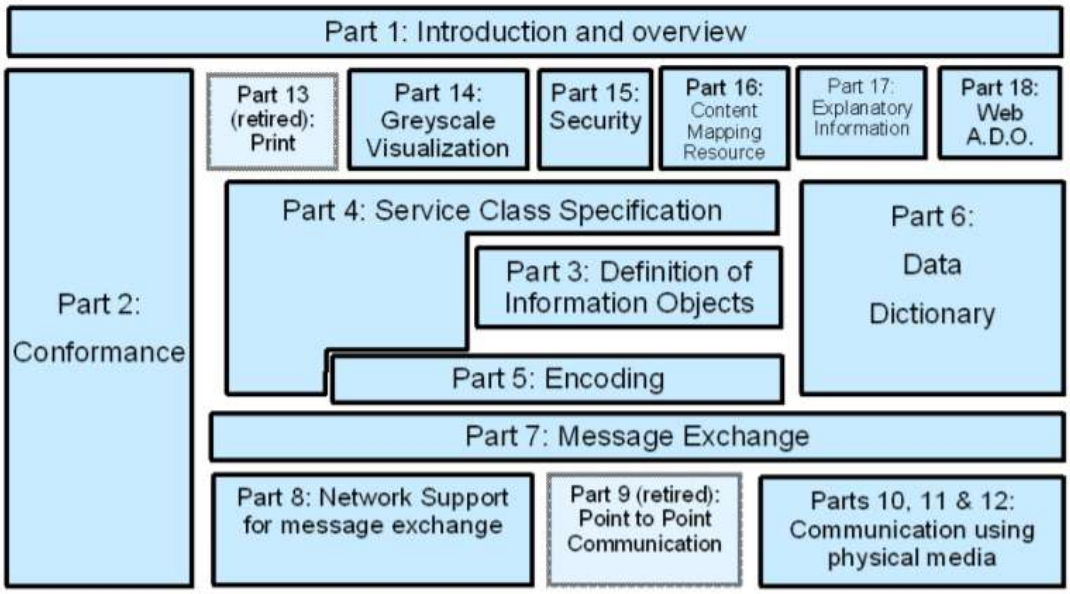

Figure 3.8: [Gib08] DICOM standard multi-document organization.

3.2.2 The DICOM standard

Nowadays, with the development of imaging techniques such as CT, PET, SPECT, MR, and others, the use of numerical technologies is dominant in diagnostic imaging. Thus, the management of medical images is inherently based on informatic technologies, making computers at the core of generation, memorization, transmission, and access to those images. This process of digitalization of images has various advantages. First of all, numeric images memorization permitted a reduction of costs, time, and size of the archiving, that now can handle different imaging modality in a structured and easy to access database with the possibility of easily generate copies of the original image. Also, the transmission of images has clearly improved and permits the reception of the exams at the same time as written texts in a fast and reliable way [CDV12].

The diffusion of images in a numeric form has permitted the application of Computer Graphics techniques to improve the visualization of anatomical structures. Thanks to such methodologies, the fruition of the information contained in the image is easier for the physician or surgeon observing the structure. In order to completely take advantage of all the possibilities that numeric images provide, it was necessary to determine a standard system for the transmission of those images that could be used all over the world. For this reason, nowadays, all the companies supplying equipment for the production of images, have assumed as communication protocol the *DICOM (Digital Imaging and COmmunications in Medicine)* standard, in order to guarantee a high interconnection and interoperation capability [CDV12].

The DICOM standard is composed as a multi-part document made of 18 modules (Fig. 3.8). We will describe briefly the most important parts. Part 3 *Information object definitions* specifies the information objects to be exchanged and the definition of the semantics of each data element. This part is very long due to the various existing imaging modalities, that require many technical parameters. Part 4 *Service Class specifications* describe the services for exchanging information, like the images themselves or other information useful to manage the images. Part 16 *Content Mapping Resource* defines the terminology, specifically how existing terminological resources can be used in DICOM, and how to reuse grouped content items in DICOM Structured Reporting documents. Part 5 *Data structure and encoding* describes how to organize the information objects specified in Part 3 into a linear bitstream, in order to be sent over a network connection or stored in a file. This comprehends all aspects related to image compression. Finally, Part 2 *Conformance* specifies how to claim conformance to the DICOM standard for a particular product, meaning how to write the document called *conformance statement* in detail [Gib08].

This standard not only defines a transmission protocol for images but also regulates the memorization of those images. It is precisely this last aspect that has been relevant in carrying out the research activity of this Thesis. Indeed, the images contained in the data set were provided as DICOM images, meaning that they were saved accordingly to DICOM rules. Together with the image, this standard permits the achievement of different other pieces of information that identify the patient, the exam parameters, and the image itself. Indeed the information of the DICOM element is composed by [CDV12]:

- a tag that identifies the element and the group to which the packet belongs to. Where the group is the DICOM entity associated with the data and the element the type of attribute contained in the packet. As an example, group 0100 identify the patient entity, and in this entity, element 0010 identifies the surname;
- a type indicator that identifies the format of the information memorization;
- the byte length of the transmitted information;
- the real principal information in the format indicated by the previous fields.

Besides the public tag, which is present in all the data saved through the standard, there are also private tags, that are inserted by the specific company, and contain information that depend on the specific implementation. However, such information can be fundamental for the processing and correct visualization of the image [CDV12].

3.2.3 MRI pixel intensity informative content

It is sure, when talking about MRI, to encounter the concept of *weighting*. This term can be seen as a label to describe MR sequences and images and identifies the source of signal differences,

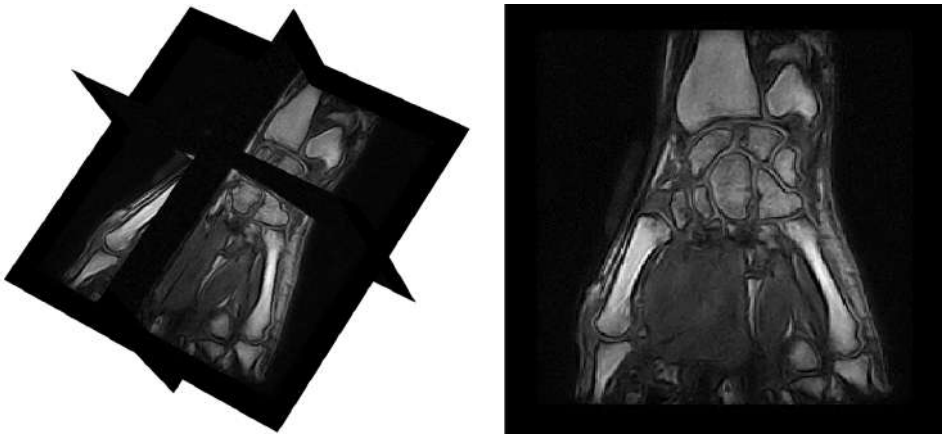

(a) (b)

Figure 3.9: $T_1 - weighted$ low field MRI of the carpal district. (a) 3D view, (b) 2D slice representation.

namely the contrast, seen in an image. Usually, in clinical practice, the weighting concept is described qualitatively. Indeed, an image is said to be weighted for a specific tissue property like T_1, T_2, or proton density when the most important source of contrast on the image is that specific property. However, the relation between tissue properties and the weighting sequence or image can not be immediate. This means that even if an image is defined as $T_1 - weighted$, only part of it may be, in fact, $T_1 - weighted$ while other parts can be $T_2 - weighted$ or $\rho - weighted$ (where ρ is the proton density) or even without any weighting. Moreover, assuming that the whole image is $T_1 - weighted$, the various tissue can present a different degree of weighting.

It must not be forgotten that the term *weighting* is usually associated with both the image and the sequence, even if in real practice the weighting of a sequence may differ from that of the image produced by it.

Despite these difficulties, the concept of weighting is fundamental in MR imaging since it relates the contrast on images to differences or changes in tissue properties, which highlight and explain the effects of the disease. As a result, weighting provides an essential link between observed contrast in diseases and pathologic processes believed to be responsible for the contrast [YBH$^+$10]. Indeed, keeping in mind the different aspects of the weighting terminology just described, we will describe the characteristics of $T_1 - weighted$ images (the ones present in the data set used in this work). Going deeper into a quantitative differentiation of the various weighting methods is beyond the scope of this thesis, thus, we will rely on the concept that some excitation sequences, appropriately designed, can emphasize the FID dependency from the three parameters: ρ, T_1, and T_2, which means controlling the contrast of the image. In particular, $T_1 - weighting$ sequences tends to present a short time of echo (TE) and short time of repetition (TR) and relies on the longitudinal relaxation of tissues net magnetization vector, namely the spin-lattice relaxation

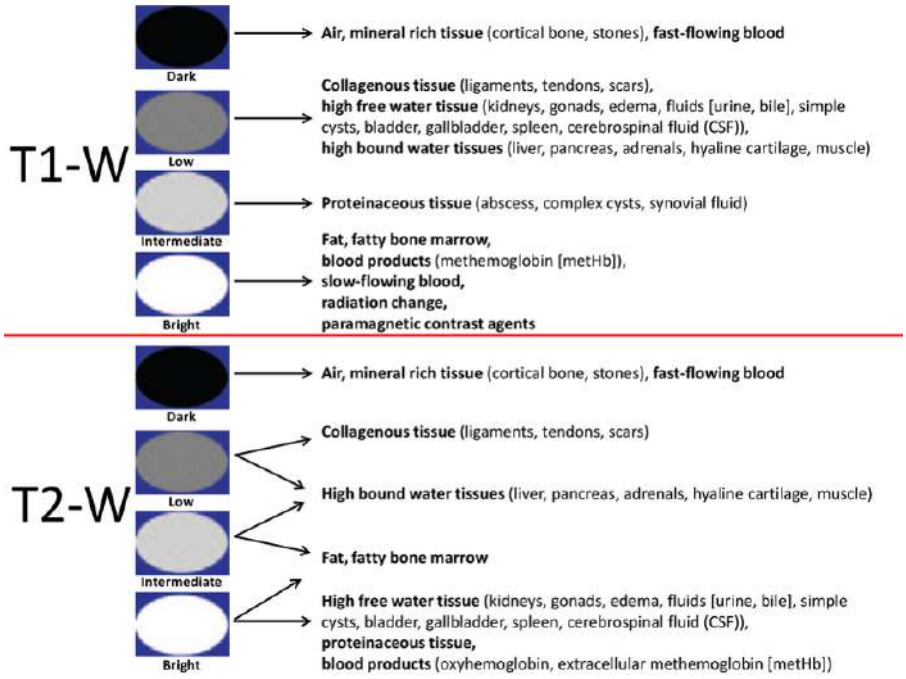

Figure 3.10: $T_1 - weighting$ and $T_2 - weighting$ pixels/voxels intensities in MRI.

time. Since fat tends to realign quickly its longitudinal magnetization to B_0, it appears bright in these images. Water and collagenous tissues, instead, present slower realignment and thus are darker. Finally, tissues that present a high portion of minerals result in black.

Our work is focused on the analysis of the bones and articulation-related tissues of the most analyzed districts in rheumatology: the carpal district. In Fig. 3.9, we show an example of the raw images used in this work. The final result of the scan presents bright areas in correspondence of the internal tissue of the bone and in the bone marrow since those structures are characterized by a high percentage of fat. The final part of the bone toward the exterior, namely the cortical bone, instead is rich in minerals and thus it presents as a back region contouring each bone. Outside the bone then, with this low resolution, the synovial tissue is not clearly distinguishable from the cortical bone but it is also represented by as highly dark voxels. The ligament and tendons, which are prevalently collagenous tissues, result in different dark and intermediate grey-levels (Fig. 3.10).

3.3 The carpal district

Since in the study and diagnosis of rheumatic diseases the carpus is one of the most affected districts, it is useful to understand its anatomy. In the following, we discuss the main character-

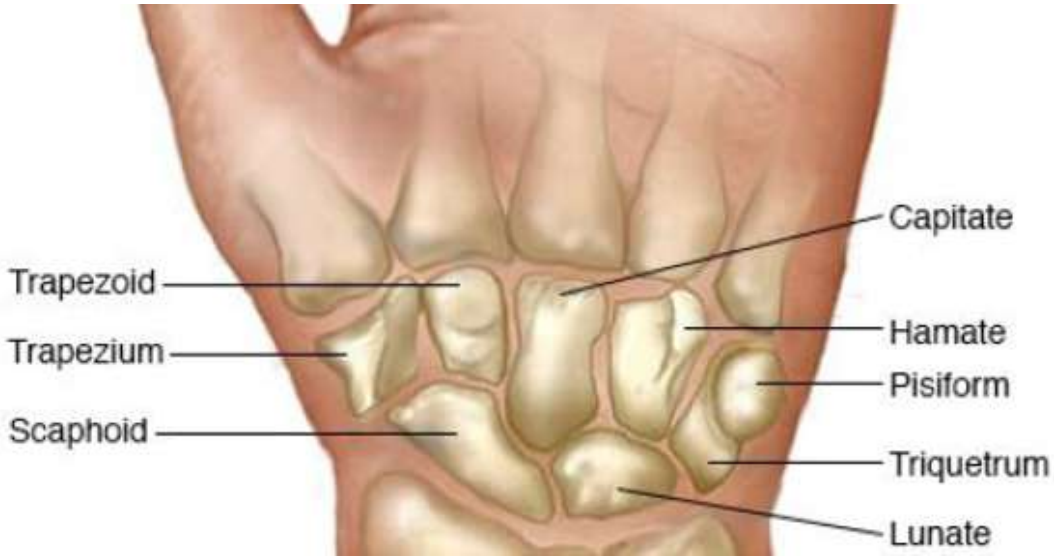

Figure 3.11: Wrist bones.

istics of the anatomical structures of the carpal district and its functionalities. The final aim is to identify the right amount of information required to provide support in the diagnosis and monitoring of rheumatic pathologies, in order to bring interesting insights into the data interpretation process. For this reason, we need to understand clearly what are the anatomical features and their attributes that results important for the clinicians.

The carpus is the group of eight bones and associated soft parts forming the joint between the forearm and the hand, articulating with the radius, with the ulna, and with the five metacarpal bones [Dic00] (Fig. 3.11). The eight carpal bones are arranged in 2 rows in a lateral to medial direction on the palmar surface:

- *proximal* row: scaphoid, lunate, triquetrum, pisiform bones;
- *distal* row: trapezium, trapezoid, capitate, hamate bones.

In general, each carpal bone presents a quite spherical shape and different facets in order to articulate with several nearby bones. Particularly, the bones belonging to the proximal row are convex proximally, and concave distally, and the bones in the distal row are convex proximally and flat distally [Ban16].

The carpus articulation is one of the most complicated human joints, indeed it comprehends

- *intercarpal* articulations: regard the articulations among the contiguous bones of the distal row and the proximal row;

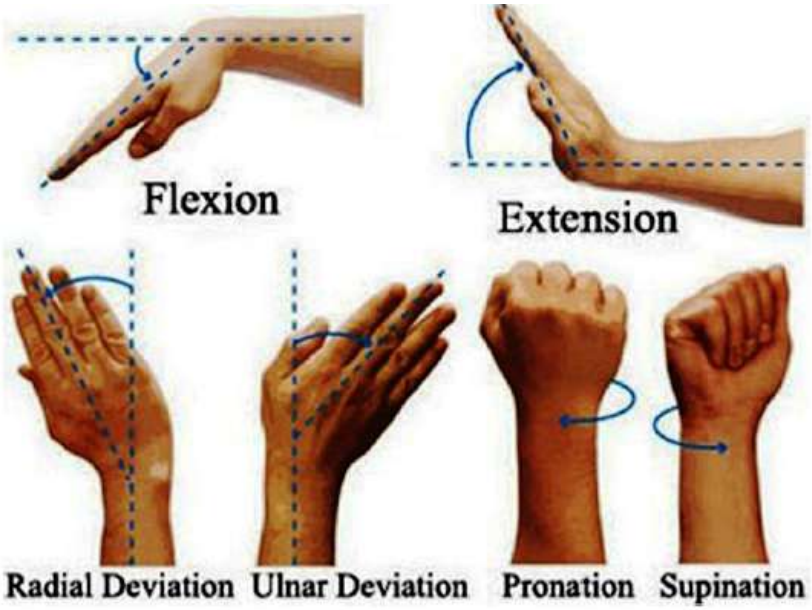

Figure 3.12: Wrist movements.

- *radiocarpal* articulations: identify the articulations between the proximal row and ulna and radious bones;
- *carpo-metacarpal* articulations: relative to the articulation between the distal row with the five metacarpal bones;
- *mid carpal* articulations: involve the articulation between the distal and the proximal rows.

Such a high number of different articulations is the main reason for the remarkable mobility ad fine movement allowed to this district (Fig. 3.12).

Ligaments perform a major role in stabilizing the whole carpus, indeed ligaments hold carpal bones together despite the various articulations and movements. For this reason defects in ligaments, e.g, injury, or detachment, can cause carpal instability. Carpal ligaments can be categorized as (Fig. 3.13):

- *extrinsic* ligaments, which bridge carpal bones to the radius or metacarpals;
- *intrinsic* ligaments which originate and insert on carpal bones.

Among the ligaments involved in the carpal district, the bigger are the ulnar collateral which connects the ulna and triquetral bones, and the radial collateral which connects the pisiform and radius to the scaphoid.

Figure 3.13: Intrinsic (right) and extrinsic (left) ligaments of the wrist.

The muscles that act on the wrist movements originate in the forearm and are extensors of the carpus, extensors of the fingers, flexors of the carpus, and flexors of the fingers. Only one long tendon unites such muscles to the hand and passes through the wrist. While three nerves cross the wrist going from the forearm to the hand: the radial nerve, median nerve, and ulnar nerve.

Important information to be provided to clinicians are related to the patient-specific positioning and morphology of the anatomical district and functional landmark areas on the carpal bones. Articulation regions, prominent features, ligaments origin, and insertion sites can all be considered valuable landmarks. However, the significance of different sorts of anatomical landmarks relies upon the contextual investigation. For the carpal district, one of the most relevant types of anatomical landmarks, are articulation regions and the ligament origin/insertion sites, since they relate to the functionality of carpal anatomy. Moreover, in both ligaments and articulations regions, the early signs of rheumatic pathology can be interpreted by experts in the field in order to have a faster diagnosis and a tailored treatment plan.

3.4 Rheumatic pathologies

Rheumatic pathologies reside among the oldest diseases recognized by the medical community. The classification of these pathologies can be difficult since their etiology is partly unknown and their clinical representation is quite heterogeneous. However, the impact of those illnesses on both individuals and society comprehends a decrease in the quality of life, a loss in productivity, and an increased cost in healthcare. Those reasons brought to the necessity of controlling such

Figure 3.14: Rheumatoid Arthritis anatomical deformation.

diseases, given also the progressively aging of in the population [San00]. The term *rheumatic diseases* does not possess clear limits, indeed more than 100 different conditions are labeled as rheumatic diseases.

Rheumatoid Arthritis (RA) is one of the most common and consists of a chronic inflammatory disorder that affects the lining of joints, causing a painful swelling that can eventually result in bone erosion and joint deformity (Fig. 3.14). This pathology starts, usually, from the small joints and attacks multiple others throughout the body. Nowadays, a significant number of person presents RA especially in their wrists, which makes it difficult for them to perform daily activities, given the importance of a well-functioning carpal district in everyday life movements. RA is more common among women than men and can present itself at an early age but is more common among elderly subjects. Experts confirm that RA disease can be characterized by the morphological changes of carpal bones and the whole district. Early-stage symptoms are: marginal and central bone erosions, giant synovial cysts, regional osteoporosis, and widened joint space. Late signs are bony fusion, destruction of joint spaces, destruction of bone ends, and joint deformity. Rheumatologists usually check the distribution of the inflamed joints as the first step in RA diagnosis, since the presence of inflammation in the joint helps to distinguish Rheumatoid Arthritis from other common types of arthritis that are not inflammatory, such as osteoarthritis. The chronic inflammation leads to the formation of the *synovial pannus* with bone eroding capacity. Usually, in RA, erosions are marginal and localized at the *bare area*, the bone surface within the synovial space, which is not protected by cartilage [TCB$^+$15].

The data set contains patients with PSA, an inflammatory disorder characterized by the association of cutaneous psoriasis and inflammatory arthritis [TCB$^+$15]. PSA can present different

forms: a symmetrical polyarthritis similar to RA, an oligoarticular form, a spondylitic form characterized by axial involvement, and a mutilans form. Bone erosions, unlike the ones observed in RA, are not in the marginal area but in the central region of the articular surface.

Gout is another rheumatoid pathologies examined in the data set. It is a metabolic disease correlated with hyperuricemia, and characterized by recurring acute arthritis at first, usually monoarticular, and later by chronic deforming arthritis. The characteristic lesion of the chronic stage is called *tophus* and consists of nodular deposits of monosodium urate monohydrate crystals that can be found in cartilage, articular and periarticular tissues. The erosions of the gout are well-defined, punched-out erosion, usually adjacent to the tophus, with overhanging edges.

PR, instead, is a particular form of inflammatory arthritis characterized by sudden and rapidly developing arthritis episodes leaving no radiographic change. Such pathology may develop in RA. Finally, among the pathologies present in the data set, SSC, represent a chronic systemic connective tissue disorder. It is characterized by diffuse fibrosis of the skin and internal organs. Joint involvement is frequent and can present distal phalange resorption, demineralization, joint space narrowing, and erosions [TCB$^+$15].

Nowadays, two of the most frequently used imaging techniques for the study of rheumatic diseases are Computed Tomography (CT) and Magnetic Resonance (MR). Since MR permits to acquire images non-invasively, it is commonly used both in diagnosis and monitoring phases. Indeed, the use of imaging techniques represents a step to confirm the diagnosis and localize possible erosion or osteoporosis. The origin of such erosive degeneration differs according to the particular undergoing pathology, but the result is an anomalous change in the tissues' composition and, as a consequence, in the bone morphology. However, visual inspection is a time-consuming manual process, and inter-operator variability may influence the analysis. What can help physicians and rheumatologists in the diagnosis and differentiation of rheumatic diseases is an accurate and efficient system for the visualization of anatomical and physiological changes that involve the disease. Moreover, experts confirm that the automatic identification of particular landmarks, that are most subjected to early symptoms (ligament insertions and articulation areas), could help to obtain early and more patient-specific diagnosis.

Chapter 4

Grey-levels Mapping

4.1 Aim of the hybrid representation

The first aim of the integration method is to provide an *efficient* and *augmented* visualization tool for supporting the diagnosis and monitoring of rheumatic pathologies. With the term *augmented* we intend the possibility to add volume context information to the 3D shape model visualization of anatomical structures. Typically medical visual data are approached through *surface rendering* or *volume rendering*.

In particular *3D volume rendering (3DVR)* is suitable for semitransparent object. Usually, it is used as a visualization method where three-dimensional volumes are mapped to density and color values in order to allow the viewer to recognize shapes and patterns within a material that, in origin, was opaque [SC18]. Thus, the volume visualization provides a way to see through the data, revealing complex 3D relationships [MB05]. Indeed, one of the great advantages of 3DVR is that it can provide all the necessary information in a single radiologic study in cases that previously, with 2D representations, required two or more studies. 3DVR also permits to interactively explore the imaging data and, thus, allows the clinician to assess more information on the patient. All 3D-rendering techniques reveal a 3D volume of data in one or more 2D planes, conveying the spatial relationships with the use of visual depth cues [DDM$^+$19]. Generally, such volume rendering techniques can be used also for the visualization of the 3D volume with its original grey-levels (Section 4.2) (Fig. 4.1(a)). *Surface rendering*, instead, is useful for the 3D visualization of objects' surfaces starting from a binary image (which is the result of a segmentation process). In this case, the value of the 3D reconstruction goes beyond the sole visualization: indeed, a reconstruction, is particularly useful for the analysis of morphological characteristics. The 3D models, contrarily to volume rendering, explicitly represent the shape of the analyzed structure (Section 4.2). Surface rendering is based on surface mesh representations instead of mapping volume data directly to the viewport, as happened in volume rendering (Fig. 4.1 (b)).

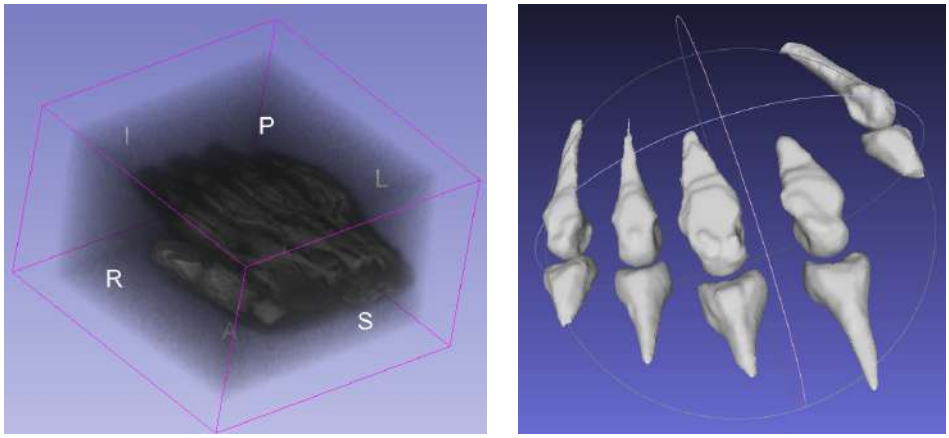

(a) (b)

Figure 4.1: Volume rendering (a) and surface rendering (b) of the hand.

The main reasons for the necessity of a surface rendering in the first place were basically two: it was faster than volume rendering, since a mesh has a significantly lower memory footprint than a volume data set, and it provided clearly recognizable images with depth cues such as those caused by illumination [PB13]. These original advantages lost their relevance with the introduction of GPU rendering. Thus, even advanced volume rendering of typical medical data sets can be performed in real-time. However, in the last years, the importance of surface rendering has expanded in different areas such as biophysical simulation, interactive 3D visualization, and 3D printing. The latter application regards the modeling and printing of relevant portions of human anatomy to support in-depth collaborative discussions of treatment options [PB13].

Thus, the development of a new visualization modality that provides a hybrid between the two rendering techniques was the very first goal of the integration proposed in this work (Section 4.3). A correspondence map between the volume image and the surface model is one of the key elements of the integration method, leading to the visualization of the image grey-levels directly on the 3D segmented surface. For this reason, we refer to the integration method as *grey-levels mapping*.

The therm *efficent*, instead, refers to the possibility to realize this integration exploiting a simple methodology (the results of such methodology are presented in Section 4.4). Indeed, in clinical applications, the simplicity aspect of the innovation is what brings such innovation to be actually applied in practice. One reason may reside in the possibility to perform faster and less complicated integrations with already existing tools. Moreover, highly complicated solutions often require longer training for the final user. For these reasons, the efficiency term relates to the augment of information provided by the approach to its simple implementation.

Since quantitative parameters can be extracted from both 3D models, regarding the morphology of the structure, and from the 3D volume image, regarding the composition of the tissue, the

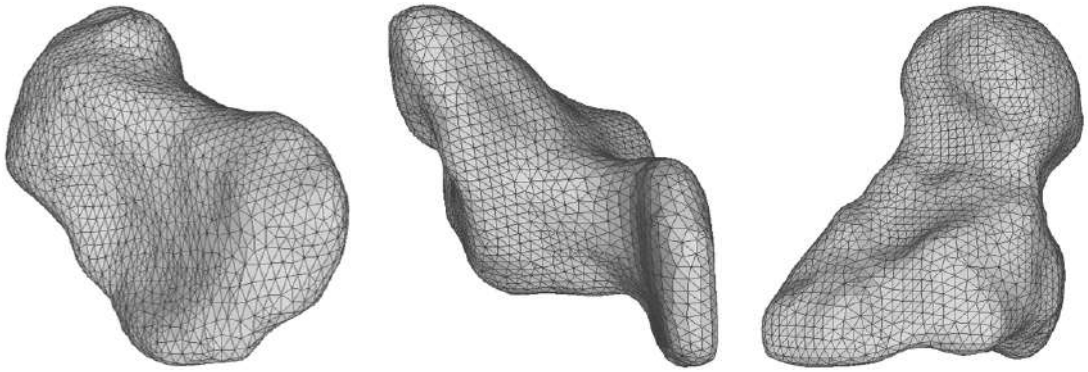

Figure 4.2: Bones surfaces represented as triangular meshses.

integration of the two methods has been thought not only for visualization and rendering purposes but also for a combined analysis to support diagnosis and monitoring processes. Indeed, the presence of information from both the volume and the model, permits an integration between shape analysis and image processing techniques, bringing to a quantitative evaluation of the overall exam information. Such quantitative analysis has the scope of helping physicians to explore the particularly interesting region or symptoms related to the pathology. Thus, the other goals of the integration method regard the characterization of the carpal district anatomy and an evaluation of the segmentation result in terms of tissue distribution around the bones surfaces, as we will present and discuss in Chapters 5 and 6.

4.2 The bridge data sctucture

The key for correct and efficient integration of information between 3D surface models (Sections 4.2.1) and volume images (Section 4.2.2) is a data structure that could be intended as a bridge between these two different data. The scope of the data structure is, indeed, to permit the exploration of the volume image in the neighborhood of the surface, a task that requires the correct location of the two data in the space.

4.2.1 Surface mesh

A surface in Computer Graphics is commonly defined as an orientable continuous two-dimensional manifold embedded in $\mathbb{R}^3$, which describes the boundary surface of a non-degenerate 3D solid. Where non-degenerate implies the absence of thin parts or features, such that the *interior* and *exterior* of the solid are properly separated [BPK+07].

Among the different ways to represent a surface, one of the most used, studied, and diffused is

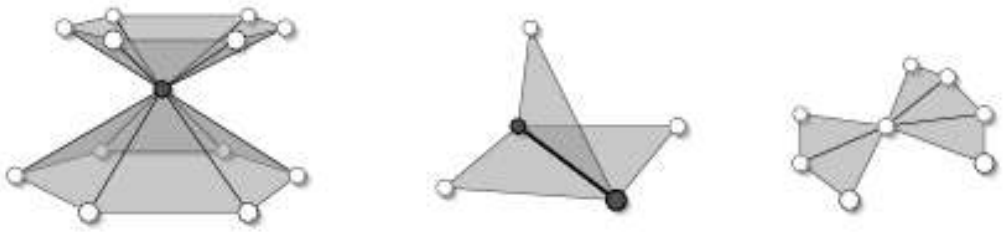

Figure 4.3: [BPK$^+$07] Non-manifold vertex in case of two-surface sheets meeting on it (left). Non-manifold edge with more than two incident faces (center). Non-manifold configuratin handled by most data structure (righ).

through a triangle mesh, as in the data set we used for this work.

Triangle meshes can be considered as a set of triangle without any particular mathematical structure, as happes in different geometry processing algorithms. However, each triangle defines a linear segment of a piecewise linear surface representation, through its barycentric parametrization (Fig. 4.2). Indeed, every point $\mathbf{p}$ inside a triangle $[\mathbf{a}, \mathbf{b}, \mathbf{c}]$ can be considered as a barycentric combination of the corner points [BPK$^+$07]:

$$\mathbf{p} = \alpha\mathbf{a} + \beta\mathbf{b} + \gamma\mathbf{c}. \tag{4.1}$$

With $\alpha + \beta + \gamma = 1$. If we choose an arbitrary triangle $[\mathbf{u}, \mathbf{v}, \mathbf{w}]$ in the parameter domain, we can define a linear mapping $f : \mathbb{R}^2 \rightarrow \mathbb{R}^3$ with [BPK$^+$07]:

$$\alpha\mathbf{u} + \beta\mathbf{v} + \gamma\mathbf{w} \rightarrow \alpha\mathbf{a} + \beta\mathbf{b} + \gamma\mathbf{c}. \tag{4.2}$$

A triangle mesh M consists of a geometric and a topological component. The topological component can be described as a graph structure (simplicial complex) with a set of vertices $V = v_1, ..., v_V$ and a set of triangular faces connecting them $F = f_1, ..., fF$, $f_i \in V \times V \times V$ [BPK$^+$07]. Sometimes, however, the connetivity is represented in terms of the edges of the respective graph for efficiency reasons. $E = e_1, ..., e_E$, $e_i \in V \times V$. Associating a 3D position $\mathbf{p}_i$ to each vertex v_i the triangle mesh is embedded into $\mathbb{R}^3$:

$$P = \mathbf{p}_1, ..., \mathbf{p}_V, \mathbf{p}_i := \mathbf{p}(v_i) = \begin{pmatrix} x\,(v_i) \\ y\,(v_i) \\ z\,(v_i) \end{pmatrix} \in \mathbb{R}. \tag{4.3}$$

In this way each face $f \in F$ corresponds to a triangle in the 3D space, specified by its three vertex positions. The resulting polygonal surface is still continuous, consisting of triangular pieces with linear parametrization functions [BPK$^+$07].

A triangle mesh is described as *two-manifold* if it does not contain non-manifold edges, non-manifold vertices, nor self-intersections. Where a non-manifold edge is defined as an edge having more than two incident triangles, while a non-manifold vertex is present when two surface

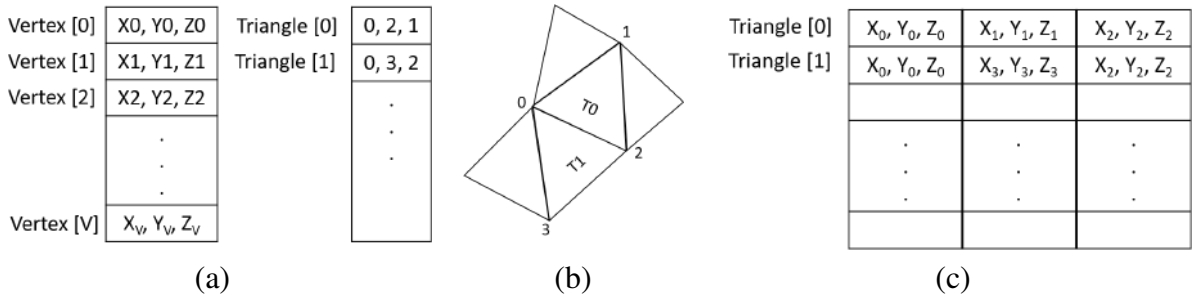

Figure 4.4: Mesh description methods. (a) Indexed triangle sets option. (b) Toy example of the correspondent mesh. (c) Description of the same mesh through list of triangles.

sheets are compressed together at that vertex. Non-manifold meshes create a problem for most algorithms since around non-manifold configurations there is no well-defined local geodesic neighborhood (Fig. 4.3). Thus, in this case, it is necessary to handle that non-manifold vertices/edges prior to the application of the algorithm. Similar situations were present during the data preparation for the integration algorithm and have been solved as will be described in the next Paragraph.

The relation between the numbers of vertices (V), edges (E) and faces (F) in a closed, connected and structured mesh is given by the *Euler formula*:

$$V - E + F = 2(1 - g). \tag{4.4}$$

Where g (genus) represents the number of handles of an object and usually is small with respect to the number of elements. Thus, the right-hand side of the equation can be assumed as zero. With this premise, and since each triangle is surrounded by three edges and that each edge is incident to two triangles, then:

- the triangles are twice the vertices: $F \approx 2V$,
- the edges are three times the vertices. $E \approx 3V$,
- the average vertex number of incident edges is 6.

Mesh cleaning and repair It is important to consider the relation expressed by the Euler formula (Equation 4.4) when analyzing the data structure or file format that is used for the mesh description. Since wrist bones are particularly small, a mesh describing them is supposed to comprehend a number of triangles in the thousands. Even in this case, in the data organization phase, it was necessary to clean the files describing the mesh, since the structure used in the original data was extremely redundant. Indeed, usually, one of the most efficient ways to represent

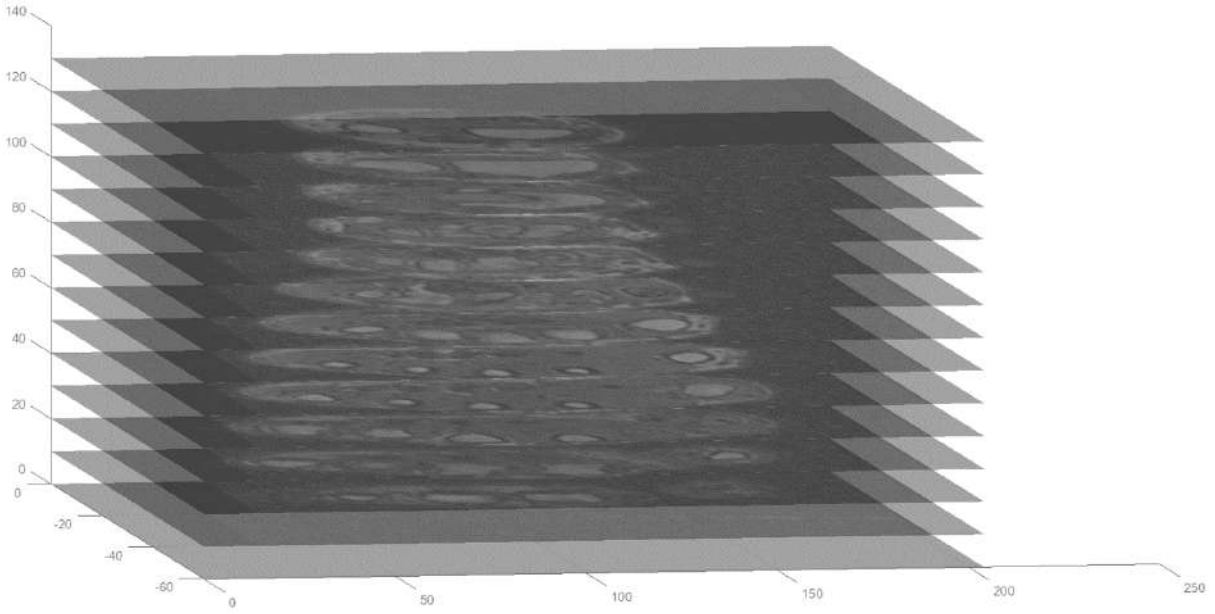

Figure 4.5: 3D MRI volume.

the mesh is through *indexed triangles sets*. In this kind of representation, the mesh is described through the use of two different lists: the first containing all the vertices 3D coordinates followed by the list of triangles, described by triplets of the indices of the precedent list (Fig. 4.4 (a), (b)). The set of vertex coordinates describes the geometry of the mesh, from which it is possible to extract information like the volume surrounded by the surface or the total surface extension. The list of triangles, instead, is commonly referred to as connectivity and describes the adjacency relations. From this connectivity, it is possible to extract information like the presence of boundaries, the genus, or the manifoldness. Another way to describe a mesh is through the use of *separate triangles*. In this case, each separate triangle is described through the use of its vertices coordinates (Fig. 4.4 (b), (c)). This means that every element of the list consists of the 3D coordinate of each vertex composing the triangle. The first problem of this kind of representation is a high waste of space since each vertex is stored 6 times, while in the indexed triangles sets each vertex is identified just one time. Indeed, considering that on average there are 2 triangles per vertex, 3 vertices per triangle, 3 coordinates per vertex, and that to store the information of a coordinate are required 4 bytes, the memory space involved can be high. Not to mention the relevant slowdowns that an algorithm could encounter with such data description. Moreover, in this way the adjacency is not explicit, making it difficult to search for neighbors on the surface.

In our data set, each mesh was originally saved through the use of separate triangles. Indeed, it was very redundant and affected the algorithm performances. Thus we developed an automatic conversion function in order to convert triangle strips into the indexed triangle set. The function identifies the repetitions in the list of vertices and their index. After the elimination of the repeti-

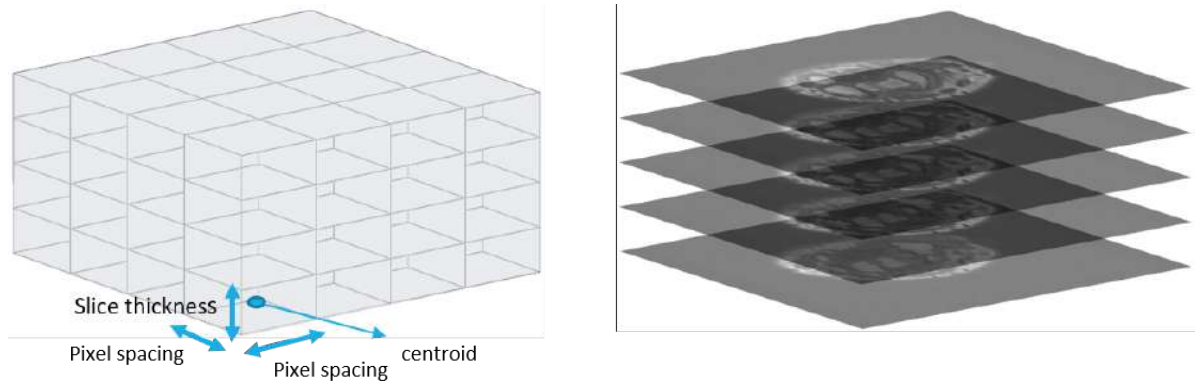

Figure 4.6: Analogy between the regular 3D grid describing the volume and the 2D stack of slices composing the volume MRI.

tion, an opportune modification of the connectivity through the index information is applied, as well as an update of the other vertices indexes, in order to obtain a final explicit connectivity list.

With the term *model repair*, is intended the task of removing artifacts from a geometric model in order to produce an output model that is suitable for further processing. Where the definition of what "model", "artifact", "suitable for further processing" highly depends on the problem at hand. Usually, there is no single algorithm that is applicable in all situations [BPK+07].

A general classification of repair algorithms consists in *surface-oriented* or *volumetric* methods. Surface oriented algorithms operate directly on the input mesh and try to explicitly identify and resolve artifacts on the surface. These algorithms perturb the input model only minimally and can preserve the model structure in areas that are not involved by the artifacts. In particular, structure encoded in the connectivity of the input or material properties associated with triangles or vertices are usually well preserved [BPK+07].

Volumetric algorithms, instead, convert the input model into an intermediate volumetric representation from which the output model is extracted. With volumetric representation, is intended any kind of partitioning of space into cells that allow each cell to be classified as either being inside or outside. Then, the interface between inside and outside cells defines the topology and the geometry of the corrected model. Due to their very nature, volumetric representations do not allow for artifacts like intersections, holes, gaps or overlaps, or inconsistent normal orientations. Moreover, the absence of complex edges and singular vertices can be guaranteed depending on the type of extraction algorithm. Volumetric algorithms are typically fully automatic and usually, they can be implemented very robustly. In particular, the discrete neighborhood relation of cells permits to extract a consistent topology of the restored model. On the downside, given the conversion to and from a volume, a re-sampling of the model is required and often introduces aliasing artifacts, loss of model features, and destroys any structure that might have been present in the

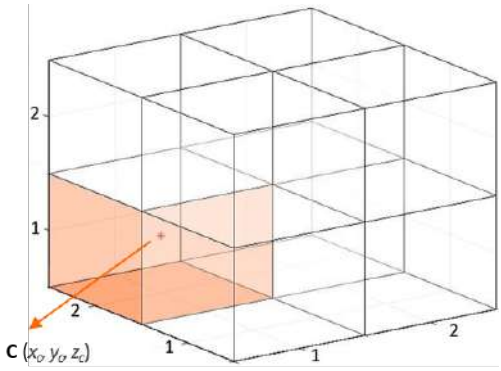

Figure 4.7: Data structure of the input voxel grid. $\mathbf{V}(i, j, k)$ is the intensity of the voxel (i, j, k), where i, j, k are the indices of the intervals on the X, Y, Z axis used to generate the grid structure; $\mathbf{c}$ is the centroid of the voxel with coordinates (x_c, y_c, z_c).

connectivity of the input model. Furthermore, the number of triangles in the output of a volumetric algorithm is usually higher than the one of the input model, requiring a post-processing step to reduce this redundancy. Another drawback is that the quality of the output triangles often degrades and has to be improved afterward. Finally, volumetric representations are quite memory consuming [BPK+07].

Since in our data set case, the artifacts were limited only to non-manifold edges, their correction directly on the surface was more than enough, without the need for volumetric algorithm implementation. Moreover, not all the models present in the data set showed artifacts, thus the number of correction to be made were a totally controllable number. For these reasons, we based our search for such non-manifold edges on the values of the normal to the surface on the vertices. Typically surface normal whose components were exactly equal to 0 in each direction, could indicate an artifact. Thus, every mesh was scanned for the presence of such anomalous surface normals, that, if present, were located onto the surface. Once the exact position of the potential artifact was identified, then through the use of Meshlab© tools, it was manually corrected, and the new mesh description was saved.

Since the surfaces in our data set are obtained by experts, we consider them as ground-truth without applying further processing, such as smoothing and re-meshing. Thus, we limited the changes on the meshes to the cleaning and repair just described. Avoiding other processing can maintain all the information included by the physicians without alteration in bones' shape. This, in turn, avoids the accidental insertion of deformations due to the mesh processing. Moreover, this approach prevents from the elimination of actual deformations which are highlighted in the original meshes obtained by the experts.

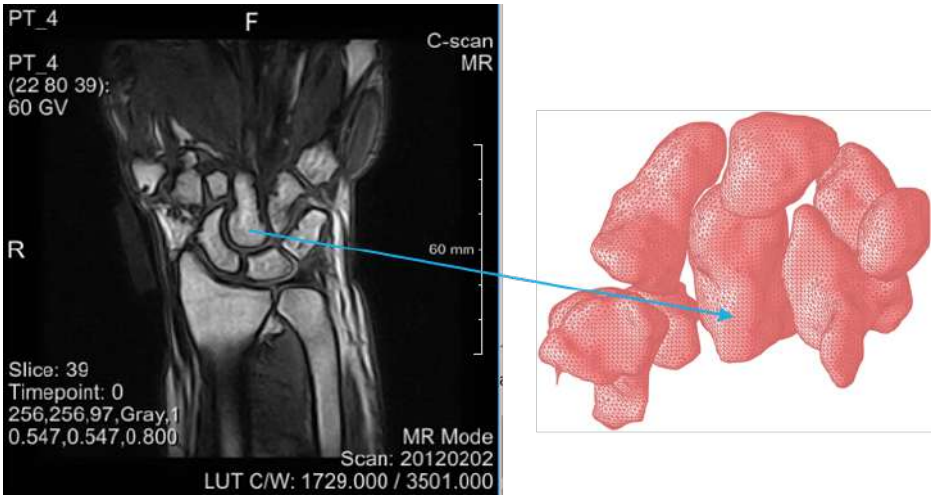

Figure 4.8: Main idea: map the grey-levels of the image voxels onto the segmented surface through a volume-surface correspondence map, which defines a grey-level texture on the surface. The texture links the image context to the 3D geometric representation of the segmented shape.

4.2.2 Volume image

Medical images such as MRIs are a typical example of volume data generated by sampled data of real objects or phenomena. The volumetric data are treated usually as a set $\mathbf{V}$ of samples (x, y, z, v), representing at each 3D location (x, y, z) the value of some property of the data. If v can assume just two values, such as 0 indicating the background and 1 indicating the object, then the volume is called *binary*. However, if the data can assume different values, then the volume is *multivalued*, where v describes some property of the data such as density, color heat, or pressure. Moreover, the value v may be a vector, as in the representation of the velocity at each position [Kau96]. In our case, v is multivalued and represents the tissue composition given by the MRI scan. The DICOM volume is constructed by a stack of 2D slices that, together, form the whole volume. Here the term *stack* refers to a collection of 2D slices obtained by a multislice acquisition characterized by the same orientation (Fig. 4.5).

The result is that $\mathbf{V}$ can be defined on a *regular grid*, meaning that the samples are taken with regularly spaced intervals along all the three orthogonal axes [Kau96]. This implies that the values of $\mathbf{V}$ an be stored in an array, called usually *volume buffer* or *cubic frame buffer* or even *3D raster*. Thus, V is the array of values $\mathbf{V}(x, y, z)$ defined at grid locations. The region surrounding each sample and presenting a constant value is called *volume cell* or *voxel*. Each voxel is a rectangular cuboid with six faces, twelve edges and height corners [Kau96] (Fig. 4.6). Information regarding the dimension of the volume, of the single slice as well as the orientation of the scan, can be found inside the tag of the DICOM header (Section 3.2.2). From those pieces of information, it is possible to understand if we are in presence of an isotropic or anisotropic

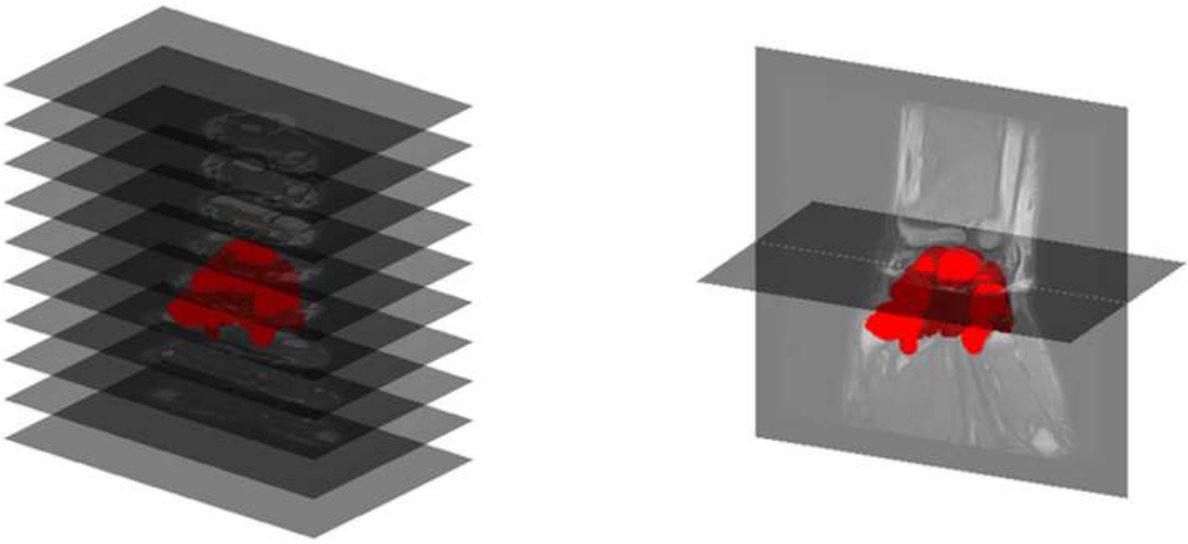

Figure 4.9: Initial visualization: superimposition of the volume image and the surface model.

scan. Particularly, looking at the *Slice spacing* attribute it is possible to understand how big is each pixel dimension in space. Moreover, the *thickness* attribute provides information on the distance between two slices. All this information together, supply the extensions of a voxel in all the space dimensions. If such extensions are equal in every dimension, then the volume is *isotropic*, if one or more of the dimensions are different from the others then we talk about an *anisotropic* volume.

The image volume can be therefore thought also as a grid of voxels, each having dimension equal to *x-spacing* $\times$ *y-spacing* $\times$ *thickness*, with a total number of voxel equal to $N \times M \times R$ where M is the number of pixels in the x direction, N the number of pixels in the y direction and R the number of pixels in the z direction. Given all these premises, the solution to correctly locate the volume image in the space and to navigate the volume is to load the DICOM image into a 3D grid structure whose elements have the same dimension as the image voxels (Fig. 4.7). In this way, every grid cell has its 3D coordinates to locate it in space and each grid cell is associated with a voxel and its grey-level.

Under these assumptions, $\mathbf{V}(i, j, k)$ is the volume voxel associated with the $i - th$, $j - th$ and $k - th$ interval along the X, Y, and Z axis, $\mathbf{c}$ is the centroid of the voxel with coordinates (x_c, y_c, z_c).

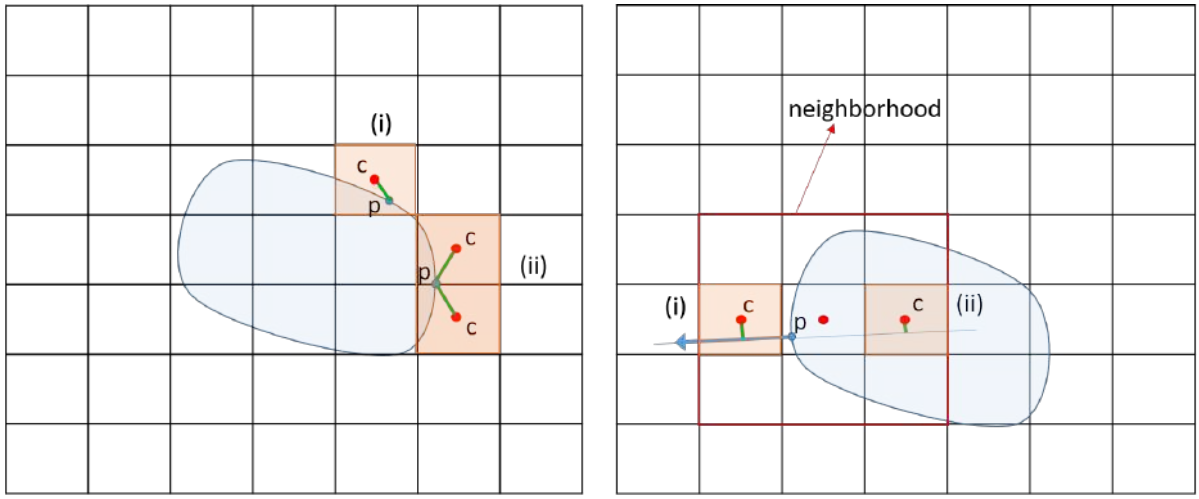

(a) (b)

Figure 4.10: Vertex-voxel correspondence identification. Orange cells are the correspondences between the volume grid element (**c**) and a surface vertex (**p**), computed to obtain different mapping: (a,i)) Euclidean correspondence when the vertex lays strictly in a voxel, (a,ii) Euclidean correspondence when the vertex lays in an ambiguous position (cell's edge) and (b) internal and external correspondences based on the distance from the normal to the surface (blue arrow) and the voxel's location (inside or outside the surface).

4.3 Single vertex correspondence identification algorithm

The input of the approach, indeed, consists of a 3D DICOM image volume and a 3D surface, resulting from the segmentation of the volume. Concluded the first step, regarding the construction of a data structure that allows navigating the volume through the surface, we aim at coloring the surface's vertices with the volume's grey values exploiting a mapping between the surface and the volume (Fig. 4.8). Thus, it is necessary to find the correspondences between the volume image and the segmented 3D surface. For the grey values mapping, three different criteria are defined, according to the method chosen to identify the correspondences between the surface vertices and the volume voxels.

The search is directed toward the image value on the surface or in the interior and exterior direction with respect to the surface. In this way, we look at the segmented structure as fully immersed in its original volume. To this end, the surface and the volume must be superimposed to find the vertex-voxel correspondence. Since the 3D surfaces are extracted from the MRIs, their reference systems must be coherent, simplifying the superimposition step (Fig. 4.9).

Since we want to map onto the surface the grey values that are immediately outside or inside the segmented surface, we have to decide how far from the surface we want to move and in which

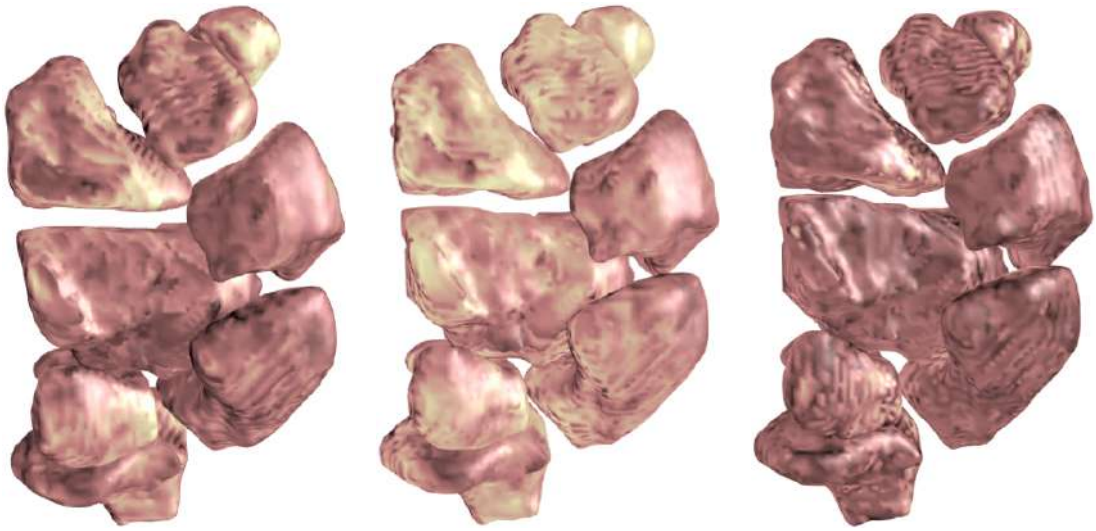

(a) (b) (c)

Figure 4.11: Surface mapping obtained with the vertex-voxel correspondence metrics: (a) Euclidean mapping, (b) internal mapping, (c) external mapping.

direction. We have explored several options, each providing a slightly different insight.

- *Euclidean mapping* if the surface vertex $\mathbf{p}$ gets the grey-level of the voxel $\mathbf{V}$ closest to $\mathbf{p}$ with respect to the Euclidean distance;
- *internal mapping* when the closest voxels are searched only inside the surface, that is, inside the object's volume;
- *external mapping* when the closest voxels are searched only outside the surface, that is, outside the object's volume.

For the Euclidean distance, given a surface vertex $\mathbf{p}$ the closest voxel $\mathbf{V}_i$ is defined as the centroid $\mathbf{c}_i$ such that $d(\mathbf{p}, \mathbf{c}_i) := min\|\mathbf{p} - \mathbf{c}_i\|_2$, for all voxels, that is, for all centroids c_i. Given the grid structure and considering the definition of Euclidean distance, the nearest centroid will be the one relative to the voxel containing the surface vertex. The volume is embedded in space through the grid, defined by 3D coordinates, thus, the best way to locate the voxel that contains a surface mesh vertex $\mathbf{p}$ is to navigate the grid structure. Since each voxel $\mathbf{V}(i, j, k)$ is identified by the $i - th, j - th, z - th$ intervals along the X, Y, and Z axis, we identify the voxel containing $\mathbf{p}$ by searching the intervals that contain the coordinates of the vertex $\mathbf{p}$. This situation applies when the vertex is strictly inside a single voxel (Fig. 4.10(a, i)). If the vertex lies on a grid node, a grid edge, or a grid element's face, then respectively, 8, 4, or 2 centroids will present the same minimum Euclidean distance from the considered vertex. In this implementation of

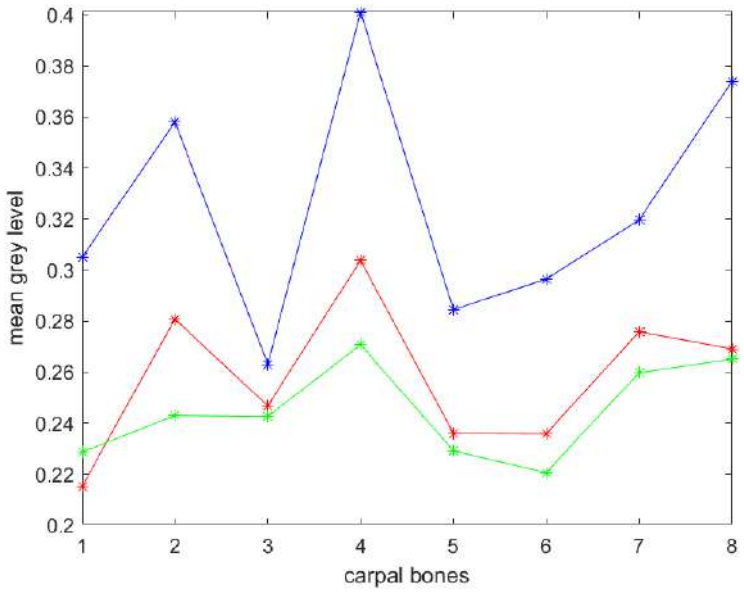

Figure 4.12: Mean grey-levels value graph for each bone (numbered from 1 to 8). Blue corresponds to internal mapping, red to Euclidean mapping, and green to external mapping. Blue values are higher since internal mapping explores the volume toward the bone marrow. External mapping is darker since the tissues outside the bone result in black or dark grey. Euclidean mapping, corresponding to the volume grey-levels in the surface location, lays in between the others.

the algorithm, all the centroids identified will be considered equally correspondent to the vertex (Fig. 4.10(a, ii)).

The other mappings applicable, as listed above, are based on the distance from the normal to the surface. These mapping methods can distinguish between the volume inside the surface and the volume outside it. To remain close to the surface, a small neighborhood of voxel surrounding each vertex is considered. Here, we compute the dot product between the surface normal at a vertex and the vector connecting the vertex to the centroid of a voxel. A positive dot-product indicates a voxel outside, while a negative one, a voxel inside the surface. Then, for all the vertices that belong to the neighborhood, the vertex-voxel distance is computed as: $d(p, c) = \|\mathbf{n} \wedge \mathbf{e}_{pc}\| \ / \ \|\mathbf{n}\|$, where $\mathbf{n}$ is the normal to the surface of the selected vertex and $\mathbf{e}_{pc}$ is the vector connecting the vertex to the grid centroid $\mathbf{e}_{pc} = \mathbf{p} - \mathbf{c}$. The centroid that presents minimum distance from the normal and lays inside the surface will be the correspondent one in terms of *internal mapping*. Whereas the centroid that presents the minimum distance from the normal, among the ones that are outside the surface, will be the correspondent one in terms of *external mapping*.

These correspondences have to be computed for all the vertices that constitute the bone surface. Thus, each vertex is considered separately and, once all the vertices are associated with the

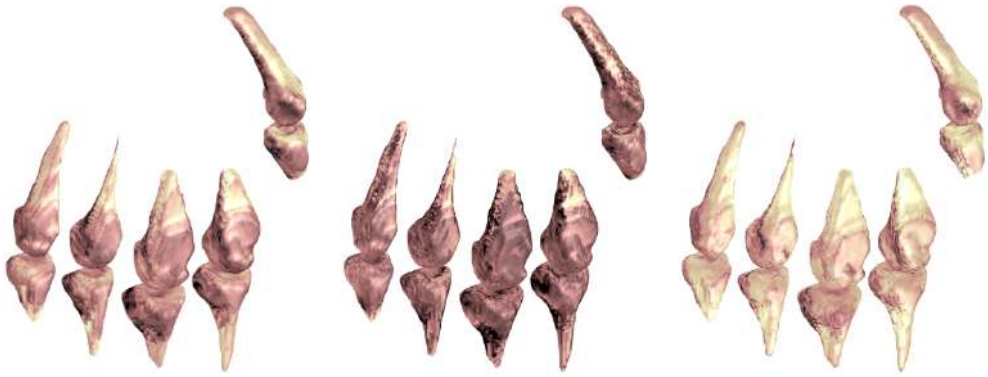

(a) (b) (c)

Figure 4.13: Application of the mapping algorithm to the hand district: (a) Euclidean mapping, (b) external mapping, and (c) internal mapping.

correspondent voxel, the texture mapping begins.

Computational costs During the search for vertex-voxel correspondence, it is easy to incur in a relevant growth of the computational cost. This is particularly evident for Euclidean correspondence since the other correspondences, based on the distance from the normal, are computed in a small neighborhood of centroids. The surface mesh is composed of k vertices and the volume grid dimension is $N = A \times B \times C$. The method used by the algorithm takes advantage of the data structure: identifying the nearest centroid as the one belonging to the voxel containing the vertex. In this case, the computational cost for a single vertex-voxel correspondence search will be $\mathcal{O}(\sqrt[3]{N})$, since the search is performed separately in each dimension of the grid. This method is the one applied since, with respect to a kd-tree ($\mathcal{O}(N \log N)$), permits to easily identify and deal with the ambiguous situations mentioned previously.

4.4 Texture mapping

At this point, every vertex of the surface is associated with a corresponding centroid and, thus with a corresponding voxel. Since the volume grid element is representative of a volume voxel, it contains information about the grey-level of that voxel. The grid volume element is identified by its index inside the volume. To perform the actual mapping, each vertex is associated with the same grey-level owned by the correspondent voxel which, in turn, is the grey-level of the centroid of the grid volume element. The only exception arises when, in the *Euclidean mapping* correspondence, the surface vertex belongs to one of the ambiguous position described previously. Since all the centroids that present minimum Euclidean distance from the vertex are considered as equally relevant, in these cases, a mean of the correspondent voxels' grey-levels is performed

and associated with the vertex.

Computer Graphics considerations The result of the grey-levels mapping is the addition of the color information to the triangulation structure: each vertex coordinate is associated with its specific color, representative of the information contained in the image. In particular, the *Euclidean mapping* is representative of the volume in the location of the 3D surface. For this reason, provides information on the structures that are crossed by the surface. The *internal* and *external mapping* explore the volume in the neighborhood of the surface, defining the internal or external normal directions from surface vertices. The information brought by these two methods are related to the volume composition inside and outside the surface, providing insights on the gradient variation of the grey-levels. The volume knowledge mapped on the surface exploiting the texture, provides an enhanced visualization method able to integrate heterogeneous data. Moreover, this integrated solution can be used as the starting point for different scopes such as shape analysis, shape segmentation, and object classification. The texture information can be easily integrated into those analyses with the awareness that now, such texture, represents a direct link to the real volume context.

The method applies also to different image resolutions, indeed, the 3D grid that bridges the volume field to the surface field can adapt the single grid element of the same size as the image voxel. This means that if a higher image resolution is provided as input then the result will be more accurate in reflecting, through the texture information, the anatomical structures surrounding the surface.

Mapping voxels' grey-levels into the mesh vertices permits the enhancement of the visualization through the 3D surface models. Other approaches for the representation of the surface exist and could be applied for the integration of volume image information on surfaces. However, the method described in 4.2 is more direct and permits to take full advantage of the 3D surface obtained by experts from the volume segmentations. Since the texture obtained by our method represent the real density of the volume, the added information can simply but effectively improve shape analysis techniques. A comprehensive 3D visualization is still a key component of medical analysis and Computer Graphics techniques can extract additional relevant details. In particular, evaluating the performed segmentation exploiting texture gradient values can provide a 3D description of the object in terms of the context in which it is inserted. 3D shape descriptors with the additional information provided by the texture allow the extraction of density characteristics from articular regions. This density information, in turn, enriches shape analysis and semantic segmentation. A shape comparison method based on distance definition can be improved by the computation of texture changes. Shape characterization via landmark identification can also take advantage of the mapped surface.

Clinical aspects considerations The proposed approach supports the integration of the surface shape model with the image volume grey-levels and provides to physicians and surgeons an augmented 3D representation of the bone surface. The combination of district density information and shape characteristics can overcome the limits of visualization methods that are based exclusively on volume processing. From a first analysis, the method performs as expected. The mapped bones result clearer if the direction of the search is addressed toward the interior of the bone, and darker when looking outside the bone. The Euclidean mapping result less smooth since it is relative to the edge between different tissue (Figs. 4.11, 4.12). These observable differences have a huge relevance since every type of mapping carries different information. Changing the mapping means exploring the volume in a different way and thus, retrieving different tissue information. For each possible clinical application is then important to choose the appropriate mapping method. This pipeline can be easily applied in other anatomical districts such as hip, shoulder, or ankle articulations. Indeed, the proposed method is general enough to be applied to other segmented data sets, such as the metacarpal and phalanx bones, independently from the method adopted to extract the surface model (Fig. 4.13).

Part II

Applications and Clinical Studies

Chapter 5

Clinical Applications of Grey-levels Mapping

5.1 Clinical aspects of early diagnosis in rehumatology

Rheumatic pathologies are numerous and present differences between one another thus, treatments, have to be tailored in order to provide the highest benefit for the specific patient. An early diagnosis and a proper differentiation of the pathology characteristics help the rheumatologist to select the right treatment from the very beginning. According to expert rheumatologists, the ligament insertion sites are regions that show clues on the type of rheumatic illness even in the early pathology onset and for this reason, their localization is a clinically relevant task. The identification of the ligament insertion must consider the anatomical structures involved (Section 5.1.1) and the key hypothesis on their role in the pathology discrimination (Section 5.1.2). Moreover, often, the first tissues to show slightly more advanced symptoms of the pathology are located in the articulation regions. The complex structure of the articulations that characterize the wrist makes it one of the most complex districts of the human body (Section 5.1.3).

Exploiting the mapping method described in Chapter 4 we propose a ligament insertions localization method based on the analysis of the 3D surface texture (Section 5.2).

The study of the wrist complicated anatomical structure can benefit from both shape descriptors and texture analysis. Thus, we propose an integration of the information retrievable from both aspects, aimed at the characterization of articulation regions, discussing the results obtained (Section 5.3).

In an advanced stage of the pathology, usually, early symptoms degenerate in the erosion of bone tissue which, in turn, is a key index of the evolution of the pathology (Section 5.4).

	Composition	Significance
Zone 1 ***Pure Dense Fibrous Connective Tissue***	Fibroblasts Type I Collagen Type III Collagen	Linearly arranged collagen with mechanical properties similar to mid-substance tendon
Zone 2 ***Uncalcified Fibrocartilage***	Fibrochondrocytes Proteoglycan aggrecan with Collagen (Types I-III)	Dissipates bending of collagen fibers in tendon
Tidemark		Basophilic demarcation between uncalcified and calcified fibrocartilage representing the boundary between soft and hard tissues
Zone 3 ***Calcified Fibrocartilage***	Fibrochondrocytes Type II Collagen (Predominant) Type I Collagen Type X Collagen	Irregularity of attachments into bone give mechanical integrity of enthesis
Zone 4 ***Bone***	Osteocytes Osteoblasts Osteoclasts Type I Collagen	Provides sites of attachment for the tendon

Figure 5.1: [ADD+14] Tissue composition of fibrocartilaginous different zones.

Erosion sites identification can base either on image information or morphological information (Section 5.5). However we propose an integrated method able to consider both aspects (Section 5.6).

5.1.1 Ligament insertions

The musculoskeletal system is structured in order to provide support and stability to the human body and makes possible the organized set of human movements. Overall, this system consists of bones, muscles, cartilages, tendons, ligaments, and other connective tissues that together form the functional organ system [ADD+14]. Thinking in engineering terms, tendons and ligaments can be associated with machines with multiple moving parts (e.g., fibrils, fibers, and fascicles), which performs a force transfer to and from the skeleton. Indeed, ligaments and tendons are involved in load distribution to perform movement patterns [BTR+06]. In particular, tendons and ligaments, constituted by connective tissues, join the bone in specialized interfaces that form the *insertion sites*, which formally are known as *enthesis*. Here, tendons/ligaments (TL), integrate their structure with the one of the bone to facilitate joint motion [ADD+14]. Indeed, the insertion sites help to transmit the tensile load from soft tissues to the bone, thus allowing the proper transmission of contractile forces from the muscle belly to the respective skeletal attachment, while simultaneously dissipating force away from the enthesis itself [ADD+14].

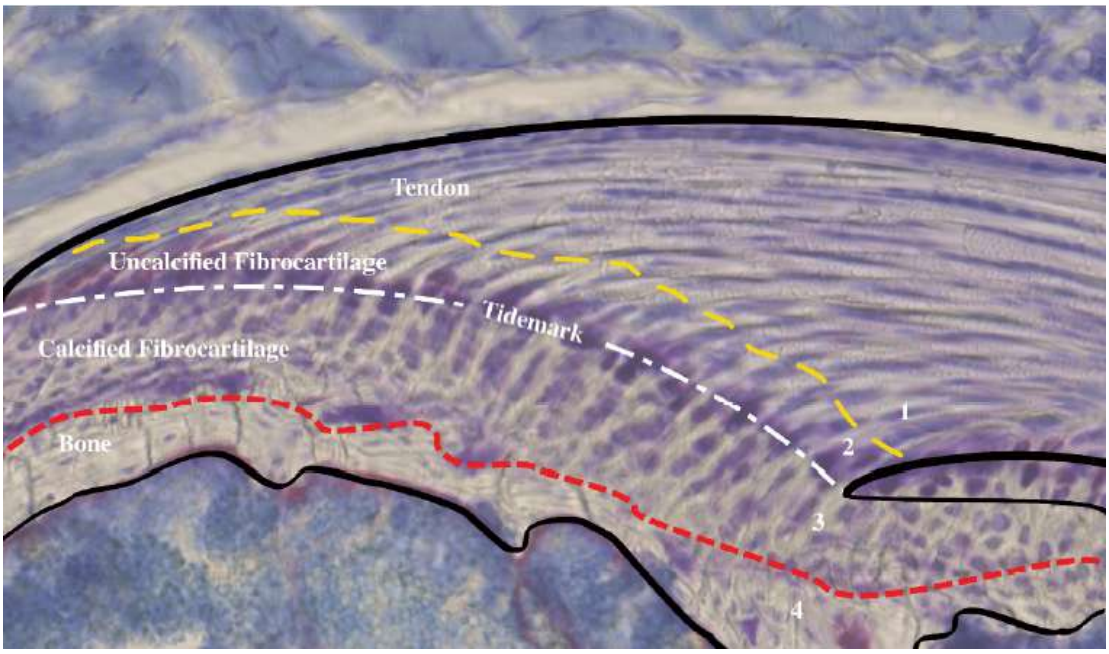

Figure 5.2: [ADD+14] The four zones of the enthesis on an histological section of a mouse supraspinatus.

Overall, the role of the enthesis is triple:

1. anchorage of soft tissues to bone;
2. stress dissipation;
3. promotion of bone growth.

The enthesis can be described on the basis of the tissues they involve. In particular there are two main classes of entheses: *fibrous* and *fibrocartilaginous*. The majority of the human body entheses are fibrocartilaginous which, other than being more commonly studied, are also more frequently injured than fibrous insertions [ADD+14]. Fibocartilaginous entheses are found in the apophyses and epiphyses of long bones, on the short bones of the hands and feet, and are common also in the spine. Fibrous enthesis, instead, are typical of TL that attach to metaphyses and diaphyses of long bones [BM01].

Fibrous enthesis This type of insertion is characterized by dense fibrous connective tissue and is typically present in large surface areas where they pierce mineralized collagen fibers. They can be classified as *bony* if the TL inserts directly in the bone, or *periosteal* if the TL connects to the periosteum. This type of enthesis has received less attention than the fibrocartilaginous

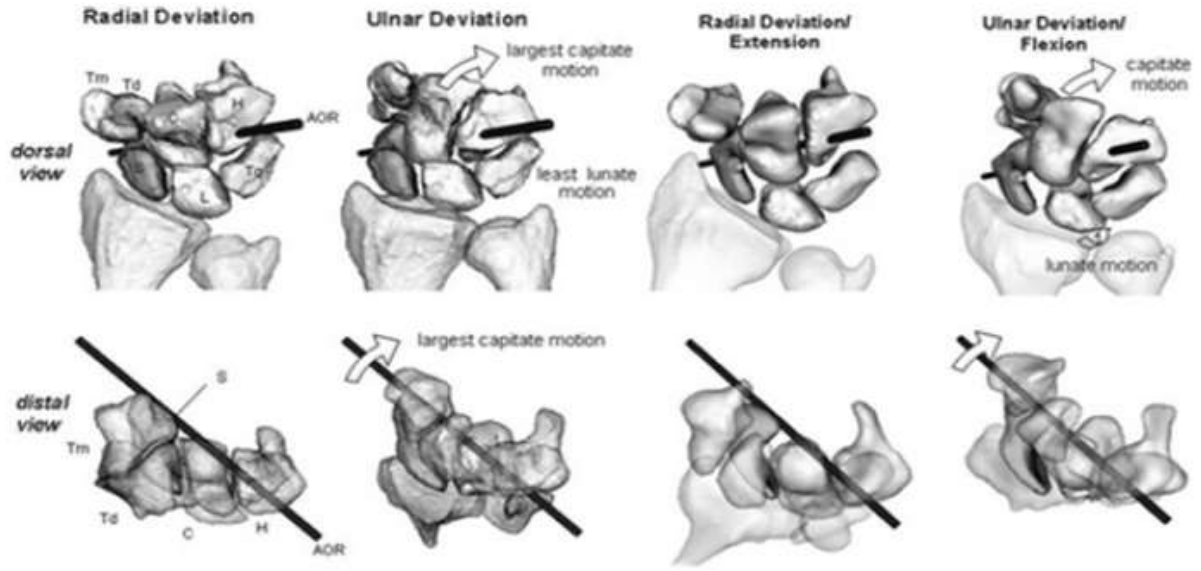

Figure 5.3: Carpal bones relations in wrist movements.

one since it is less common in the human body and never presented a high rate of injury cases [ADD+14].

Fibrocartilaginous enthesis As the name suggests, Fibrocartilaginous entheses, are characterized by fibrocartilage, they are more common in the human body and present a higher tendency to be injured for overuse. This kind of insertion is particularly interesting for our work since it is the most present in the carpal district. Typically, this enthesis can be divided into four distinct zones creating a structurally continuous gradient that goes from uncalcified tendon to calcified bone. Fig. 5.1 presents the fibrocartilaginous enthesis with the relative tissue composition, and Fig. 5.2 shows a typical fibrocartilaginous insertion.

For the purposes of this work, it is important to consider also the bone side of the attachment. Indeed, in the TL insertion area, the bone is constituted by fibrous tissue. This kind of bone tissue is the first to be deposited both during growth and bone fracture healing, but then it is substituted by lamellar bony tissue. The only region that continues to present the fibrous tissue is, indeed, the insertion site. In this kind of tissue, the collagen fibers present relevant dimensions and are distributed without a particularly defined orientation.

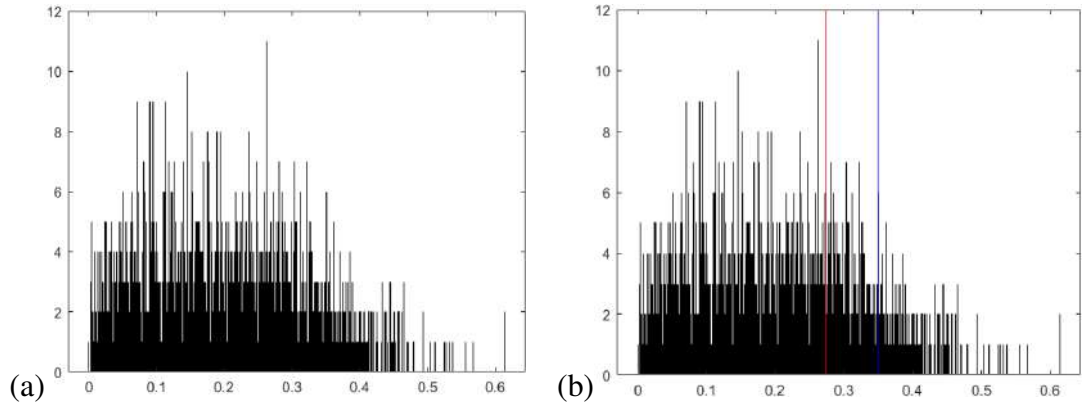

Figure 5.4: (a) Histogram of the grey-levels mapped on the surface vertex. (b) Thresholds identifying the grey-level range associated with ligaments insertion: 75th percentile (red), and maximum of brightness allowed to remain in the dark gray region (blue).

5.1.2 Enthesis localization in the case-study

The carpal district constitutes a challenge even in the description of the TL enthesis localization. Indeed, the presence of a high number of small bones requires also the cooperation of a high number of tendons and ligaments for both stabilization and movement control. However, rheumatologists confirm the importance of the identification of those insertions for diagnostic purposes. Even if the enthesis is commonly understood as the junction between a TL or a joint capsule to the bone, there are good reasons to support the idea that entheses can present complex anatomy, described through the analysis of the TL-bone junction itself. The reason for that is due to the possible presence of adjacent tissue specializations in both the TL and the bone that are functionally related. From this analysis, the concept of *enthesis organ* has been proposed [BM01]. This concept is extremely important for clinicians, especially rheumatologists since it can help to explain and differentiate patterns of injury or even explain why the symptoms associated with a particular enthesopathy are diffuse [BTR$^+$06].

The term *enthesopathy* refers to the involvement of the entheses in any pathological process, such as inflammatory, metabolic, traumatic, or degenerative. Indeed enthesopathy has been well recognized as a feature of a variety of systemic rheumatic disorders [SRB$^+$15].

In spondyloarthropathies, enthesitis can be considered a significant clinical manifestation and important to pathogenesis; in particular, enthesitis helps the diagnosis of Psoriatic Arthropathy or juvenile enthesitis-related arthritis [SR17]. According to the study proposed by [KEA$^+$18], $35-50\%$ of patients with PsA reported the presence of enthesitis and enthesitis presented in PsA more than in other forms of arthritis such as Rheumatoid Arthritis, Ankylosing Spondylitis (AS), and Osteoarthritis. Furthermore, entheses may be the main target of the disease process in many prevalent rheumatic conditions.

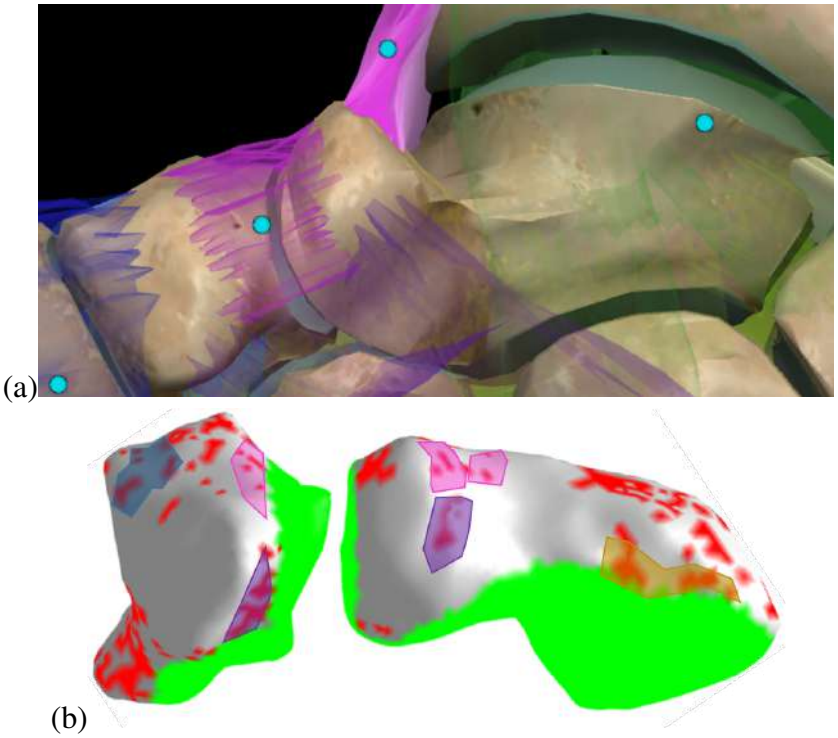

Figure 5.5: (a) Anatomical atlas of the ligament insertion sites on the trapezium and scaphoid bones of a healthy subject. (b) Result of our analysis on a 3D segmented bone: red regions represent ligament insertion sites estimation, green areas highlight articulation regions.

Given these premises, it is evident that the study of enthesitis is fundamental for pathology differentiation and analysis of the disease's gravity. One of the difficulties in the evaluation of enthesitis is their localization. Since the enthesis is located very close to the synovium its location uncertainty often makes clinical diagnosis problematic [KEA+18]. However, through the use of imaging techniques such as MRI, the localization of the insertion sites and thus, the evaluation of enthesitis, can be improved.

5.1.3 Articulation regions

The different bones that compose the carpus allow variable movement of the wrist and, consequently of the hand. This aspect implies the presence of different surface areas involved in the articulations. Fig 5.3 gives an idea of the structures involved in some of the possible movements performed by the carpal district. The study of the kinematics of a healthy, as well as a pathological, district is relevant in clinical practice and it benefits from knowledge about functional subparts of the individual bone. Ligament insertion sites positioning (Section 5.1.2), and area of articulation regions are examples of such relevant subparts.

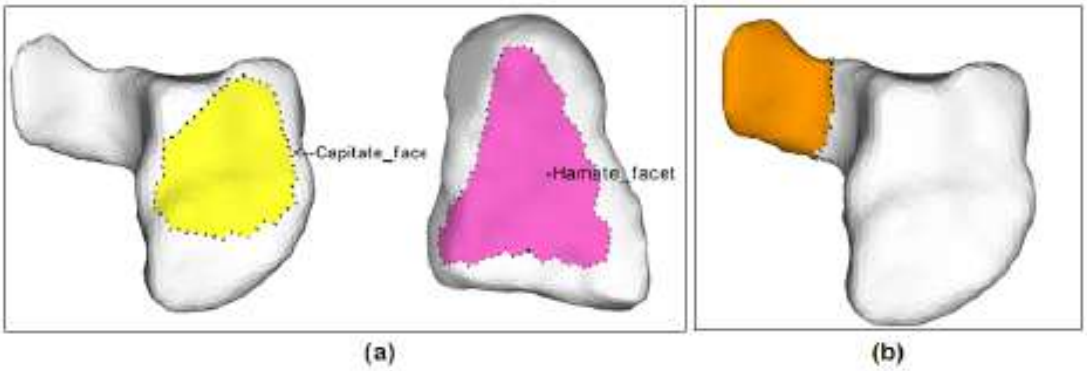

Figure 5.6: Anatomical landmarks on carpal bones: (a) articulation facets between hamate (yellow) and capitate (pink); (b) hook of hamate, prominent bony feature (orange).

To have a complete idea of the functional subpart status and organization, it is necessary to analyze not only every single bone but also the complete carpus setting since the location of functional regions is highly dependent on the inter-carpal spatial arrangement. The identification of the functional sub-parts through the visualization of 2D images is a common practice in the medical field. Some computer-guided studies have been performed to imitate the same process made by physicians through the analysis of anatomical shapes, considering the 2D perspective of scan images. However, the presence of a projection in 2D of anatomical structure can cause gaps due to occlusions. Especially for the carpal bones, where different shapes and variable orientations and overlaps are involved. Indeed, more views are needed to analyze and comprehend the bone structures.

Thanks to Computer Graphics development, Patient-specific 3D anatomical models (3D-PSMs) have been widely spread and applied in clinical research. 3D PSMs are 3D computational reconstructions of a patient's anatomy, which mirror the accurate appearance of the patients' organs in the 3D space. The 3D-PSMs are expected to be extremely useful in many applications such as biomechanical simulation, Computer-assisted Diagnosis and Surgery, prosthesis fitting, and legal medicine. In the last decade, a lot of geometric techniques for 3D shape analysis have been developed [ABM+06] and also applied to 3D PSMs. However, traditional geometric descriptors are not enough to identify the high-level functional features since:

- the anatomical features often belong to regions that do not have a strong geometric characterization, i.e., the markers of functional landmarks (articulation areas) are usually featureless flat regions;
- the definition of these features is intrinsically vague; indeed, features cannot be coded or identified by any mathematical formulation;
- landmarks are highly variable among individuals;

- shape alteration makes the anatomical shape characterization more challenging, due to the presence of pathological conditions.

These facts suggest that the analysis of the shape of bones should be coupled, with the co-analysis of all the elements of a district with the aim of identifying interoperability properties that model the articulation functionality. A study by [BPF+19] proposed a research in this direction, developing a characterization that considers also the functional interdependencies, which are particularly relevant in complex districts such as the wrist.

5.2 Ligament insertion localization with texture analysis

In the diagnosis of rheumatoid diseases, the ligaments' insertion sites are relevant areas for physicians as they help to classify the underlying pathology at its early stages and to start a patient-specific therapy. A visualization instrument able to identify the location of those insertion areas is particularly useful to support physicians in the early diagnosis of different pathologies of the carpal districts. The proposed approach takes advantage of the grey-levels mapping result (Chapter 4), in order to focus on both the MRI information and the 3D visualization of the enthesis locations. The identification of ligament insertion sites is indeed performed on the mapped surfaces but basing on the grey-levels since ligament insertions are not related to any particular morphology characteristics. However, the possibility to exploit the surface information during the grey-levels mapping phase helps in focusing the research on the image region that can actually present the insertion site, without the need of analyzing the entire volume.

To identify the insertions on the surface by the mapping result, the range of grey-levels characterizing the different tissues have to be analyzed. Indeed, given the tissue composition of the enthesis region (Section 5.1.1), and considering that the images are low-field, it is plausible to identify an approximative range of grey-levels that could represent the insertion site. In a T1 weighted MRI, the tissues outside the bone marrow are represented as black or dark grey voxels. The original MRIs are 12-bit images with 4096 grey-levels, normalized between 0 and 1. Focusing on the histogram of one bone mapping and excluding the black vertices (which are the majority), more than half of the remaining vertices are characterized by grey-levels between 0 and 0.3, with variations that depend on the single bone (Fig. 5.4 (a)).

To find the proper range of grey-levels that characterize the ligament insertions, some considerations must be made. In correspondence to those regions, the composition of the bone tissue changes with respect to the regions where ligaments are not involved. Indeed, the cortical bone, in the presence of ligaments, is characterized by fibrous bone tissues, while lamellar bone tissue is predominant in the rest of the bone. For those reasons, the grey-level of ligament insertions should belong to the brighter range among the dark grey-levels. To automatize the process and customize it for each patient, we base our subdivision on the histogram of each bone. Given the

histogram, we calculated the 75th percentile and considered it as the threshold: above the value are the grey-levels indicating a ligament insertion, below the value, all other tissues. Moreover, we add a second roof threshold placed at value 0.35 to remain in the area of dark grey-levels (Fig. 5.4 (b)).

Ligament insertion sites localization results Good results have been obtained in the preliminary study developed. In Fig. 5.5(a), the ligaments insertion regions according to anatomical atlases [sit20] are coherent to those identified by our method (Fig. 5.5(b)). In this case, the real subject is taken from the healthy cluster present in the data set. Since the volumes are low-field MR images, the regions are not accurately defined. Nevertheless, physicians need to approximately identify the region where they can find the ligaments insertions to the bones considering the specific patient.

5.3 Articulation region characterization

Characterizing a shape means building a computational description able to preserve the most representative elements of the shape, usually a few basic types, along with their relationships and their invariants [FS98]. In this context, mathematics plays a key role to handle the complexity of digital shapes, in particular, differential topology provides a setting able to formalize several problems related to shape analysis and description. In this scenario, methods have been derived to analyze the shape of an object according to the properties of real functions defined on it. The added value of these approaches is that different functions can be used according to the properties and invariants that one aims to capture, thus providing a flexible shape description framework. Examples of popular functions used in object analysis and matching are distance functions, curvature-based and geodesic-based functions, Laplace eigenfunctions and distribution maps [BDF$^+$08, BFF$^+$07]. Then, the geometric/topological information related to the shape is compactly stored into descriptors [BCA$^+$16], for instance, adopting feature vectors [BKS$^+$05], graph-based descriptions (e.g. Reeb graphs [BGSF08]), or maps [HWG14].

Unfortunately, given a collection of 3D models, a single property is not likely to provide a good organization of the data, or at least it could be not informative enough [HZG$^+$12]. To address this limitation, a recent path of research aims to derive high-level information by analyzing single objects in the context of larger *collections* of models: the idea is to derive information not only from the object itself but also from its relation with the other ones in the collection [HWG14]. This is the case, for example, of the *co-segmentation* of a set of 3D objects, [WAvK$^+$12, HFL12, KHS10], i.e. the segmentation of the objects as a whole into consistent semantic parts with part correspondences.

These 3D shape analysis techniques are meant to derive *semantic* (high-level) information from low-level properties exploring their relation with the other objects in the collection [OLGM11,

Table 5.1: Bone-based properties: a list of state-of-the-art methods.

Characterisation of a single bone	
Distance-based	
Distance from the centre-of-mass (CM)	Spatial distribution of the object with respect to its centre of mass (barycentre).
Distance from a principal axis (LD) [BB13]	Spatial distribution of the object with respect to its main axis.
Distance from a principal plane (PD) [BB13]	Surface symmetry with respect to the plane through the bary-centre and with the principal axis as its normal vector.
Distance from the convex-hull (CV)	Punctual distance between the shape vertices and the object convex-hull (crumpliness [CRC+02]).
Geodesic distance from random surface samples (GD) [HSKK01]	Average geodesic distance where the source points are randomly distributed.
Geodesic distance with the farthest point sampling (GD_FD) [MD03]	Average geodesic distance where the source points are distributed sampling algorithm.
Curvature-based	
Gaussian Curvature (GC) [PS06]	Product of the principal curvatures.
Mean Curvature (MC) [PS06]	Half the sum of the principal curvatures.
Shape Index (SI) [KvD92]	Ratio between Gaussian and Mean curvatures.
Spectral-based	
3rd, 4th, 6th and 7th Eigen vectors [PP93]	3rd,4th, 6th and 7th Eigen vectors computed from the Eigen decomposition of Laplace-Beltrami operator.

HZG+12, KLM+12, ROA+13]. The goal is to facilitate exploration and content search as well as to understand their overall categorization and summarize their content [LMS13]. Here, *semantics* refers to the meaning, or *functionality*, of an object in a given context. The key challenge is that shapes can vary in different ways, and users may be interested in different types of variations [KLM+12, KLM+13]. Examples of applications are: *semantic annotation*, which is the automatic or semi-automatic labeling of objects (or parts of objects) [BAC+16]; *attribute transfer* techniques, which study how to automatically transfer labels from a single object (or part of an object) to sets of unknown objects [KBB+13]; the structuring of 3D large data sets to enable navigation and retrieval, which is often achieved by exploiting also the pairwise similarities between the rest of the data set models [HSS+13]. In all these approaches, a major issue is how to interpret such implicit knowledge. In general, the use of prior knowledge might be inevitable; anyway, the recent advances in learning techniques have achieved state-of-the-art performance in Computer Vision applications [CMS12]. These techniques represent a possible solution to determine automatically the weights of the different shape features on the basis of context (e.g., the shape classes of a database) [BB13, TDVC13], design class-specific or application-specific shape descriptors [BMM+15] or extend deep learning techniques to geometry [MRB+16, BBL+17].

Shape characterization methods can be applied also on 3D surfaces representing anatomical structures, like the ones considered in this Thesis (Section 5.3.1). Starting from feature-based characterization we propose an integration with tissue information retrievable from the grey-levels mapping results (Section 5.3.2).

5.3.1 Feature-based carpal characterization

By discussing with the domain experts, we derived that the most relevant anatomical landmarks of carpal bones in the context of Musculoskeletal Diseases (MSD) diagnosis and treatment are: *articulation facet* - zone of the bone that participates in articulation, *contact area* - zone of the bone that is adjacent with the neighboring bones within the district, and *prominent bony feature* - zone of the bone that exhibits typical morphological characteristics (e.g., protrusions, concavi-

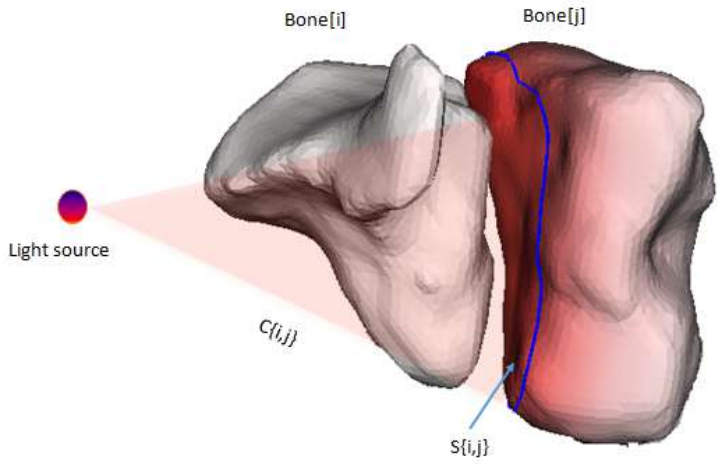

Figure 5.7: The shadow map descriptor represents the shadow projected from a bone on its adjacent one. The directional light source is opposite to the normal of the surface on which the shadow is drawn.

ties). Among these anatomical landmarks, frequently, the articulation facets and contact areas of the carpal bones belong to a relatively flat region, while prominent bony features have peculiar morphological characteristics that are geometrically well characterized. We present the example of hamate and capitate bones in Fig. 5.6, where the articulation facets belong to geometric featureless regions and therefore are not well characterized via morphological properties, while the protruded bony feature - hook of hamate, can be easily described by geometric functions (e.g. distance from the center of mass). For this reason, the analysis of the single bones with standard geometric properties is relevant as the analysis of the articulation district as a whole. Indeed, state-of-the-art methods for shape analysis can be applied also to 3D PSMs of the interested bones, thus this group of properties can also be named *bone-based*, since they are computed by considering only the shape of an individual 3D bone model.

Table 5.1 lists the state-of-the-art properties that revealed to be particularly useful for the case-study, since they can complement each other in terms of their sensitivity to feature types, and as a result, can derive high-level information. Purely geometric properties are relevant for characterizing prominent bone features that are morphologically well-characterized. However, these geometric characterization techniques are not fully suitable to identify the functional features of carpal bones that often belong to the geometric featureless and/or flat regions. The properties that are able to characterize the functional parts (articulation and contact areas) of the patient-specific 3D models, can be called *district-based* properties. These measures integrate the whole district perspective with the individual shapes of the bones. The semantics behind the articulation and adjacency relations between the carpal bones has been modeled in the *Carpus ontology* [BAC+16] which is specifically designed to support computational analysis of patient-specific 3D carpal bones. This formalism represents the anatomical information in a form that is

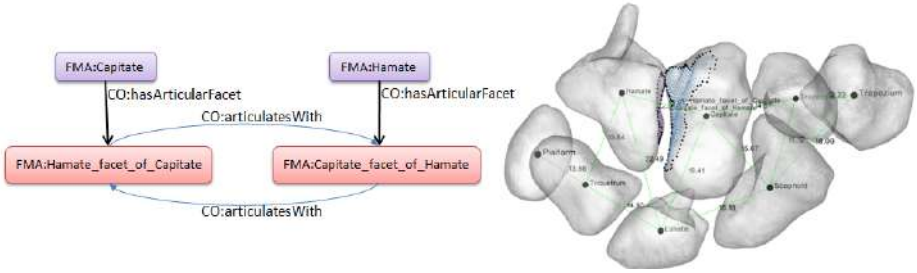

Figure 5.8: Conceptualisation of the `articulatesWith` relation in the Carpus Ontology on the left, Corresponding visualisation on the 3D model on the right.

able to support reasoning, inference, and assertion. Particularly, when such knowledge is associated directly with the patient 3D data, it allows for dynamic navigation of the 3D geometry, with the possibility to extend the reasoning to the geometric aspects.

Algorithm 1 `Shadow map` computation

procedure SHADOW MAP COMPUTATION (BONES[8])
  Input: *Bones[8]* $\leftarrow$ 8 carpal bone triangulations (.off)
  R[8][8] $\leftarrow$ Articulation Matrix
  Output:*ShadowMap[8]* $\leftarrow$ array of scalar values
  for $<i = 1$ `to` $8>$ **do**
    for $<j = 1$ `to` $8>$ **do**
      if $(i! = j$ `and` $R[i][j] = 1)$ **then**
        $Shadow[i] \leftarrow$ ***PROJECTION(Bone[i], Bone[j])***
  $DrawContour(Shadow[i])$ ▷ contour based on the pre-defined range
procedure COMPUTESHADOW($Model_1$, $Model_2$)
  $KDTree \leftarrow$ ***BuildKDTree(***$Model_2$***)***
  for `each` $vertex_k$ `of` $Model_1$ **do**
    $CloseP \leftarrow FindClosestPoint(vertex_k, KDTree)$
    $SquareDis \leftarrow EuclideanDistance(vertex_k, CloseP)$
    if $SquareDis < Shadow[i][k]$ **then**
      $Shadow[Model_1][k] \leftarrow SquareDis$

Shadow map: Is one of the *district-based* properties able to describe wrist articulations. It is a scalar function that characterizes the articulation areas of the carpal bones following the intuition that the articulation regions are the areas of the bones which *face to each other*, and these areas can be defined as the *shadow* cast by each bone onto the adjacent ones (see Fig.5.7). The shadow map represents this information, capturing not only information on the shape of the individual bones but also about their spatial arrangement in the whole district. The input is constituted by the eight 3D carpal bone models in the same coordinate system $Bone[8] = \{B_1, B_2, ...B_8\}$ and

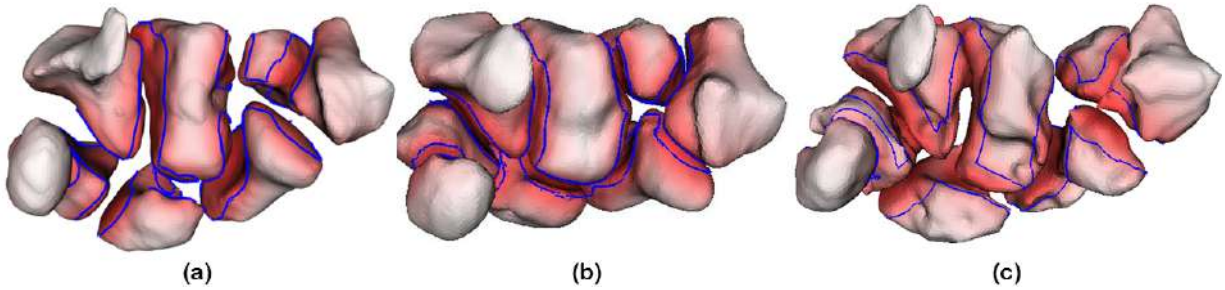

Figure 5.9: The computation of the Shadow map applied on: (a) models segmented from MRI images; (b) models segmented from CT images; (c) a pathological case affected by Rheumatoid Arthritis stage 3 (pinker areas indicates higher values of the shadow map).

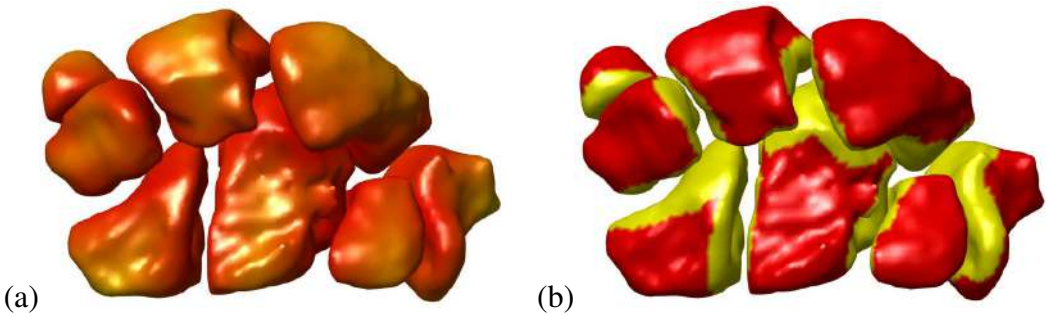

Figure 5.10: (a) Shadow map on the wrist district, (b) shadow map analysis result: distinction between bone regions identified as articular facets (yellow) and regions free from articulation interaction (red).

.

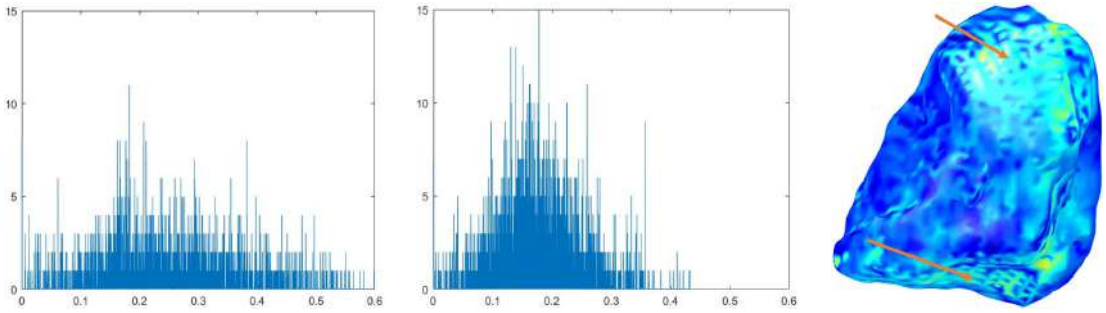

(a) (b) (c)

Figure 5.11: (a) Histogram of grey-levels in the capitate bone articulation facets, (b) grey-levels histogram related to zones not involved in any articulation, (c) external mapping of the capitate bone: in the articulation facets, (orange arrows) it results brighter.

the articulation matrix $R[8][8]$, which is defined by the Carpus Ontology as $R[i][j] = 1$ when $Bone[i]$ `articulatesWith` $Bone[j]$ (Fig.5.8), and $R[i][j] = 0$ otherwise. To compute the Shadow map we adopt the concept of orthographic projection where the shadow is projected by a point light source and the directional light source directed opposite to the normal of the surface on which the shadow is drawn. The main idea is the following: we take the $Bone[i]$, and then project its approximate shadow $S_{i,j}$ on another bone surface $Bone[j]$ which is defined by a generalised cone $C_{i,j} \subset R^3$ that marks the maximum region of space compatible with $Bone[j]$ and $Bone[i]$. Note that the shadow of $Bone[i]$ is projected onto $Bone[j]$ only if $R[i][j] = 1$. Following this approach, we compute the $ShadowMap[8]$ vector, which describes the shadows projected onto all the eight carpal bones. Algorithm 1 presents the pseudo-code to compute the *Shadow Map* from the carpal bones.

We present results of the *Shadow map* computation in Fig. 5.9 (healthy and pathological data set), where the bone surfaces are colored according to the triangle-wise scalar value of the *ShadowMap* function and the contours are drawn based on a predefined scalar value range. In Fig. 5.9, we also represent the shadow map computation on a pathological data set (RA stage 3) where, regardless of the fact that the bone surfaces are mostly eroded, the descriptor provides an acceptable characterization by coupling the bone geometry with the spatial arrangement. However, the Shadow map fails to produce a reasonable characterization solely when the spatial arrangement of the district is significantly altered due to some typical pathological conditions, e.g. advanced carpal collapse, missing bone, complex fracture.

5.3.2 Integration of shape and grey-levels analysis results

The shadow map descriptor can be easily integrated with the grey-level mapping method (Chapter 4). The idea is to provide a more complete characterization of the district, describing not

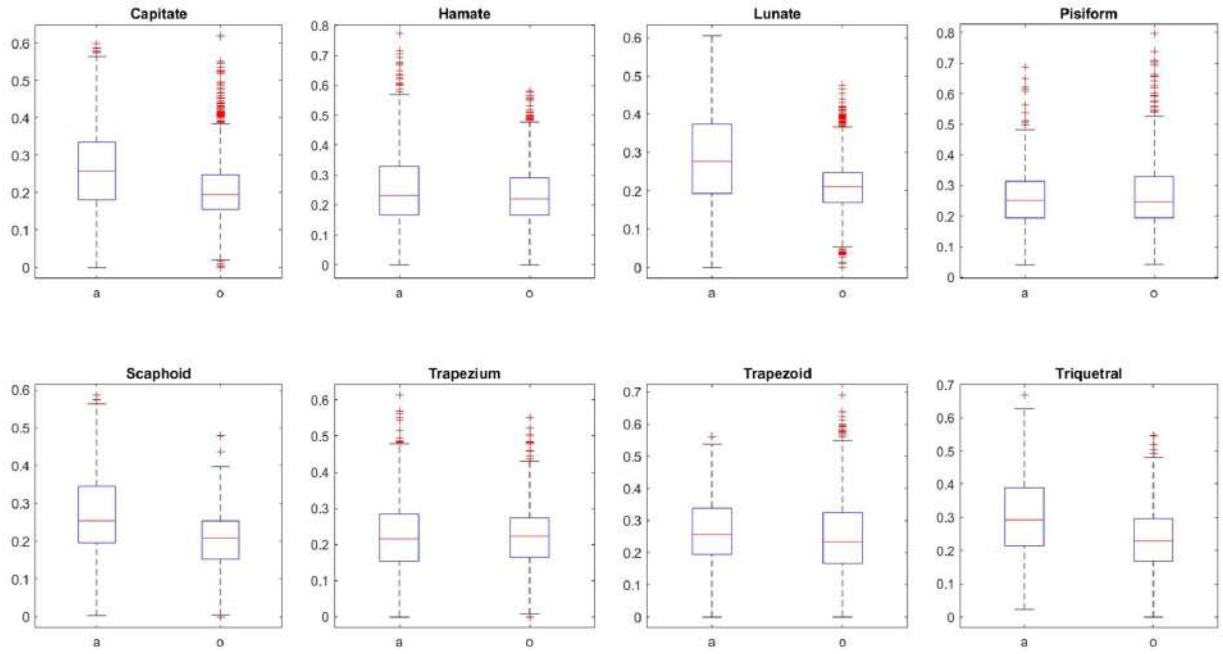

Figure 5.12: Boxplot of the grey-levels distributions for each bone in articulation areas (a) compared to the distributions of the non-articulation areas (o). The articulation areas show a wider range and often higher median value. The distribution of the articulation regions results significantly different from the non-articular region distribution except for pisiform and trapezium bones.

only shape features but also the relative volume information. Indeed, our textured surfaces of bones integrate this descriptor with the information of the tissue surrounding the bone surface. This integration is particularly indicated for areas, such as the articulation zones, which are often affected by early symptoms of a rheumatic pathology. The shape information of the articulation areas are indicated by the shadow map on the 3D PSM (Fig. 5.10)) and volume grey-levels are depicted from the mapped surface. In this case, since the relevant areas analyzed are intuitively outside the bone, the best result to integrate tissue information will be given by an analysis of the *external mapping*. Furthermore, we can compare the *external mapping* results in those regions with respect to the results in non-articulating areas.

It results that the mapping method is able to discriminate the articulation facets, not only by shape analysis (shadow map descriptor computation) but highlights those regions also with changes in the mapped color. In the articulation facets (Fig. 5.11(c)), the *external mapping* result brighter than in other regions, due to the tissues that compose this kind of joints. This is not just a visual response: the grey-levels histograms of the articulation facet is embracing a wider range of brighter grey-levels in comparison with the histogram of other regions of the

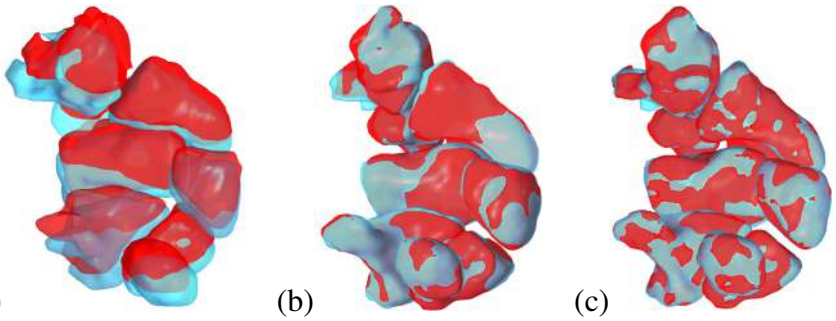

(a) (b) (c)

Figure 5.13: Registration process result. (a) Original situation, (b) after centroid translation, (c) final result obtained with ICP.

same bone (Fig. 5.11(a,b)). These considerations are confirmed by the analysis of the whole district. Fig. 5.12 shows the distribution of the grey-levels through boxplots. For each bone, the left boxplot (a) represents the distribution in correspondence of articulation facets, while the right boxplot (o) shows the distribution outside the articulation regions. A one-way ANOVA test has been performed on each bone to demonstrate the statistically significant difference between articulation and non-articulation regions. All the bones present an articulation region grey-level distribution significantly different from the non-articulation one, except for the Pisiform and the Trapezium case. However, the Trapezium presents a wider range, as expected, in the articulation grey-level distribution. The Pisiform bone, instead, can easily result as an outlier since it is the smallest bone of the district and presents just one articulation site. Indeed, considering the overall district, the articulation areas actually present a different grey-level distribution with respect to the non-articulation regions.

5.4 Clinical aspects of rheumatic pathologies monitoring

In Rheumatology, as well as in most medical branches, follow-up exams are commonly used to analyze degenerative diseases. These exams consist of the control of the patient's status over time. The importance of follow-up analysis resides in their support to the study of the pathology development which, in turn, brings to personalized adjustments of the therapy. Different degenerative pathologies, in the rheumatological domain, bring to a deformation of the bones, usually linked to an erosion process. The origin of such erosive degeneration differs according to the particular undergoing pathology, but the result is an anomalous change in the tissues' composition and, as a consequence, in the bone morphology. Patients that present a similar situation suffer from severe pain and difficulties in the mobility of the interested joints, as a consequence of the damaged bones relations. Since an erosion can deform the shape of a bone, an effective strategy is to scan and analyze the anatomical district in order to identify morphological changes in 3D surface models, focusing the analysis on geometric anomalies with respect to the normal case.

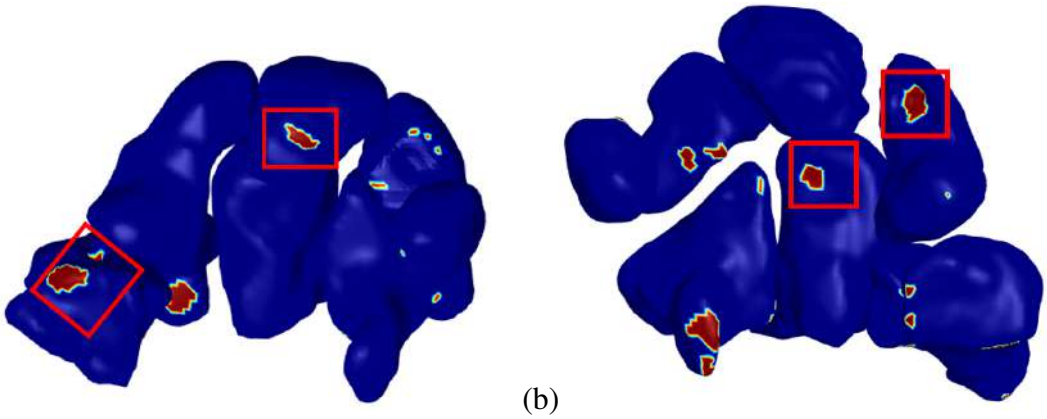

(a) (b)

Figure 5.14: Erosion localization (on two different subjects) based on the geometric analysis through distance distribution thresholding. Blue regions indicate healthy bones and red regions locate potential erosions. The red rectangles indicate erosions identified by experts.

Morphological changes in degenerative diseases are usually related to a previous degeneration of tissues. This means that the composition of the structures around the bone and in the bones themselves mutate, and such degeneration can be detected in the input images. Thus, the identification and evaluation of erosion regions have been studied in literature through the use of fo shape analysis (Section 5.4.2) and image processing (Section 5.4.1). We propose a comparison between two approaches (Section 5.5) calling the first *geometry-based* and the second *texture-based*. The *geometry-based* approach is based on the geometric differences on the 3D segmented surfaces, without considering tissue information. The *texture-based* approach identifies degenerations in the tissue composition through an analysis of the changes in grey-levels. Moreover, to provide higher accuracy, we propose an integration method that exploits both the information retrieved from the shape analysis and from the texture (Section 5.6).

5.4.1 Image-based erosion identification methods

Medical images constitute the basic instrument and the starting point to perform radiography analysis, which, in turn, are at the core of monitoring and diagnosing rheumatic diseases. Bone erosion represents a well-established indicator of such diseases. Nowadays, two of the most frequently used imaging techniques for the study of rheumatic diseases are Computed Tomography (CT) and Magnetic Resonance (MRI). It has been found that, for erosion detection, the MRI exam provides a higher sensitivity with respect to CT [DEH$^+$08]. A study regarding 7 years follow-up analysis compares three different imaging techniques in their capacity to identify bone erosion and synovitis [SHO$^+$06]. Another work presented a similar comparison but in a smaller period of time [BBS$^+$02]. This study regards a 2 years follow-up in presence of a specific therapy and compares two imaging methods in the ability to highlight erosion sites. However, in all these

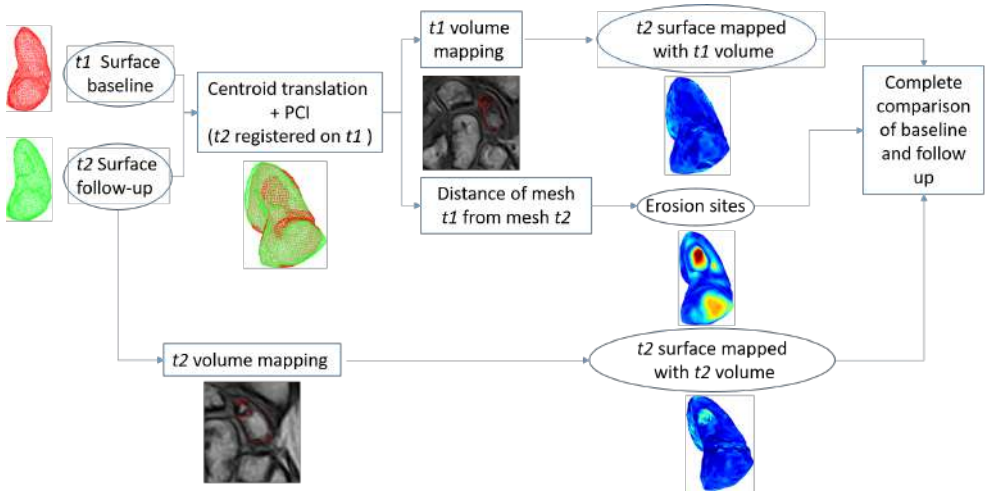

Figure 5.15: Workflow of the analysis of the same patient over time.

studies the identification of critical sites, such as erosion or synovitis, was performed by experts. This kind of manual identification is error-prone and time-consuming, especially with 3D images. Furthermore, the identification performed by experts is influenced by their previous knowledge and expertise. For the aforementioned reasons, the study of automatic or semi-automatic identification of erosion sites in images has been widely studied in recent years. Indeed, the analysis and quantification of image features through processing techniques are largely used in the study of rheumatic diseases, [HVvdH+15], [LPBK08]. Previous work exploits the use of active shape models and snakes to individuate the erosion site [GPM16, LHS+06]. Moreover, a comparison [FKS+18] of automatic, semi-automatic, and manual methods in the estimation of bone erosion from images has concluded that manual erosion segmentation underestimates the extent of the damage. With the diffusion of Artificial Intelligence techniques, bone erosion has been identified in end-to-end systems [MHT+18], [RRSD19]. Unfortunately, in the radiology environment large and reliable data sets for training machine learning or deep learning algorithms are not fairly widespread.

5.4.2 Shape-based erosion identification methods

Since bone erosion not only modifies the tissue composition but also involves the bone morphology, accurate analysis of the bone shape provides information on the eventual presence of erosion sites on the bone surface. Thanks to Computer Graphics, 3D surface models are extracted from volumetric images to accurately represent the anatomy of the patient and 3D morphological analysis provides results that are comparable to image analysis. The evolution of erosion sites on wrist bones exploiting shape analysis on 3D models has been analyzed in a follow-up study [BTZ+15]. The features considered in this kind of studies regard changes in the geometry of the

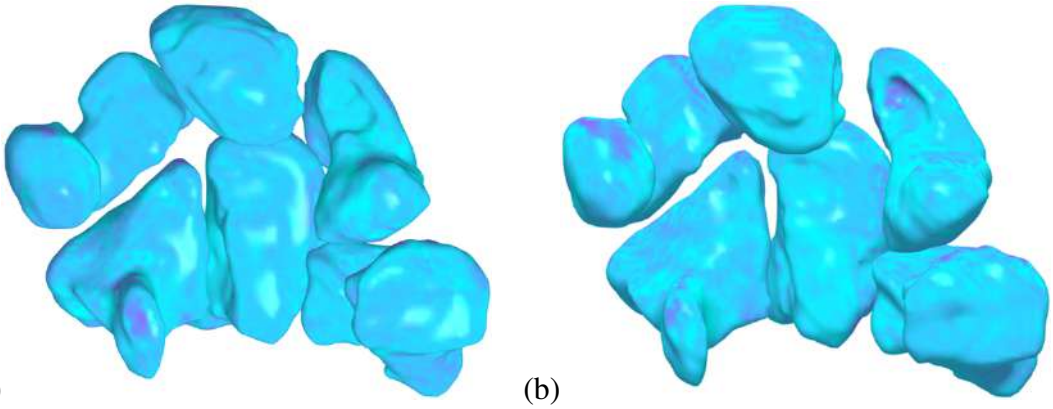

(a) (b)

Figure 5.16: Grey-levels mapping comparing the surface texture derived from the MRI at baseline time (a) to the one derived from the MRI at follow-up time (b). Both mappings are performed on the 3D surface at follow-up. Changes in texture mirror the degeneration of the tissue composition. Light blue values are associated with darker gray-levels and pink regions to brighter intensities.

3D shape. Indeed, leveraging parameters extracted from a 3D shape or from a comparison of various shapes, it is possible to support general radiology also on follow-up exams [BCPS16]. In this scenario, the work in [JLBC15] quantifies point-wise changes in surface morphology of the bones of the wrist. After the atlas selection, a non-linear registration method is applied to warp the corresponding bones of individuals in the population, on the basis of a regularized l^2 distance minimization. Where, as atlas we intend a representation for characterizing anatomy and anatomical variation, thus a model of the expected anatomy [DCdBdMW04]. Through the computation of a displacement field, the authors were able to show local differences in bone shape, and thus to track bone erosion evolution in Rheumatoid Arthritis.

5.5 Comparison of erosion evaluation method on the case-study

Considering that both image texture and shape analysis can provide insights on the erosion process, we studied a comparison of a geometry-based approach, which performs a geometric analysis of 3D segmented surfaces, and a texture-based approach, which analyses changes of the grey-levels in a neighbor of the bone surface. Moreover, we propose a combination of the two approaches, showing how it could overcome the limitation of the single ones taken separately. The carpal district is one of the most used for the diagnosis of rheumatic diseases since it is one of the first to show symptoms of the pathology. As described in Chapter 3.1, for each subject in the data set is also present a 3D surface model obtained from the MRI segmentation. Among

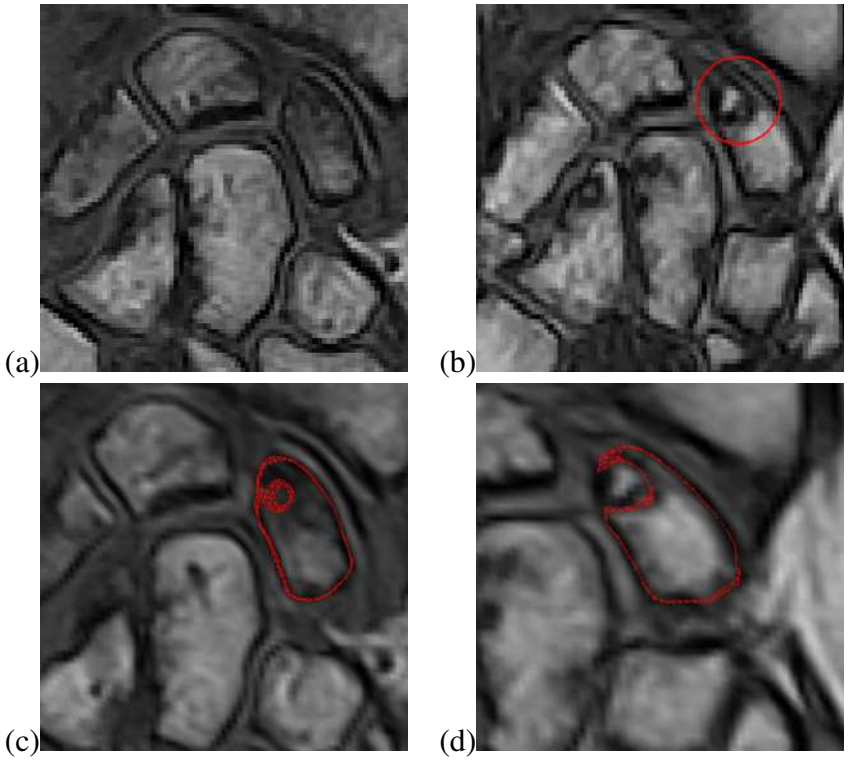

Figure 5.17: Bone erosion evolution in time: (a,c) volume at time t_1, (b,d) volume at time t_2. At time t_2 the Scaphoid presents an erosion (red circle in (b)). (c,d) Relation between the surface mesh at time t_2 with the volume, before (c) and after (d) the bone erosion.

those are present 6 follow-up exams, thus, for the relative subjects, it is possible to analyze how the pathology has progressed. Usually, in this case, with *baseline time* is intended the moment of the first exam/image scan, namely t_1. While the *follow-up time* indicates the second exam, performed after a few months or years (t_2). We now describe the three approaches chosen to study the erosion processes developed due to the pathology.

Geometry-based follow-up analysis In order to evaluate the differences in the geometry of each bone over time, we consider exclusively the 3D surface models of the carpal district at baseline time and the one at follow-up time. The analysis is carried out by a registration of the two carpal districts followed by an evaluation of local distances in order to localize shape changes and, thus, eroded regions. The registration of the district at baseline and follow-up is based on the Iterative Closest Point algorithm. A centroid translation is performed prior to the ICP algorithm [BM92] since the latter is designed to align partially overlapping meshes. In this way, the centroid translation coarsely superimposes the two districts and the following ICP refines the alignment. In Fig. 5.13, we show the registration between a baseline 3D surface (light blue) and

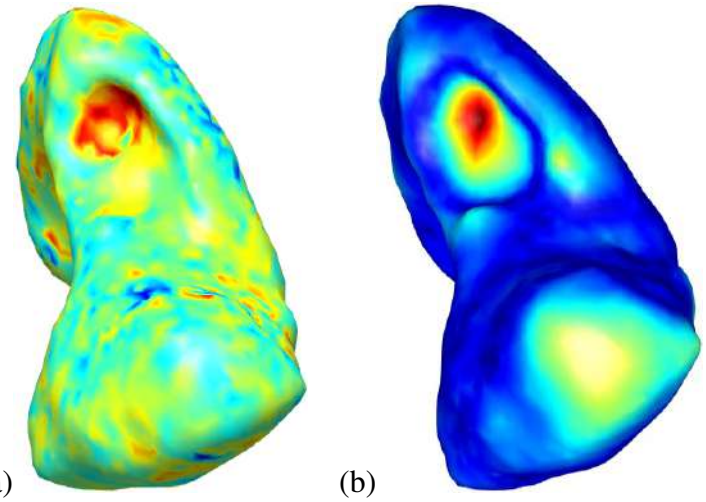

(a) (b)

Figure 5.18: (a) Difference between the external mapping of volume at time t_1 and external mapping of volume at time t_2. The erosion area (red) presents a major change of texture (higher difference in mapping values). (b) Distribution of the distances of each vertex of the mesh at time t_2 from the mesh at time t_1; high values of distance (red), typical of erosion regions, corresponds to the erosion depicted in (a).

a follow-up surface (red). Then, we compute the Hausdorff distance between the two districts to identify which bone could present an erosion. Ideally, the higher the distance, the higher the probability to find an erosion. Calling $\mathbf{X}_1$ the 3D bone surface at t_1 and $\mathbf{X}_2$ the registered 3D surface at t_2, we identify eroded bones by their Hausdorff distance is computed as: $d(\mathbf{X}_1, \mathbf{X}_2) := \max\{d_{\mathbf{X}_1}(X_2), d_{\mathbf{X}_2}(X_1)\}$. Where $d_{\mathbf{X}_1}(\mathbf{X}_2) := \max_{\mathbf{x}\in\mathbf{X}_1}\{\min_{\mathbf{y}\in\mathbf{X}_2}\{\|\mathbf{x}-\mathbf{y}\|_2\}\}$. The minimum distance is calculated using a KD-Tree algorithm.

This general analysis is followed by a local evaluation of the distribution of the minimum distance of each vertex of the surface at t_2 from the vertices of the surface at t_1. The results obtained in terms of distance distribution are then normalized to $[0, 1]$ in order to be comparable with the results obtained with the texture approach described further in this Section. The regions of the bone where the morphology has changed the most, present a higher level of distances (near to 1) in the distribution, highlighting possible erosion processes. To help physician in localizing the erosion on each bone, we set as threshold: $T = \overline{d_{\mathbf{X}_1}} + 3 * \sigma_{d_{\mathbf{X}_1}}$, were $\sigma_{d_{\mathbf{X}_1}}$ and $\overline{d_{\mathbf{X}_1}}$ represent the standard deviation and the mean of the distance distribution, respectively. In this way, vertices that have a distance higher than T are considered as belonging to erosion, and the remaining vertices are classified as healthy (Fig. 5.14).

Texture-based follow-up analysis The volume images in the data set are T1 weighted MRIs, whose voxel values have been normalized between 0 (black) and 1 (white). The grey-levels present in the image result from the signal received from the tissues, which is linked to their

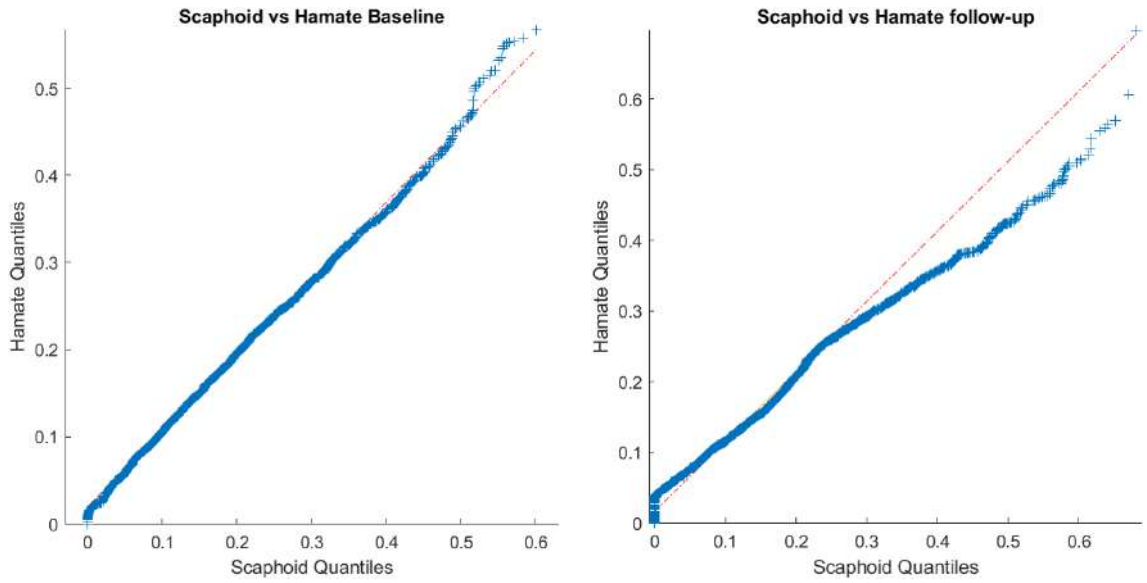

(a) (b)

Figure 5.19: Analysis of the changes in the distribution of grey-levels after the development of erosion. (a) Comparison of the hamate and scaphoid bones external mapping before the erosion (baseline exam): the two distributions can be considered equal. (b) Comparison of hamate bone (healthy) and scaphoid bone (eroded) in the follow-up exam: the erosion significantly changes the distribution of the scaphoid grey-levels. The two distributions can no longer be considered equal.

composition (Chapter 3.2.3). The erosion typically results from a previous mutation of tissue, whose origins can be different depending on the disease. Once the degeneration affects the bone tissue, then start the erosion, which usually destroys the cortical bone at first, and then proceeds with the internal layers. This means that, on the image, if an erosion presents itself over time, it can be identified through an analysis of the changes of voxels' intensities. Since significantly eroded bones present a higher Hausdorff distance, eroded regions are easily identified and it is possible to evaluate the grey-levels mapping locally on the single bone of interest. The distribution of the minimum distance of each vertex of the surface at time t_2 from the vertices of the surface at time t_1 highlights the region of the bone where the morphology has changed the most, possibly due to an erosion process. In this location, the analysis of the texture mapped on the surface can confirm and evaluate the erosion (see the pipeline in Fig. 5.15). The surface used for the analysis is the follow-up mesh because at time t_2 the pathological situation will be worse than at time t_1. Thus, localizing and evaluating the erosion region through volume changes is more discriminating on this surface. This solution permits to focus exclusively on the regions of the volume image that are near the bone surface by mapping the grey-levels in the neighborhood of the surface onto the 3D shape model. After properly co-registering the t_2 surface on the t_1 surfaces, the volume grey-levels at time t_1 are mapped on the surface at time t_2, exploiting the

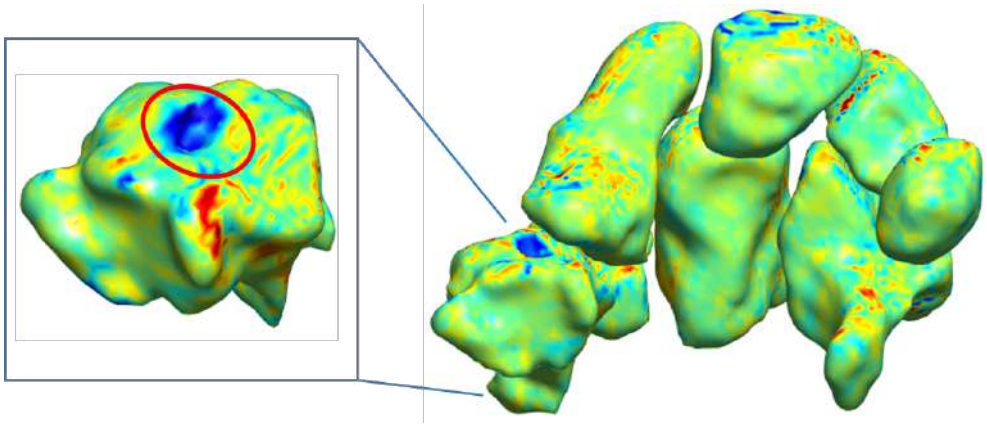

Figure 5.20: Texture difference values near to -1 can be associated with the healing process of the bone due to the therapy. The red circle indicates an erosion site where the eroded volume at baseline time was higher than the eroded volume at follow-up time.

grey-level mapping described in Chapter 4. Moreover, the grey-levels at time t_2 are mapped on the surface at time t_2 as well. In this way, the follow-up model can show either the volume situation at time t_1 and time t_2. In particular, we focus on the grey-levels immediately outside the segmented surface (Fig. 5.16), because often the erosion results from a degeneration of articulation regions. Figs. 5.17(a,b) show the volume situation at time t_1 and time t_2. Registering the t_2 mesh on the volume at time t_1 (Fig. 5.17(c)) and comparing it to the mesh at time t_2 on the volume at time t_2 (Fig. 5.17(d)), is evident that there are changes in the bone tissue. Those changes are highlighted coherently in the mapped mesh.

The variations in texture are highlighted by computing the difference between the grey-levels mapped from the baseline MRI and the ones mapped from the follow-up MRI. A higher value of difference indicates a region where the tissue has been substantially damaged, probably in relation to an erosion process. A color map associated with the difference values can describe the distribution of the changes in terms of tissue modification directly on the 3D surface. This confirms that the grey-levels mapping algorithm is useful, not only for global evaluation but is also coherent with local changes. It helps the classification of bone erosion sites on the surface and supports the bone object comparison over time. Indeed, the tissue information provided by the texture, confirm the findings supported by the shape analysis and correct misleading information that arises from the morphological comparison. As an example in Fig. 5.18(b), besides the red area (erosion), another region of the bone present slightly high distance values (yellow) from the geometrical analysis. Although Fig. 5.18(a), in the same areas, do not exhibit a deep change as for the erosion case. Thus, the distance values are to be attributed to the variability introduced by the registration phase. To verify that the presence of erosion can actually change significantly the distribution of grey-levels, we compared a healthy bone with the eroded one before and after the development of the erosion. In Fig. 5.19, the Scaphoid *external mapping* is compared to the

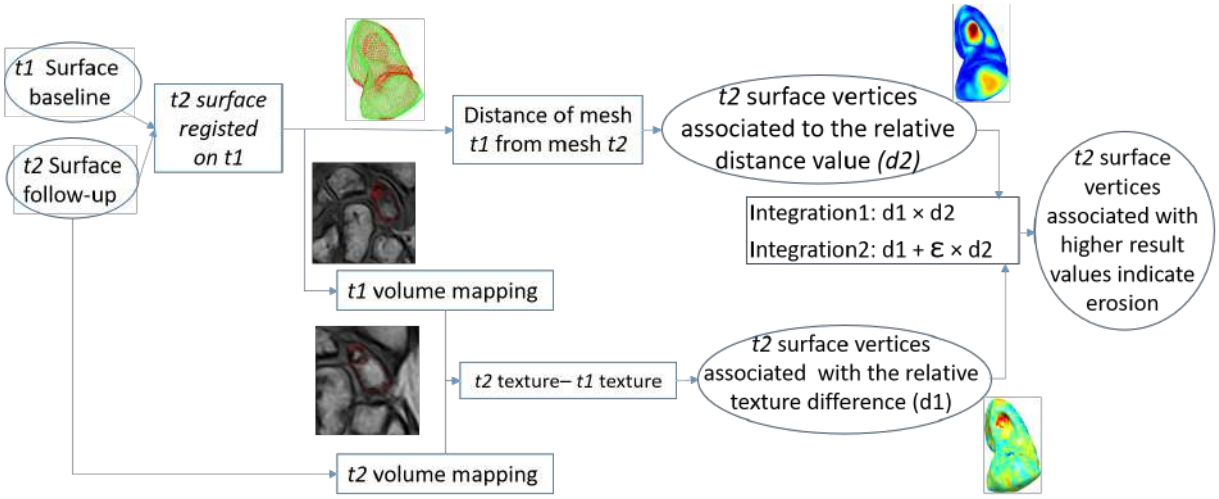

Figure 5.21: Pipeline of the follow-up integration method.

Hamate *external mapping* using a qq-plot. At time t_1 (Baseline exam), the plot results lay on the bisector line, thus the two distributions can be considered equal (Fig. 5.19(a)). The same comparison is performed in the follow-up exam, after the development of the erosion in the Scaphoid bone. In this case, the two distributions can no longer be considered equal (Fig. 5.19(b)). Indeed the change in the grey-level distribution is significant.

5.6 Erosion identification integration method

The first approach described in Section 5.5 focuses exclusively on the geometric differences that occur over time, without considering the tissue information. Whereas, the second method is centered on the degeneration of tissue composition. In the following, we will present two possible approaches that aim to integrate the information extracted from the two methods seen so far. The analysis of the local distance distribution between the district's bone at baseline and at follow-up associates, to each vertex composing a bone model at follow-up time, the value of the distance from the nearest vertex of the baseline correspondent bone. Similarly, from the texture analysis, each vertex of the follow-up district is associated with the value of the difference between the image information at baseline and follow-up. In this way, each vertex composing the surface model of the follow-up is associated with a feature vector, characterized by geometrical and texture information. In particular, the texture information present intensities in $[-1, 1]$ since they are obtained from the difference of gray levels between 1 and 0. A value of texture nearer to 1, indicates a major change in the intensity of the image voxels and, thus, a radical change in tissue composition over time. A value of texture nearer to -1, instead, could indicate a healing process,

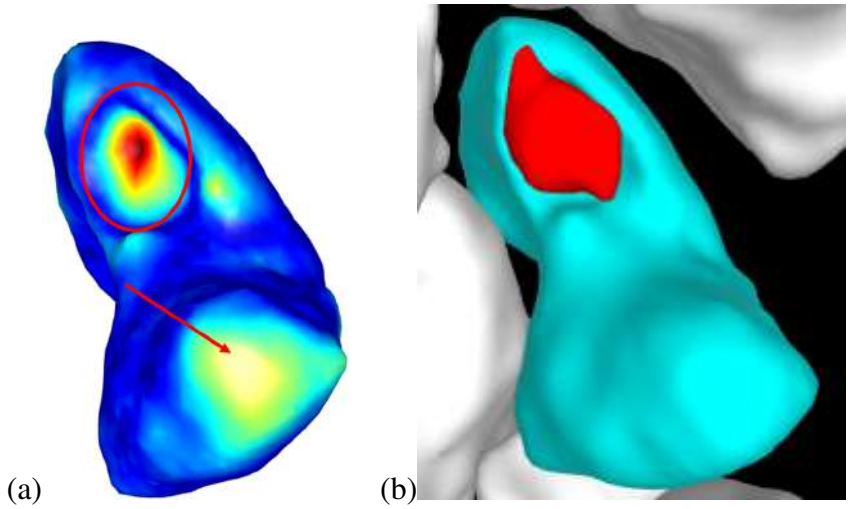

(a) (b)

Figure 5.22: Scaphoid bone follow-up analysis of a patient with Rheumatoid Arthritis. Comparison of the erosion region identified by the experts (a) with the result of the geometrical analysis (b). The erosion is correctly identified (circle), but the distance distribution shows higher values also in an area that does not present erosion (arrow).

where the extension of an existing erosion has decreased due to the therapy [BTZ+15]. As an example Fig. 5.20 shows the identification of an erosion where the texture provides negative values. In correspondence of that region, in the data set evaluated by experts, the eroded volume is $171mm^3$ at baseline time and $57mm^3$ at follow-up time, indicating a reduction of the erosion. In this case, the bone tissue, probably due to the therapy, has healed over time, bringing the value of texture difference near to -1. The value of the distance, instead, can vary from 0 to 1 depending on the entity of the geometric deformation.

Fig. 5.21 shows a flow-chart of the two options leveraged to integrate the information provided by the geometry to the ones provided by the texture. The core difference between the two types of integration resides in how the information of the texture is combined with the relative information on the distance. The first option is to multiply the value of the geometry information to the one of the texture information for each vertex. In this way, if a variation in geometry is associated with a high variation in texture (value near to 1), then the result will be a higher total value. Whereas, if a geometry change is not associated with a major change in texture (value next to 0) then the influence of the geometry variation will be diminished, bringing to a lower total value. In this way the erosion sites will be highlighted only if texture as well as geometry, show a major variation, confirming that the bone has developed both a change in morphology and in tissue composition.

As a second option, we consider a linear combination of geometric and texture information. Calling d_2 the distribution of the distances obtained by the geometry analysis and with d_1 the distribution of the texture changes in the grey-levels analysis, the resulting distribution will be

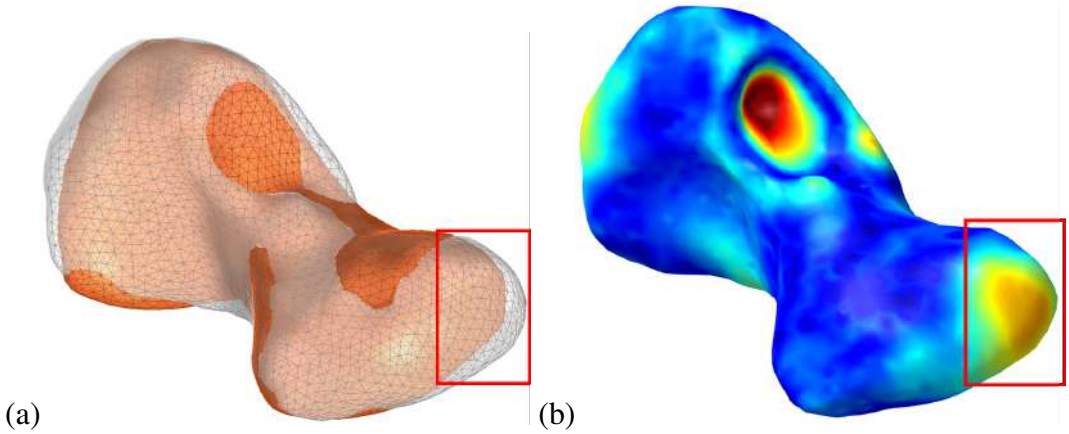

(a) (b)

Figure 5.23: Inaccuracies of the registration method (a) with the relative influence on the identification of erosion regions (b).

given by $d_1 + eps * d_2$ where ϵ is in the interval $[0, +\infty)$. Varying the value of ϵ, it is possible to give more emphasis to the geometric or the texture information. If the clinician wants to surely identify all erosions, even the smaller, ϵ will be increased. A low ϵ is more suitable for the identification of larger and persistent erosions. Finally, an interactive visual representation of the integrated results is achieved by changing ϵ and helps the user to better analyze the input data.

It is presumable that the relevance of the geometry to the final result, managed by ϵ, has a correlation with the stage of the pathology. Thus the manual setting of the parameter permits the physician and the rheumatologist to adjust the visualization accordingly to their previous knowledge on the case, that is the type of rheumatic disease and the relative mechanism of erosion development. Moreover, the expert adjustment of the parameter could be guided by the duration of the pathology for following monitoring exams.

Results and discussion As already explained, the carpal area represents one of the most complicated skeletal districts of the whole human body. It is constituted by eight small bones that articulate with each other in a small space extension. Such a complicated arrangement is fundamental for the high number of fine movements that the wrist can perform. Since the wrist represents one of the districts that mostly suffer from damages due to rheumatic pathologies, it is usually studied by physicians as a reference point for the analysis of the evolution of the disease. One of the most used techniques for this purpose is the analysis of low-field MRI such as the ones exploited in our data set. The highly complicated anatomical structure and the low-field images represent the core challenges of the approaches presented in this Chapter.

Regarding the geometry-based analysis, in Fig. 5.22 we compared the identification of erosion sites performed by experts in the field with the result of the geometry-based analysis. In this case, the erosion site is correctly identified by the geometrical analysis, which presents a partic-

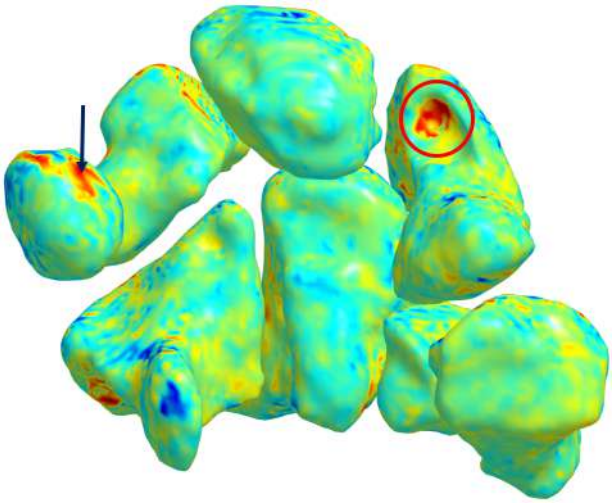

Figure 5.24: Erosion localization results in the texture-based approach. The erosion is correctly identified (circle) but other healthy areas (arrow) are false-positives due to low image resolution. Blue and light blue colors represent negative texture values (blue corresponds to -1); green areas present values near to 0. Yellow and red represent increasing values where red corresponds to 1.

ularly high value of distance distribution in the exact location indicated by the experts. However, the results show also the presence of *false positives*: areas of the bone that are classified as erosion but are actually healthy regions. This misclassification is related to the inaccuracies of the registration process. Indeed, it is presumable that even the registration phase of the geometrical approach could bring errors in the evaluation since most of the wrist bones are small and do not present relevant shape features. In particular, the rounded and symmetric shape of most of the bones affects the accuracy of the alignment of the district. According to Fig. 5.23, in the region where the two bones are not well aligned, the geometrical analysis shows a possible erosion site. Indeed, in the area which presents a less accurate alignment, the distance distribution presents higher values than expected, even if no erosion process is involved. Nevertheless, if an erosion process is actually present it hardly goes unnoticed in the geometrical analysis.

Regarding the image texture analysis, the difference between the texture at baseline and follow-up times shows an inhomogeneous behavior. It is clear, though, that the higher values of difference in texture are located in an erosion region. This result is coherent with what expected since a major change in tissue composition implies a higher value of difference between the texture at the two different times. As for the geometrical approach, even in this case, the location of the erosion is correctly identified, however, a series of false-positive are present, even if characterized by lower values of difference with respect to the real erosion locations (Fig. 5.24). The inhomogeneities, as well as the false positives, can be explained by the resolution of the MRI images. Indeed, the experiments of this study are performed using a low-field T1 weighted MRI, which implies that the resulting scans have a low resolution. This factor influences the results

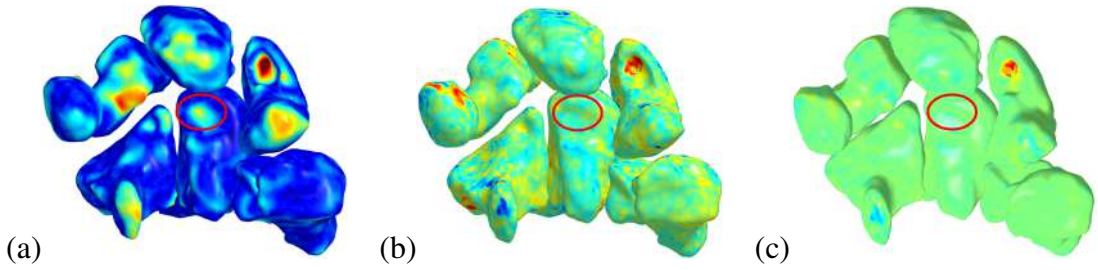

(a) (b) (c)

Figure 5.25: Comparison of the (a) geometry-based approach, (b) texture-based approach, and (c) their integration through the multiplication of the geometric and texture intensities, on the same follow-up district. Warm colors represent the higher intensity values (red as the highest values), cold colors represent the smaller values in the distribution. The red circle indicates the small erosion identified by the geometry-based approach but not by the integration method.

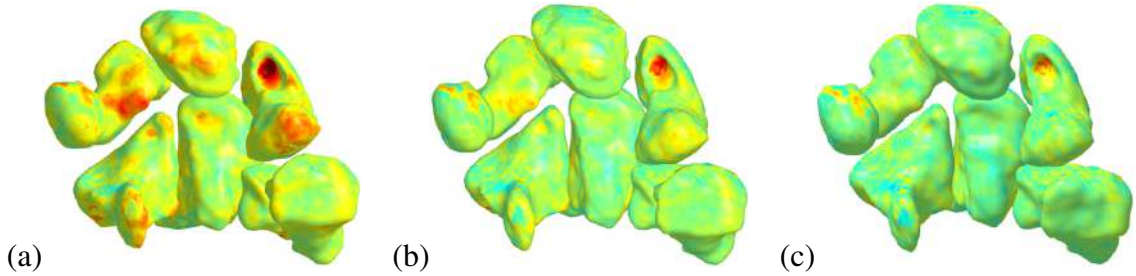

(a) (b) (c)

Figure 5.26: Linear combination: $d1 + \epsilon * d2$ where $d1$ is the texture distribution and $d2$ is the geometry distribution integration method varying the value of ϵ (a) $\epsilon = 1$, (b) $\epsilon = 0.5$, (c) $\epsilon = 0.2$. Warm colors correspond to higher intensity values of the distribution (red as highest value); cold colors represent smaller value in the distribution.

obtained in the search for erosion using a texture-based approach, thus increasing the resolution could lead to more precise and accurate results.

The integration methods are thought to merge the information provided by the geometrical analysis with the ones extracted from the texture analysis. In Fig. 5.25, we compare the results obtained from geometric, texture, and integration approaches. In this case, the integration is obtained using the multiplication option. As visible, the false positives, in the integration approach, are no longer present since just the areas that present an actual erosion show higher values. The overall result is, indeed, more homogeneous, indicating that geometry and texture information compensate each other, discarding misleading classifications due to low image resolution or registration inaccuracies. Nevertheless, the integration result could miss some newly developed and small erosions, as it is possible to see in the example reported in Fig. 5.25. Here the red circles indicate the small erosion that is underlined by the geometrical approach but is not particularly evident in the texture changes. This suggests that the erosion could be at its beginning, implying a minor change in geometry and a small change in the cortical bone tissue, which could be still

partly intact.

The integration approach that considers the linear combination of the texture and geometry, is more flexible compared to the multiplication approach. Indeed, varying the value of ϵ, it is possible to regulate the result based on the necessity. Fig. 5.26, presents three different integration results according to the variation of the ϵ value and shows that by diminishing the relevance of the geometric information ($\epsilon = 0.5$, $\epsilon = 0.2$), the values lead to a more homogeneous result. This means that the false positive areas decrease in number along with the reduction of geometric information relevance. However, an excessive reduction of the relevance of the geometrical information brings also to the presence of *false negatives*, that is the misclassification of erosion regions as healthy areas. Overall, this second approach permits to adjust the focus of the search and to reach the desired trade-off between false negatives and false positives.

The presence of false positives shows to the physician a worsened situation and, thus, a higher level of bone degeneration with respect to reality. Whereas, the presence of false-negatives induces an underestimation of pathology progression gravity. Indeed, the false-positives or false-negative could alter the result of the therapy performance analysis, thus the identification of a trade-off between the two is important.

The possibility to manually change the value of ϵ provides also the opportunity to support the quantitative evaluation metrics used for erosion in rheumatic diseases. As an example, the OMERACT Rheumatoid Arthritis MRI Scoring system (RAMRIS) and the EULAR-OMERACT Rheumatoid Arthritis MRI reference image atlas, are established standards for synovitis, bone edema, and bone erosion scoring guided by standard reference images [ØEM$^+$]. The bone erosion, in particular, is evaluated separately for each bone and the scale is $0 - 10$, based on the proportion of eroded bone compared to the assessed bone volume, judged on all available images. Where 0 corresponds to no erosion; 1 to $1 - 10\%$ of bone eroded; 2 to $11 - 20\%$, and so on. In this way, the erosion gravity is indicated by the (1-10) score. With a manual tuning of ϵ, given the score, it could be possible to assess the level of erosion with higher precision inside each scoring class, showing interactively the result of the evaluation on the 3D model.

Finally, it is important to underline that both integrations between geometry-based and texture-based analysis proposed in this Section do not need any previous knowledge regarding the analyzed district. Indeed, the methods do not require the computation of mean shapes or atlases in order to perform the follow-up analysis. The only requirements are the images and segmentation at the two points of time to be compared, making the analysis deeply patient-specific. Moreover, the integration methods are quite general, since they can be applied to different anatomical structures, independently on how the bone models are obtained and on the imaging technique.

Chapter 6

Grey-levels Mapping for Segmentation

6.1 Evaluation and comparison of segmentation methods

As introduced in Chapter 2, the scope of image segmentation is to partition a digital image into meaningful regions, considering both visual content and local properties of homogeneity and contrast. Thanks to extensive research in the field, many different approaches, and algorithms for image segmentation have been developed. However, few methods assess whether one algorithm produces a more accurate segmentation than another, whether we consider a particular image or set of images, or for a whole class of images. In this context, we present an overview of methods for the evaluation of segmentation algorithms; this analysis will lead us to (i) propose a novel approach that provides physicians with tissue information related to the segmentation (Section 6.2) and (ii) develop an unsupervised evaluation method (Section 6.3), based on the method described in Chapter 4. Designing a good measure for segmentation quality is a well-known hard problem and we can apply different criteria for the definition of a good segmentation. The criteria that define a segmentation are often application-dependent and hardly explicable, however, for many applications the difference between a favorable segmentation and an inferior one is noticeable. Segmentation evaluation has been studied less than segmentation approaches. Nowadays, the evaluation of the effectiveness of a segmentation method is commonly conducted through subjective evaluations, which imply a visual comparison, performed by a human, of the image segmentation results for different segmentation algorithms. This process has intrinsic limits due to the evaluation of a small number of segmentation methods. Another common method is the supervised evaluation, where a segmented image is compared against a manually segmented or pre-processed reference image. Such an image must be provided by experts and used for comparison with the segmentation to be evaluated [ZFG08]. Different problems arise from this situation: in addition to subjectivity, previous knowledge of the expert could bias the results, especially when the lack of visual information is filled by Gestalt unconscious mechanisms, such as reification. This kind of evaluation method requires user assistance, thus resulting unfeasible

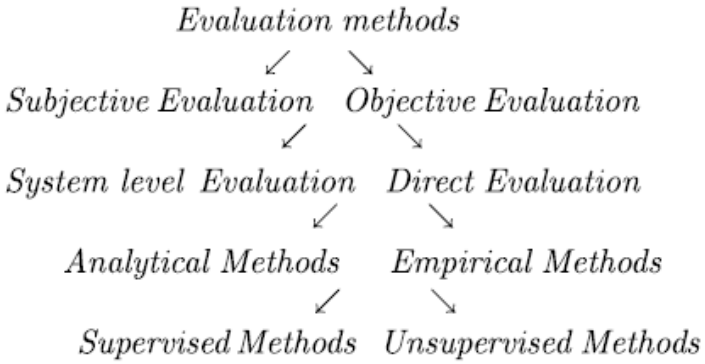

Figure 6.1: [ZFG08] Calssification of segmentation evaluation methods.

in many vision applications. Given these premises, it is clear that unsupervised methods are necessary in order to achieve an objective comparison of different segmentation methods and different parameterizations of a single method. An important constraint is the independence of the unsupervised methods from human visual comparisons or of a comparison with a manually-segmented or pre-processed reference image [ZFG08].

Previous works on the evaluation and comparison of segmentation methods can be divided hierarchycally [ZFG08] (Fig. 6.1). The first two main categories are *subjective evaluation* and *objective evaluation*, depending on whether the evaluation is performed visually by a human or not. Nowadays, subjective evaluation is the most used method in medical image analysis. Subjective evaluations require a visual exam performed by a human, with all the problems that can derive from such a solution. First of all, visual or qualitative evaluation is inherently dependent on the person who analyses the image. Indeed, subjective evaluation scores may vary significantly from one expert to another, since each person has his/her own standard for assessing the quality of segmentation. Furthermore, the results of the evaluation may depend also on the order in which evaluators analyze the segmentation results. For these reasons obtaining an unbiased judgment of the accuracy and effectiveness of a segmentation algorithm is a difficult task and requires a large visual evaluation study. Indeed, a large set of test images, as well as a high number of expert evaluators, must be involved to provide a visual comparative evaluation without any particular bias. The set of test images must contain a sufficient number of examples representative of the category of images that the segmentation algorithm will analyze. Following the same principle, also the group of human evaluators must be sufficiently large in order to represent the typical human observer. In medicine, obtaining such a high number of images is particularly challenging given ethical and privacy issues, especially if the data set requires validations by experts or bioethics committees. Moreover, it is necessary to establish well-defined guidelines to reduce the presence of favoritism between different algorithms and parameterizations [ZFG08]. It is clear now that such subjective methods are not suitable for a real-time system with the scope of deciding between different segmentation algorithms, or even different parameterizations of a

single segmentation algorithm.

In the *objective evaluation* some methods analyze the impact of segmentation on larger applications, while others look at the segmentation method independently. Indeed, it is plausible to divide objective evaluation methods into *system-level evaluation* and *direct evaluation*. Indeed, *system-level evaluation* methods represent an alternative way to intend the evaluation of segmentation. They examine the impact of different segmentation methods on the overall system. In this approach, the goodness of a segmentation method is valued on the basis of the empirical system results. However, this type of evaluation method is indirect. Indeed, the system-level results from different segmentation methods just mean that the characteristics of the results were more favorable in that particular system.

Basing on whether the method itself or the generated results are being examined, the direct evaluation can be further subdivided into *analytical methods* and *empirical methods*. In particular, *analytical methods* judge the goodness of the segmentation not on the output of the algorithm, but on certain properties of the algorithm itself: processing strategy, processing complexity, resource efficiency, and segmentation resolution. Indeed, it is important to notice that these methods evaluate algorithmic and implementation properties, which are usually independent of the final result of the segmentation process. Finally, the empirical methods can be divided into *supervised methods*, if they require a ground truth reference image, or *unsupervised method* if not.

With *supervised methods* we intend the evaluation of segmentation algorithms by comparison of the results with a manually-segmented gold-standard. This kind of evaluation is also known as *empirical discrepancy methods* or *relative evaluation methods* since the degree of similarity between the human and machine segmented images determines the quality of the segmented image. One potential advantage of supervised methods over unsupervised methods is that the direct comparison of a segmented image and a reference image provides a finer resolution of evaluation, thus, discrepancy methods are commonly used for objective evaluation. Different discrepancy measures have been proposed for segmentation evaluation. The earliest discrepancy methods were based on the number of misclassified pixels with respect to the reference image, and associated penalties proportional to the distance to the closest pixel that was correctly identified in the region [YMB77]. An alternative is to base the discrepancy method on the differences in the feature values measured from the result of the segmentation and the reference image [Z$^+$17]. These methods have been developed over the years in order to solve problems where the number of objects to be segmented is different from the objects presented in the reference image. There are also a variety of discrepancy methods for the evaluation of edge-based image segmentation methods [PGAN16]. Finally, the evaluation can be based on a multi-dimensional fitness/cost space with multiple discrepancy metrics, in contrast with other evaluation methods that are based on a single discrepancy metric [EMT02].

Unsupervised evaluation methods are also known as *stand-alone* or *empirical goodness* methods and do not need a reference image, but instead evaluate a segmented image depending on if it matches a set of characteristics of segmented images interpreted by humans. The capacity

to work without reference images permits unsupervised evaluation to work on a wide range of conditions (or systems) and with many different types of images. The key advantage of this method is that it does not require a manually-segmented reference image as a gold standard for the evaluation. This aspect is fundamental for general-purpose segmentation applications where a large variety of images with unknown content and no ground-truth need to be segmented. Unsupervised objective evaluation methods offer the ability to automatically set the segmentation algorithm parameters and thus allow self-tuning. Usually, the segmentation parameters are selected manually exploiting the set of parameters that generate the best overall segmentation results on test images. In this way, the parameters for the segmentation algorithm are determined during system development, prior to system deployment. However, these parameters might reveal inappropriate for the segmentation of later images. Thus, it would be ideal to have a self-tuning segmentation method able to adjust the segmentation parameters dynamically. Only unsupervised evaluation methods offer this ability for any generic image since they do not need a reference image [ZFG08]. These characteristics make this kind of evaluation method particularly suited for automatic control of real-time systems.

In order to perform an unsupervised evaluation, it is necessary to define the criteria that discriminate the goodness of a segmentation result. Those criteria were described already in 1985 [HS85] as *Characteristic criteria*, that regard the objects in the image, and *Semantic criteria*, that regard the possibility that each region is considered a single object by humans:

- regions should be uniform and homogeneous with respect to some characteristics (characteristic criterion);
- adjacent regions should have significant differences with respect to the characteristic on which they are uniform (characteristic criterion);
- region interiors should be simple and without holes (semantic criterion);
- boundaries should be simple, not ragged, and be spatially accurate (semantic criterion).

Various segmentation evaluations are based on the characteristic criteria since semantic criteria tend to be application-dependent or object-dependent. In practice, the principal metrics used in the evaluation of the segmentation can be generally divided into three categories: the ones measuring *intra-region uniformity*, *inter-region disparity*, and *semantic cues* of objects. These metrics can also be combined exploiting weighted sums of inter-region and intra-region metrics or through the division of intra-region metrics by inter-region metrics, to give a composite effectiveness measure [ZFG08]. We underline that all the categories presented in this Section are not mutually exclusive since an evaluation method can result from the combination of techniques belonging to different categories.

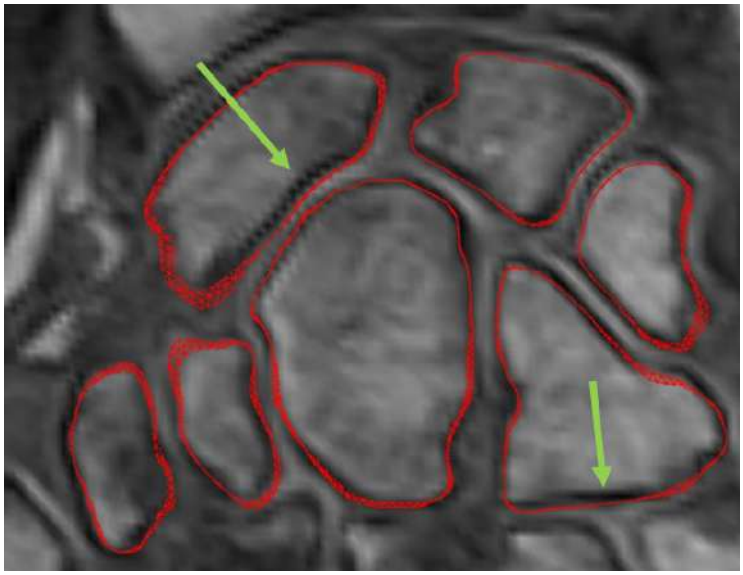

Figure 6.2: 3D segmented surface (red) superimposed to the volume slices: in some regions, the darker tissues constituted by synovial structures and cortical bone lie inside the surface (green arrows).

6.2 Tissue relation with segmented surfaces

Evaluation of grey-levels gradient To further study the segmented objects in the context of medical images, we compare the grey-levels of the voxels outside and inside the surface. Thus, we present the application of the grey-levels mapping, described in Chapter 4, to a specific clinical problem. Once obtained the Euclidean, external, and internal mappings, the grey-levels comparison is achieved subtracting, for each surface vertex p_i the value of the *external mapping* to the *internal mapping*. Given the voxels intensities relation with the tissue composition (Section 3.2.3), if the edge of the bone is placed between the cortical and the marrow bone tissue, then the *internal mapping* should be brighter than the *external mapping*, leading to a positive value. If the edge is placed outside the cortical tissue, then darker *internal mapping* grey-levels will make the difference negative. The reason why the segmentation analysis is based on the comparison between internal mapping and external mapping is due to the high anatomical variability and the low resolution of the images, which make unreliable the use of a global threshold to distinguish between dark and bright grey-levels. Indeed, by comparison, the internal mapping evaluation is patient-specific and scan-specific.

Results and discussion An analysis of the mapped gray levels provides information regarding the choices made in the segmentation phase, and thus regarding the tissue relation with the segmented object. Fig. 6.2 shows that, in certain regions, the cortical bone tissue is included in

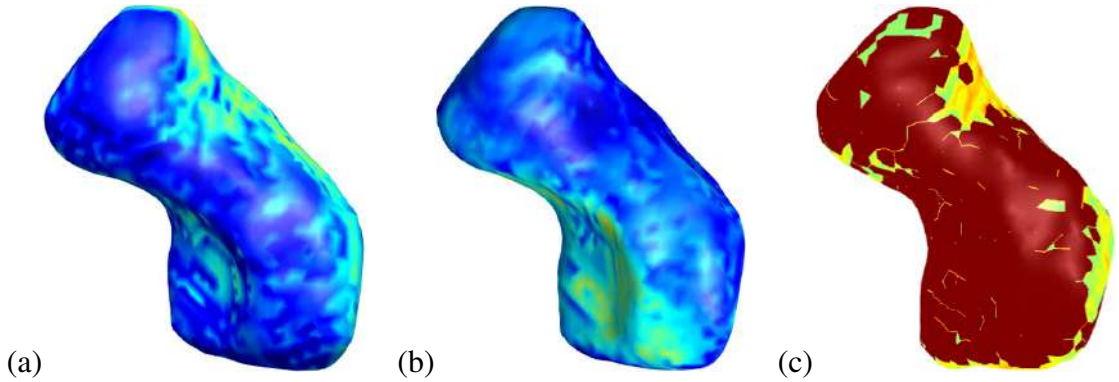

Figure 6.3: (a) Internal mapping results on the scaphoid bone: darker areas on the surface indicate that the volume voxels internal to the bone are darker. (b) External mapping result: in the same region where the internal mapping results darker, the external mapping is brighter. (c) Difference between internal and external mappings: red areas indicate the vertex with a negative difference value, and thus, the presence of cortical tissue inside the surface.

the segmentation, while in other regions it is excluded from the bone object. The proposed mapping can exhibit, directly on the 3D surface model, the choices taken in the segmentation phase. In this way, huge information regarding the anatomical structures that will be expected inside and outside the bone is provided to the observer. If the cortical bone is comprehended in the 3D surface, outside of it there will be ligaments, tendons, and articulation tissue directly. If the cortical bone is excluded, then immediately outside the surface there will be the cortical region and, only after that, all the others. The edge position of the segmentation can be appreciated in both internal and external mapping, as depicted in Fig. 6.3(a,b), and visualized directly on the surface (Fig. 6.3(c)). This kind of information can not be deducted from the sole surface since the surface itself is derived from a binary image.

The absolute value of the difference between the internal and the external mappings can be useful to quantify how the choices taken during the segmentation phase influence the mapping result. Indeed, the absolute difference can be considered as a measure of the difference between the tissues inside and outside the bone. A higher difference indicates that the edge of the object has been located between two well distinct tissue; a smaller difference indicates that the edge of the object is placed between tissues that are not clearly distinguishable. The latter situation happens when the cortical bone is considered as part of the bone itself. Fig. 6.4 shows the cumulative histograms of the absolute difference in two hamate bones: the blue one presents a higher portion of cortical bone considered as part of the object w.r.t. the red one. The blue cumulative histogram shows a steeper trend, indicating that a higher portion of the bone presents a low difference between inside and outside. The red cumulative histogram, instead, shows a gradual growth, meaning that a larger portion of the segmentation edge has been placed between two distinct tissues.

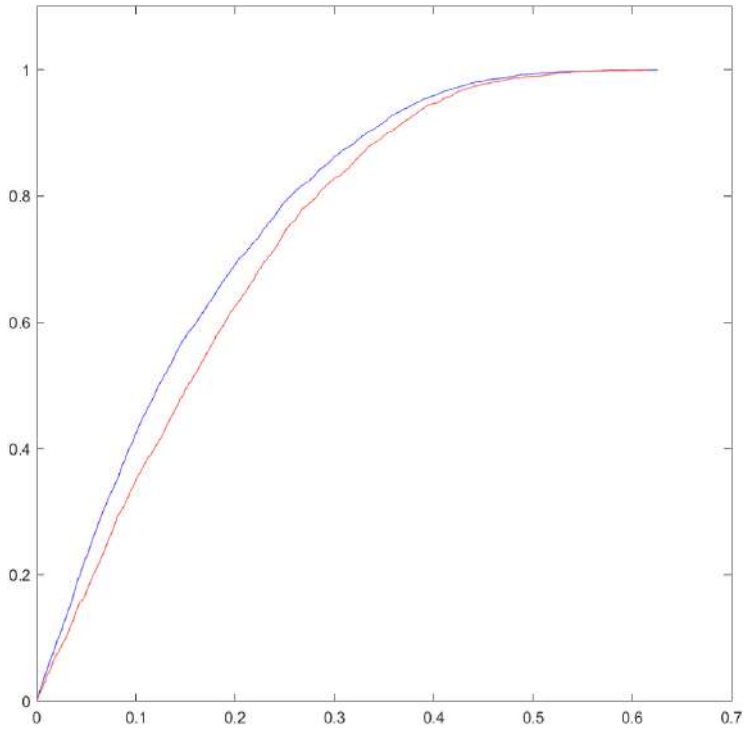

Figure 6.4: Cumulative histogram (CH) of the absolute difference between internal and external mapping. Both CHs refers to a hamate bone. The blue one presents a higher portion of cortical bone inside the bone surface. The red one presents a higher portion of cortical bone outside the surface. The red more gradual trend in the left part of the graph indicates that its segmentation edges are placed in a clearer tissue interface position w.r.t the blue one.

6.3 Unsupervised segmentation evaluation proposal

In the clinical application of segmentation processing, expert radiologists or physicians performing the image segmentation insert involuntarily their previous knowledge. In the particular case-study treated in this Thesis (the carpal district) doctors tend to estimate the cortical surface and use the cortical-trabecular interface as a starting point for the segmentation process. This is a direct consequence of the combination of a-priori knowledge and data, which yields the edge of the segmented bones to include dark voxel other than the bright ones.

Usually, an automatic segmentation method, instead, is completely based on the grey-levels of the volume and represents better the interface between cortical and trabecular bone. This outcome discrepancy between the manual and automatic segmentation may lead to errors in the evaluation of the segmentation result when the ground-truth is obtained from different experts' segmentations. Therefore, in collaboration with the University of Genova (Professor Silvana Dellepiane and Marco Trombini), we developed an automatic method for unsupervised evalua-

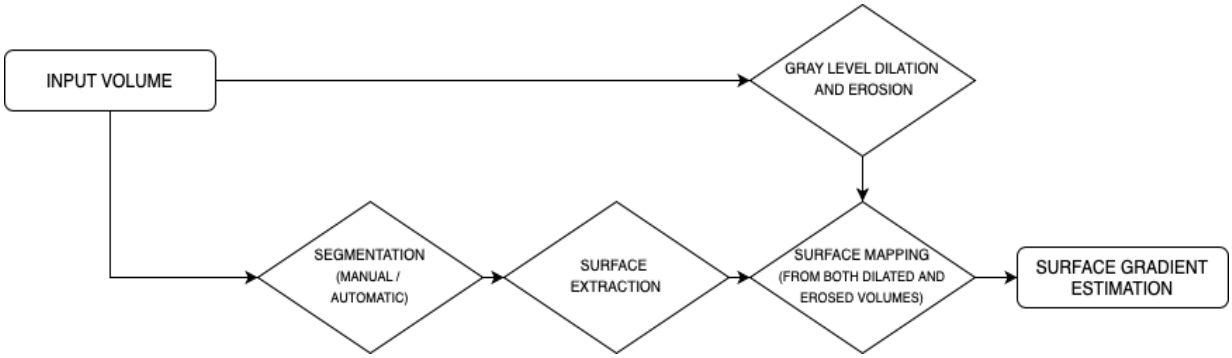

Figure 6.5: Pieline of the developed unsupervised segementation evaluation method.

tion of manual and automatic volume segmentation, which aims at finding a user-independent evaluation of segmented results exploiting the integration of volume- and surface-based analysis. The pipeline of the developed method can be seen in Fig. 6.5. The main objective of this application is to evaluate if the surface extracted from a segmented volume is coherent with local contrast information regarding the interface between the internal and external voxels of a Region Of Interest (ROI). It is this quantitative objective evaluation that can be considered a valid measure to evaluate segmentation accuracy and to compare different segmentation results. The core of this evaluation is then the reliable gradient since its measure provides information on the variation of the grey-levels across the surfaces, in the direction normal to the segmented surface. Usually, the best location of the interface between voxel inside and outside the ROI corresponds to the local maximum contrast. Thus, it is possible to think about the comparison between two different segmentations in terms of a statistical analysis of the local gradient values.

The segmentation considered through the development and testing of this unsupervised evaluation method were both manual and automatic segmentation. As manual segmentation, we exploited the ones present in the data set (described in Chapter 3), performed by medical experts in MR volumes evaluation, by using the tool RheumaSCORE (Softeco Sismat S.r.l.). The automatic approach applied corresponds to the method in [GD15]. It consists of a graph-based, unsupervised, and adaptive method, which therefore does not require any a-priori knowledge. Here, at first, the volume is mapped into a connected, undirected, and vertex-weighted graph. Then, a cost function, which assigns cost values to the vertices rather than to the edges of the graph, is defined. In this manner, the algorithm does not consider the length of the path connecting nodes, i.e. the dimension of the object to segment, but only their difference in terms of grey-level. Then, based on a specific propagation mechanism, the method finds a Minimum Path Spanning Tree (MPST), and graph-cut yields to the segmentation.

The proposed evaluation method consists of mapping a gradient measure onto the bone surface, extracted with the marching cubes algorithm [LC87], from the segmented bone. Since the input

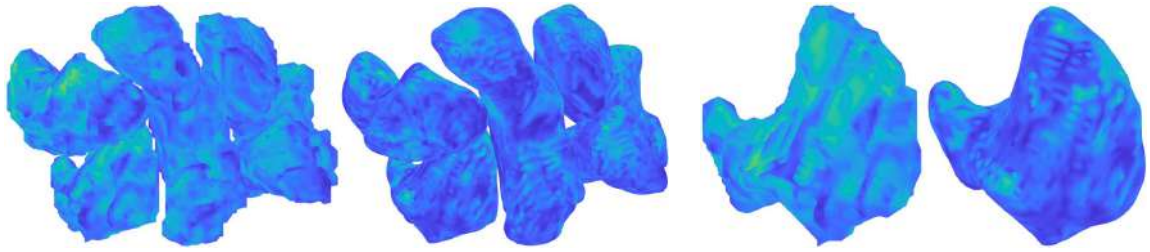

(a) (b)

Figure 6.6: Gradient outer estimation mapping on (a) the whole district and (b) the hamate bone, obtained from automatic (a,b left) and manual segmentation (a,b right). The gradient values reside between 0 and 1, where higher values correspond to the yellow areas of the colormap, while lower values to blue.

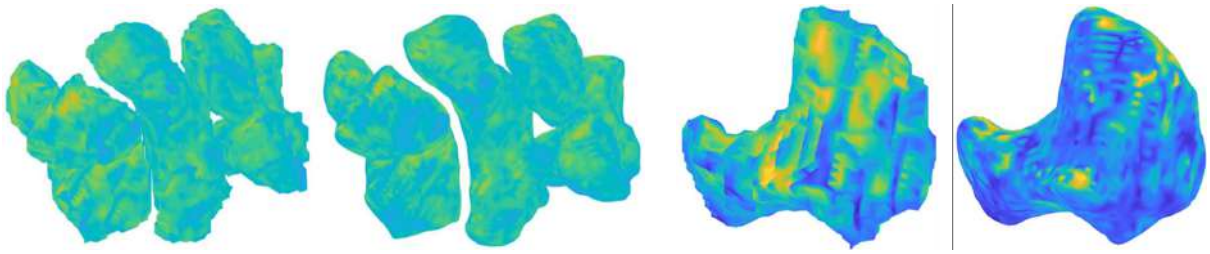

(a) (b)

Figure 6.7: Gradient Euclidean estimation mapping on (a) the whole district and (b) the hamate bone, obtained from automatic (a,b left), and manual segmentation (a,b right). The gradient values reside between 0 and 1, where higher values correspond to the yellow areas of the colormap, while lower values to blue. As expected the automatic segmentation presents more yellow areas.

images are binary, the selected iso-value is 1 and the segmented bones are represented as 3D triangle meshes, that can undergo the grey-levels mapping algorithm (Chapter 4).

Instead of mapping the raw volume grey-levels onto the surfaces, the images are pre-processed through morphological processing, in particular applying dilation and erosion operations [SS00]. Indeed, a way to reduce the human factor influence on segmentation is to apply a pre-processing operation on the images, especially when the starting volume is scanned with low-intensity field tomography that makes the ground-truth development even harder. The effect of morphological dilation and erosion is the reduction of small differences between segmentation results since both dilation and erosion take into account information related to a voxel neighborhood. Thus, the gradient measure obtained from pre-processed images benefits of a better localization of the actual separation between cortical and trabecular bone tissues (bright and dark areas). Indeed, the morphological dilation and erosion operations are performed on the raw volume, before the mapping application, in order to extend bright and dark areas, respectively.

Once obtained these two pre-processed volumes, the mappings of the voxel values are performed on the surface mesh. Thus, the two resulting volumes are used separately as input to the mapping phase, which associates each vertex of the triangle mesh with the grey-level of its closest voxel. The result of the mapping phase consists of two differently colored surfaces, one obtained from the dilated volume and one from the eroded volume, such results are subtracted from one another. The computation of their difference provides a sort of grey-level gradient measure on each vertex of the triangle mesh. The estimated gradient in each mesh node results in the difference between the dilated and eroded grey-levels. All the different mapping criteria presented in Chapter 4 are applied, in order to obtain different gradient estimations. In particular, we exploited:

- Euclidean mapping of the dilated and eroded volumes, obtaining the *Euclidean estimation*;
- Internal mapping of both dilated and eroded volumes, obtaining the *inner estimation*;
- External mapping of the dilated and eroded volumes, resulting in the *outer estimation*;
- A gradient obtained from the difference of dilated gray levels from the external mapping and eroded grey-levels from the inner mapping, obtaining the so-called *bidirectional estimation*

Intuitively, high gradient values indicate that the surface is in correspondence with the cortical-trabecular interface. While low gradient values mean that the grey-levels of the eroded and the dilated volume are similar, which, in turn, can be due to a local inaccuracy of the segmentation or to the presence of tendon insertion. Thus, to summarize, the higher the gradient value, the better the segmentation (Figs. 6.6, 6.7)

Finally, the quality of the segmentation is measured through a global analysis of the mapped gradient, where further considerations on the local mapping permit to understand the possible presence of low gradient values.

We expect that a globally good segmentation should be characterized by a higher presence of large gradient values along with small occurrences of low gradient values. Indeed, segmentation errors are associated with low gradient values since they represent a minor variation between inner and outer voxels. The presence of local errors is searched among the smallest histogram percentiles, bringing the analysis of the segmentation result as well as the comparison between different segmentation, to focus on local statistics. For these reasons, at first, the comparison of segmentation results is performed using the Cumulative Gradient Histogram (CGH), which maps the various percentile values. Then, the focus of the comparison between two segmentation results is moved to the low percentiles of the CGH. The best segmentation is represented by the CGH that presents lower values in the left part since this indicates that it has less small gradient surface points.

This application of the grey-levels mapping to unsupervised segmentation evaluation can be considered innovative since:

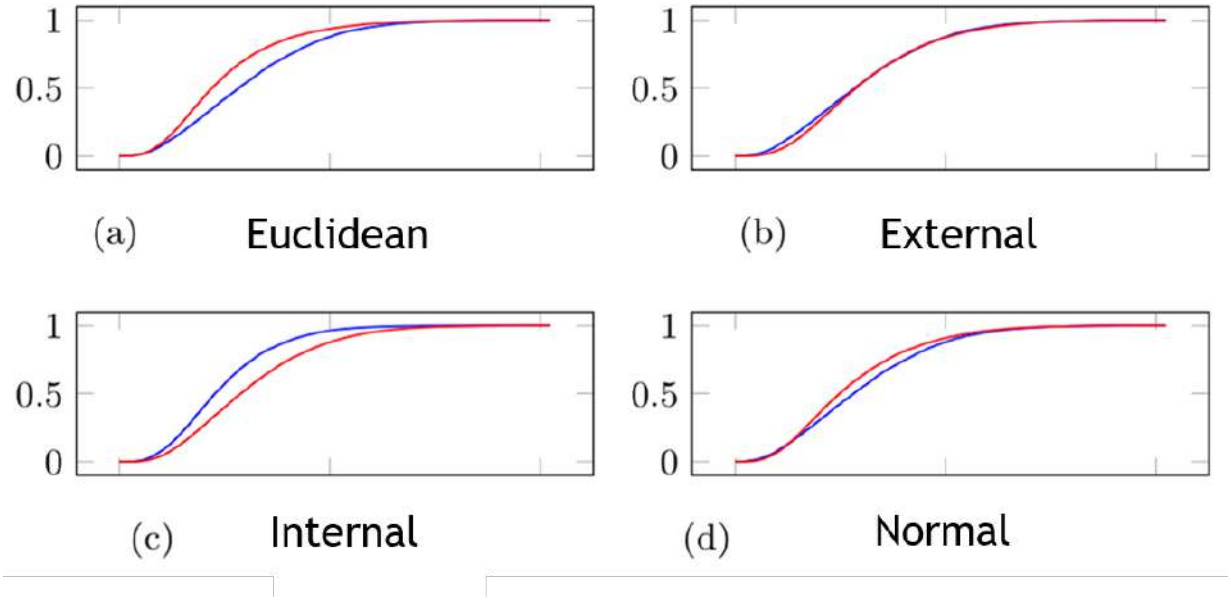

Figure 6.8: Cumulative gradient histograms (CGH) results. The blue curves refer to the automatic segmentation while the red ones to the manual segmentation. (a) Result with the Euclidean estimation, (b) with the outer, (c) with the inner, and (d) with a mapping algorithm performed considering the distance from the normal to the surface without differentiating between inside and outside.

- it results in a novel unsupervised approach;
- it presents the integration of volume and surface information into a novel framework, through the definition of the gradient measures and their mapping;
- the processing steps are conducted in both the voxel and surface levels;
- the algorithm uses 3D Mathematical Morphology (MM) with the novel scope of pre-processing step for gradient analysis;
- the regularization brought by MM pre-processing reveals able to reduce the noise effects.

Results and discussion The validation phase was conducted on the set of MRI contained in the data set described in Chapter 3. Here, the size of each slice in the coronal plane is 256×256, while moving in the longitudinal direction, the number of slices is between 90 and 120. As just reported, the CGH already provides a visual idea of the segmentation results, where a worse separation of trabecular and cortical bones are indicated by a steep trend in the left part of the CGH, since a significant quantity of the estimated gradient levels resides in lower values

(a) Euclidean estimation.

	Automatic	Manual
10^{th} Prc	592.75 ± 135.96	360.46 ± 62.39
1^{st} Qrt	830.67 ± 176.63	530.81 ± 97.81
2^{nd} Qrt	1116.71 ± 288.14	787.98 ± 159.76
3^{rd} Qrt	1489.70 ± 241.07	1118.30 ± 213.82
90^{th} Prc	1815.42 ± 269.49	1492.42 ± 258.10
95^{th} Prc	2016.89 ± 278.07	1754.30 ± 294.50

(b) Outer estimation.

	Automatic	Manual
10^{th} Prc.	596.03 ± 135.29	415.64 ± 76.33
1^{st} Qrt	834.15 ± 176.02	613.74 ± 132.82
2^{nd} Qrt	1149.36 ± 217.90	905.71 ± 210.76
3^{rd} Qrt	1491.51 ± 240.26	1263.72 ± 291.71
90^{th} Prc	1816.95 ± 269.46	1630.73 ± 350.78
95^{th} Prc	2019.24 ± 275.39	1847.36 ± 375.02

(c) Inner estimation.

	Automatic	Manual
10^{th} Prc	352.89 ± 38.97	530.20 ± 128.88
1^{st} Qrt	501.43 ± 60.29	766.28 ± 191.89
2^{nd} Qrt	709.15 ± 95.04	1091.22 ± 258.09
3^{rd} Qrt	960.99 ± 127.02	1438.37 ± 302.22
90^{th} Prc	1226.15 ± 157.20	1770.58 ± 328.17
95^{th} Prc	1407.14 ± 181.81	1971.44 ± 342.10

(d) Bidirectional estimation.

	Automatic	Manual
10^{th} Prc	585.79 ± 132.60	397.11 ± 51.94
1^{st} Qrt	824.84 ± 175.24	594.70 ± 103.46
2^{nd} Qrt	1141.48 ± 216.69	896.81 ± 177.53
3^{rd} Qrt	1484.53 ± 240.19	1274.47 ± 253.38
90^{th} Prc	1811.83 ± 268.21	1648.24 ± 300.19
95^{th} Prc	2013.31 ± 276.77	1866.19 ± 313.88

Figure 6.9: Average difference values with respect to the quartiles (Qrt) and percentiles (Prt).

(Fig. 6.8). On the contrary, a more gradual trend indicates the presence of a relevant portion of higher values, thus, better separation of trabecular and cortical bones. Quantitative results are presented in Fig. 6.9

Moreover, it is possible to notice how gradient values corresponding to gradient CGH percentiles are influenced by the adopted mapping criteria. Overall the Euclidean estimation proved to be the most suitable estimation criterion for the current purpose. Indeed, it shows the highest ratio between the gradient from the automatic segmentation and the gradient from the manual one in the lowest percentiles. This indicates that different mesh nodes present a low gradient across the surface in the manual approach result, confirming the assumption according to which the medical operators tend to include dark voxels to the ROI, as a consequence of their expertise. The automatic approach, instead, presents a high surface gradient, performing better in the cortical-trabecular interface. This is linked to the clear separation between bright and dark voxels.

In the outer estimation of the gradient, the two segmentation results tend to overlap along with the gradient values with respect to the analyzed percentiles. The explanation of this can be found in the area that the external mapping considers. Indeed, the outer estimation focuses on external voxels, thus moving away from the cortical-trabecular interface in the external direction. This results in the reduction of the bias since pathological areas, e.g. tendon insertions, are not clearly visible as moving away from the bones borders. The inner estimation, conversely from the outer

estimation, focuses on the interior voxels, thus balancing the estimation error performed by the human user.

Finally, bidirectional estimation shows a similar result to Euclidean estimation. Here, both the segmentation techniques benefit from the separate focus on external and interior voxels, thus the difference between the surface gradient is reduced. This can be reconducted to the limited number of dark voxels that are included in the manual segmentation. Nevertheless, if more dark voxels were included, then the resulting gradient estimation would be much lower, thus more distinguishable from the automatic one.

Overall, from the performed tests, the Euclidean criteria results as the most suitable to distinguish segmentation methods in their ability to identify the cortical-trabecular interface. This implies that the Euclidean criteria can differentiate a segmentation method that focuses on the grey-levels of the image (such as an automatic method), from an approach influenced by a-priori knowledge. The results presented demonstrate how the evaluation method proposed is able o show the general segmentation performance in terms of tissue interface localization. Moreover, a local evaluation on each segmentation can be performed and supported by the enhanced visualization method, localizing the regions of the single segmented structure where the borders actually coincide with the tissue interface, and those where this does not happen. This kind of analysis and evaluation, if extended to a properly wide data set, can provide information and identify the typical tissue and anatomy criticality. That information, in turn, could be exploited for the correction of automatic and semi-automatic segmentations. A further step in this direction could lead to the development of an automatic method able to benefit from the evaluation proposed in this Chapter. To this end, learning approaches, guided by the information retrieved from our unsupervised evaluation method could be considered.

Chapter 7

Contributions and Future Work

The work described in this Thesis moves towards the development of an integrated approach aimed at the combination of heterogeneous medical data. This direction of research brought to the study of different interdisciplinary fields, due to the link between all the subjects involved. A clear idea of the working principles of imaging technology is necessary to understand the information contained in the image pixels and their relevance in the clinical applications (Chapter 3). Moreover, image analysis algorithms and medical image standard must be considered in order to extract relevant regions of the image itself. Since the core of the work aims at combining image and shape analysis, Computer Graphics techniques are involved in the integration and manipulation of the 3D models with the volume images (Chapter 4). Finally, for a relevant clinical application of the developed tool both notion on the anatomy of the structures and the possible pathologies evolution must be known, in order to provide physician useful information other than an augmented visualization tool (Chapters 5, 6). Thus, the Thesis does not limit to image and shape analysis but covers image technologies' principles, image properties extraction, anatomy, and pathology notion, and graphics principles both in volume and surface rendering.

7.1 Thesis contributions to anatomical representation and clinical applications

The main contribution of this research work is the development of a mapping method able to integrate volume images and 3D PSMs (Chapter 4), in order to improve the visualization of 3D models with volumetric information for different clinical tasks (Fig 7.1). An appropriate bridge data structure, followed by a correspondence search and coloring of mesh vertices, allows us to obtain a 3D textured patient-specific model of a given anatomical district. Different mapping criteria are evaluated depending on:

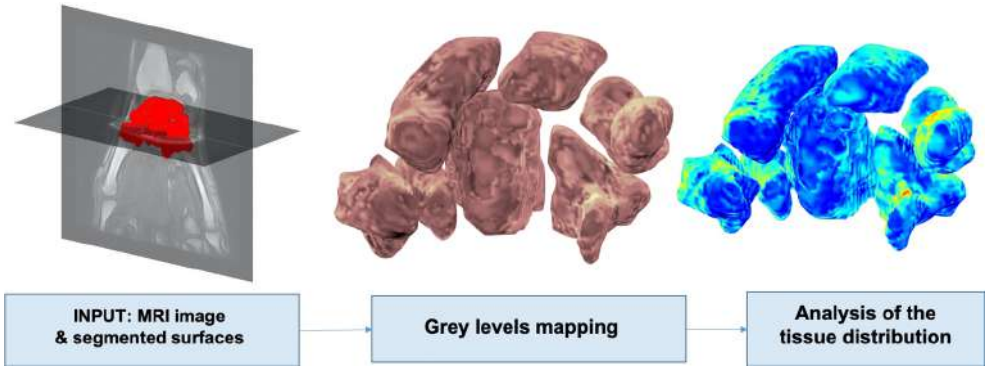

Figure 7.1: Overview of the novel approach: MR images and segmentation of the hand-wrist district, textured surfaces by mapping grey-level onto the bone surfaces, identification of tissue distribution inside the surface (darker blue correspond to darker tissues in the original volume; while brighter toward yellow and red correspond to brighter tissues in the original volume).

- **extent**: how far from the surface we analyze the distribution of grey-levels;
- **direction**: if we map gray values from inside or outside the segmented surface;
- **selection criteria**: used to define a representative grey value for the texture element.

On the basis of these characteristics, we developed 3 different mapping options: *Euclidean mapping*, *internal mapping*, and *external mapping*. The result of the mapping method is indeed a 3D shape model where the vertices of the triangulated mesh are associated with the grey-levels obtained from the analysis of surface-volume correspondences.

The proposed algorithm is simple but effectively integrates information derived from medical image analysis and 3D shape analysis. The method developed is quite general since it applies to different anatomical districts independently of the segmentation method. The proposed approach is also applicable to different imaging techniques, such as CT, and higher resolution images can only improve the promising results obtained with low-field MRIs. The volume information can be integrated easily in different shape analysis applications, which take into consideration not only the morphology of the input shape but also the real context in which it is inserted. Often, in the medical field, the possibility to integrate a tool with an already existing workflow is the key to the success of the tool itself, which brings to possible actual application in clinical practice.

We identified the medical problems that most benefit from the use of the proposed approach and tried to find a way to support those applications with the information provided by the mapping method. Specifically, we compared and merged these pieces of information with the ones provided by shape analysis. We have demonstrated that, given the 3D model resulting from the grey-levels mapping, it is possible to execute comparative evaluations, between the results obtained from the shape analysis and the ones obtained from the texture evaluation (Chapter 5).

Moreover, the shape analysis results have been useful to pursue a more focused analysis of the texture information, as happens in the characterization of the articulation regions. Shape descriptors that aim to semantically segment the shape, are improved and supported by the texture analysis. This means that the mapping result is able to perform not only a general analysis but also local discrimination of tissues and anatomical features. Furthermore, we also demonstrated how a real integration of information can bring more homogeneous overall results, with a clearer visualization interface for physicians.

The application of the mapping method can bring information also on the pre-processing of the image, this means that the method can bring further information about the patient situation and can be thought of as a means for the evaluation of the image processing performed before the surface extraction (Fig. 7.2) (Chapter 6).

Articulation region analysis Since the carpus is one of the most complicated articulation districts in the human body, a good characterization of the various articulation region in a patient-specific fashion is relevant for the analysis of the subject. To describe those areas, we combined the information provided by the shape analysis descriptor with the ones provided by the texture mapped on the 3D surface (Chapter 5). The shape descriptor chosen for this purpose was the Shadow map, which captures not only information about the shape of the individual bones, but also about their spatial arrangement in the whole district. Through the Shadow map, we identified the articulation regions on each bone, and then we performed a comparison of the texture in the identified regions (with respect to the non-articulation areas). From a statistical analysis, we found that the texture in the articulation regions is statistically different from the region not involved in the articulation.

Fllow-up analysis In the treatment of degenerative rheumatoid diseases, for physicians, it is crucial to evaluate the progression of the pathology over time. To support this kind of evaluation, we focused on the identification of erosion sites on bones, merging geometrical analysis with the information provided by texture changes in time (Chapter 5). Shape analysis techniques can indicate where on the surface, a relevant change in morphology appears. An analysis of the grey-levels, instead, indicates which kind of tissue presented alteration, without the need of referring back to the whole volume image. First, we registered the bones at baseline time, with the ones at follow up time (barycenter translation + ICP). Then, we computed the Hausdorff distance between the bones at baseline time and at follow-up time, identifying which bones could present an erosion site (the higher the distance, the more probable is the presence of erosion). From the distance distribution, we highlighted the region on the bones where the erosion is placed. Comparing the distance distribution with the difference of the texture at baseline and follow-up time we found that the texture difference is higher in the same regions identified by the distance distribution. Moreover, the texture difference does not present high values in those regions where the distance distribution provides misleading information due to inaccuracies of

the registration process. For this reason, we further performed a comparison between different approaches: geometry-based approach, texture-based approach, and integration of geometric and texture information.

Ligament insertions identification We performed a preliminary study on the identification of the ligament insertion locations from patient data. Indeed, ligament insertion analysis is important for early diagnosis and classification of the pathology. Since the insertion is not strictly linked to a region with particular shape features, we focused on the analysis of the texture histogram, identifying a patient-specific and bone-specific range of grey-levels that could correspond to a ligament insertion. We based this range on anatomical and tissue composition reasons. The results look promising since the ligament insertions indicated by the anatomical atlas find a correspondence in our method on real patient data (Chapter 5).

Segmentation analysis In medicine, the segmentation process is a challenging task to be performed both if conducted automatically or manually. One main problem is the operator dependency when it is performed manually. The second issue is the absence of a real gold standard for the evaluation of segmentation performed automatically. Thus, an analysis of the results of the segmentation, based on the analysis of the textured shape model, provides objective information on the tissues included and excluded from the shape. To study the segmented objects, we compared the grey-levels of the voxels outside and inside the surface. The comparison consisted of subtracting, for each surface vertex, the value of the external mapping to the internal mapping. It results that if the edge of the bone is placed between the cortical and the bone marrow tissue, then the internal mapping should be brighter than the external mapping, leading to a positive value. If the edge locates outside the cortical tissue, then darker internal mapping grey-levels will make the difference negative (Chapter 6).

Segmentation evaluation As regards the segmentation evaluation, we are carrying on a collaboration with Prof. Silvana DellePiane and Marco Trombini (Ph.D. student) at UNIGE-DITEN. We developed a method to evaluate and compare different segmentation results in an unsupervised fashion. In this way, the absence of an objective gold standard can be overcome. The proposed approach is based on the integration of volume-based and surface-based analysis and is tested on Magnetic Resonance volumes of the wrist district. We combined the computation of the texture gradient with volume image pre-processing (dilation and erosion) in order to provide an analysis of the quality of the segmentation. Starting from the segmented volume of a bone, the corresponding surface is extracted and its quality is estimated based on gradient properties, measured in the volume, and mapped onto the surface. Various mapping techniques along with morphological operators are proposed in order to reduce the error in the gradient estimation, and the segmentation is evaluated through a statistical analysis of the mapped gradient. We tested the result of this evaluation method on the data set (presenting manual segmentation) and on

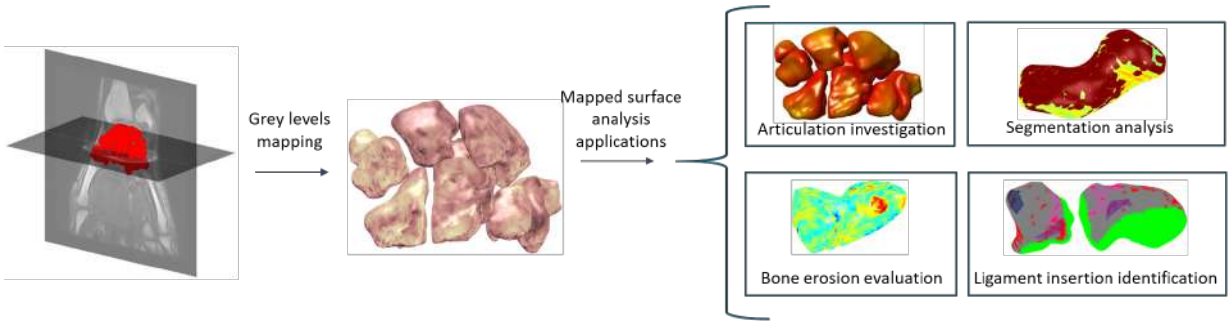

Figure 7.2: Overview of the developed framework.

the segmentation performed by the automatic method developed by Prof. Dellepiane and Marco Trombini at UNIGE. Our evaluation algorithm was able to distinguish between different segmentation methods and to provide an objective analysis of the results (Chapter 6).

All the information retrieved from the analysis of the 3D augmented PSMs have been discussed with an expert rheumatologist and are known problems of everyday medical practice. The possibility for a physician to have all the information in a unique visualization is extremely useful, not only for a 3D better visualization given by the 3D shape model but also for a time-saving point of view. Indeed, the grey-levels mapped on the surface automatically focalize the attention of the expert on the relevant areas of the volume data. With a 3D volume image, indeed, the mole of information that a radiologist has to examine is way higher, and manually evaluating every part of the image can be time-consuming and error-prone. The mapping algorithm, as a visualization tool, permits to avoid this situation by providing the volume information in a controlled neighborhood of the bone surface.

7.2 Research and development directions

Segmentation method development On the basis of the work developed with the University of Genova the idea is to define a novel segmentation method for low-field MR images and for the local correction/improvement of a given segmentation. The good results obtained from the evaluation method described in Chapter 6 are promising premisses for the development of such an automatic segmentation method or, at least, to a reliable tool for the adjustment of automatically preformed segmentations.

Clinical validation Even if the statistical analysis performed in this work and explained in Chapters 5 and 6, supported the expectations we had from our method, a wider clinical vali-

dation could be an ulterior support to our conclusions. Indeed, this research could benefit from clinical evaluation of the results, not only for the carpal district but also for other musculoskeletal structures. This implies the presence of a wider data set that, in medicine, is not as straightforward as in other fields. A questionnaire concerning the result obtained by our work and other potential use of the visualization and evaluation tool could support the clinical validation. Moreover, this questionnaire could focus also on other needs felt by radiologists that didn't come out in the early stages of this research.

Automatization of the follow-up approach In Chapter 5 we presented a comparison of different approaches to support the medical follow-up analysis in radiology, with a special focus on erosion development in rheumatic diseases. In that scenario, the presence of false positives presents to the physician a worsened situation and, thus, a higher level of bone degeneration, with respect to reality. Whereas, the presence of false-negatives induces an underestimation of pathology progression gravity. Indeed, the presence of false-positives or false-negative could alter the result of the therapy performance analysis, thus the identification of the trade-off between the two is important.

Even if the geometry and texture integration proposed already supports the analysis of follow-up as enhanced visualization methods, future work will be focused on the improvement of the integration method toward a fully automatic approach with a quantitative measure of the erosion. Since our study is based on the presence of two exams: one at baseline and one at follow-up, the automatizing process would be easier in presence of more than one follow-up exams, especially for a comparison thought to be extremely patient-specific. A higher number of exams, other than helping the automatic adjustment of the ϵ parameter, could allow a more complete clinical validation. Moreover, testing different registration methods for the geometry-based analysis could improve the results obtained with higher accuracy.

Image fusion-extention Since the method developed can be applied to different imaging technologies and given the progress of medical imaging toward image fusion techniques, a valid perspective could be to proceed in this direction. With this in mind, I started a 2-years research fellowship at CNR-IMATI and in collaboration with Esaote SPA on a research project focused on image fusion, which will be a good opportunity to expand the work described in this Thesis. The title of the research is, "Image-fusion study and development of innovative approaches to fusion, analysis, and visualization of MRI low field images and ultrasound for the improvement of musculoskeletal pathologies diagnosis". Thus, it will open the opportunity to extend the application of the method developed with this research to other kinds of imaging techniques. Moreover, it will be an occasion, not only to apply our method to various data types but also to evaluate its performances and possible development in different scenarios. Indeed, the possibility to explore a volumetric image with the guidance of a 3D surface model could be interesting in many medical branches.

Bibliography

[AB94] Rolf Adams and Leanne Bischof. Seeded region growing. *IEEE Transactions on pattern analysis and machine intelligence*, 16(6):641–647, 1994.

[ABM+06] Marco Attene, Silvia Biasotti, Michela Mortara, Giuseppe Patanè, Michela Spagnuolo, and Bianca Falcidieno. Computational methods for understanding 3d shapes. *Computers & Graphics*, 30(3):323–333, 2006.

[ADD+14] John Apostolakos, Thomas JS Durant, Corey R Dwyer, Ryan P Russell, Jeffrey H Weinreb, Farhang Alaee, Knut Beitzel, Mary Beth McCarthy, Mark P Cote, and Augustus D Mazzocca. The enthesis: a review of the tendon-to-bone insertion. *Muscles, ligaments and tendons journal*, 4(3):333, 2014.

[APAC17] Simon Andermatt, Simon Pezold, Michael Amann, and Philippe C Cattin. Multi-dimensional gated recurrent units for automated anatomical landmark localization. *arXiv preprint arXiv:1708.02766*, 2017.

[ARN+11] Ceyhun Burak Akgül, Daniel L Rubin, Sandy Napel, Christopher F Beaulieu, Hayit Greenspan, and Burak Acar. Content-based image retrieval in radiology: current status and future directions. *Journal of digital imaging*, 24(2):208–222, 2011.

[BAC+16] Imon Banerjee, Asan Agibetov, Chiara Eva Catalano, Giuseppe Patané, and Michela Spagnuolo. Semantics-driven annotation of patient-specific 3d data: a step to assist diagnosis and treatment of rheumatoid arthritis. *The visual computer*, 32:1337–1349, 2016.

[Ban16] Imon Banerjee. *Integration of Shape Analysis and Knowledge Techniques for the Semantic Annotation of Patient-Specific 3D Data*. PhD thesis, 2016.

[BB13] Vincent Barra and Silvia Biasotti. 3D shape retrieval using kernels on extended reeb graphs. *Pattern Recognition*, 46(11):2985–2999, 2013.

[BBL+17] Michael M. Bronstein, Joan Bruna, Yann LeCun, Arthur Szlam, and Pierre Vandergheynst. Geometric deep learning: Going beyond euclidean data. *IEEE Signal Process. Mag.*, 34(4):18–42, 2017.

[BBS+02] M Backhaus, GR Burmester, D Sandrock, D Loreck, D Hess, A Scholz, S Blind, B Hamm, and M Bollow. Prospective two year follow up study comparing novel and conventional imaging procedures in patients with arthritic finger joints. *Annals of the Rheumatic Diseases*, 61(10):895–904, 2002.

[BCA+16] S. Biasotti, A. Cerri, M. Aono, A. Ben Hamza, V. Garro, A. Giachetti, D. Giorgi, A. Godil, C. Li, C. Sanada, M. Spagnuolo, A. Tatsuma, and S. Velasco-Forero. Retrieval and classification methods for textured 3D models: a comparative study. *The Visual Computer*, 32(2):217–241, 2016.

[BCBB16] Silvia Biasotti, Andrea Cerri, Alex Bronstein, and Michael Bronstein. Recent trends, applications, and perspectives in 3d shape similarity assessment. In *Computer Graphics Forum*, volume 35, pages 87–119. Wiley Online Library, 2016.

[BCPS16] Imon Banerjee, Chiara Eva Catalano, Giuseppe Patané, and Michela Spagnuolo. Semantic annotation of 3d anatomical models to support diagnosis and follow-up analysis of musculoskeletal pathologies. *International journal of computer assisted radiology and surgery*, 11(5):707–720, 2016.

[BCRS14] Imon Banerjee, Chiara Eva Catalano, Francesco Robbiano, and Michela Spagnuolo. Accessing and representing knowledge in the medical field: visual and lexical modalities. In *3D Multiscale Physiological Human*, pages 297–316. Springer, 2014.

[BDF+08] S. Biasotti, L. De Floriani, B. Falcidieno, P. Frosini, D. Giorgi, C. Landi, L. Papaleo, and M. Spagnuolo. Describing shapes by geometrical-topological properties of real functions. *ACM Comput. Surv.*, 40(4):1–87, 2008.

[BFF+07] S. Biasotti, B. Falcidieno, P. Frosini, D. Giorgi, C. Landi, G. Patanè, and M. Spagnuolo. 3D shape description and matching based on properties of real functions. In *Eurographics 2007, Tutorial Notes*, pages 949–998, 2007.

[BGH+11] Leonard J Bond, Jeffrey W Griffin, RV Harris, Kayte M Denslow, and Traci L Moran. Evaluation of non-nuclear techniques for well logging. Technical report, Pacific Northwest National Lab.(PNNL), Richland, WA (United States), 2011.

[BGSF08] S. Biasotti, D. Giorgi, M. Spagnuolo, and B. Falcidieno. Reeb graphs for shape analysis and applications. *Theoretical Computer Science*, 392(1–3):5–22, 2008. doi: 10.1016/j.tcs.2007.10.018.

[BHR+15] Marco Boegel, Philip Hoelter, Thomas Redel, Andreas Maier, Joachim Hornegger, and Arnd Doerfler. A fully-automatic locally adaptive thresholding algorithm for blood vessel segmentation in 3d digital subtraction angiography. In *2015 37th Annual International Conference of the IEEE Engineering in Medicine and Biology Society (EMBC)*, pages 2006–2009. IEEE, 2015.

[BKS+05] B. Bustos, D. A. Keim, D. Saupe, T. Schreck, and D. V. Vranić. Feature-based similarity search in 3D object databases. *ACM Computing Surveys*, 37(4):345–387, December 2005.

[BM92] Paul J Besl and Neil D McKay. Method for registration of 3-d shapes. In *Sensor fusion IV: control paradigms and data structures*, volume 1611, pages 586–606. International Society for Optics and Photonics, 1992.

[BM01] Micheal Benjamin and Dennis McGonagle. The anatomical basis for disease localisation in seronegative spondyloarthropathy at entheses and related sites. *Journal of anatomy*, 199(5):503–526, 2001.

[BMM+15] D. Boscaini, J. Masci, S. Melzi, M. M. Bronstein, U. Castellani, and P. Vandergheynst. Learning class-specific descriptors for deformable shapes using localized spectral convolutional networks. *Comput. Graph. Forum*, (35), 2015.

[BPF+19] Imon Banerjee, Martina Paccini, Enrico Ferrari, Chiara Eva Catalano, Silvia Biasotti, and Michela Spagnuolo. Feature-based characterisation of patient-specific 3d anatomical models. In *STAG*, pages 41–50, 2019.

[BPK+07] Mario Botsch, Mark Pauly, Leif Kobbelt, Pierre Alliez, Bruno Lévy, Stephan Bischoff, and Christian Röossl. Geometric modeling based on polygonal meshes. 2007.

[BTR+06] M Benjamin, H Toumi, JR Ralphs, G Bydder, TM Best, and S Milz. Where tendons and ligaments meet bone: attachment sites ('entheses') in relation to exercise and/or mechanical load. *Journal of anatomy*, 208(4):471–490, 2006.

[BTZ+15] Francesca Barbieri, Veronica Tomatis, Giuseppe Zampogna, Elena Aleo, Valentina Prono, Stefania Migone, Patrizia Parascandolo, Lorenzo Cesario, Gianni Viano, and Marco Amedeo Cimmino. An mri study of bone erosions healing in the wrist and metacarpophalangeal joints of patients with rheumatoid arthritis. In *International Conference on Image Analysis and Processing*, pages 129–134. Springer, 2015.

[CDV12] Giuseppe Coppini, Stefano Diciotti, and Guido Valli. *Bioimmagini*. Pàtron, 2012.

[Cha16] Ashutosh Kumar Chaubey. Comparison of the local and global thresholding methods in image segmentation. *World Journal of Research and Review*, 2(1), 2016.

[CHC+13] Stuart Currie, Nigel Hoggard, Ian J Craven, Marios Hadjivassiliou, and Iain D Wilkinson. Understanding mri: basic mr physics for physicians. *Postgraduate medical journal*, 89(1050):209–223, 2013.

[CK16] Mahipal Singh Choudhry and Rajiv Kapoor. Performance analysis of fuzzy c-means clustering methods for mri image segmentation. *Procedia Computer Science*, 89:749–758, 2016.

[CKS97] Vicent Caselles, Ron Kimmel, and Guillermo Sapiro. Geodesic active contours. *International journal of computer vision*, 22(1):61–79, 1997.

[CMS12] D. Ciresan, U. Meier, and J. Schmidhuber. Multi-column deep neural networks for image classification. In *Computer Vision and Pattern Recognition, IEEE Conference on*, pages 3642–3649, 2012.

[CRC+02] J. Corney, H. Rea, D. Clark, J. Pritchard, M. Breaks, and R. Macleod. Coarse filters for shape matching. *IEEE Computer Graphics and Applications*, 22(3):65–74, May 2002.

[dARF+17] Diogo F de Almeida, Rui B Ruben, João Folgado, Paulo R Fernandes, João Gamelas, Benedict Verhegghe, and Matthieu De Beule. Automated femoral landmark extraction for optimal prosthesis placement in total hip arthroplasty. *International journal for numerical methods in biomedical engineering*, 33(8):e2844, 2017.

[DCdBdMW04] Mathieu De Craene, Aloys du Bois d'Aische, Benoît Macq, and Simon K Warfield. Multi-subject registration for unbiased statistical atlas construction. In *International Conference on Medical Image Computing and Computer-Assisted Intervention*, pages 655–662. Springer, 2004.

[DDM+19] Alper H Duran, Munevver N Duran, Irfan Masood, Lynsey M Maciolek, and Huda Hussain. The additional diagnostic value of the three-dimensional volume rendering imaging in routine radiology practice. *Cureus*, 11(9), 2019.

[DEH+08] Uffe Møller Døhn, Bo J Ejbjerg, Maria Hasselquist, Eva Narvestad, Jakob Møller, Henrik S Thomsen, and Mikkel Østergaard. Detection of bone erosions in rheumatoid arthritis wrist joints with magnetic resonance imaging, computed tomography and radiography. *Arthritis research & therapy*, 10(1):R25, 2008.

[Dic00] Amerircan Heritage Dictionary. The american heritage® dictionary of the english language. *Answers. com*, 2000.

[Die] Dieletric effect questions and answers in mri. https://mriquestions.com/dielectric-effect.html. (Accessed on 10/02/2020).

[EHPP04] J Ehrhardt, H Handels, W Plötz, and SJ Pöppl. Atlas-based recognition of anatomical structures and landmarks and the automatic computation of orthopedic parameters. *Methods of information in medicine*, 43(04):391–397, 2004.

[EMT02] Mark Everingham, Henk Muller, and Barry Thomas. Evaluating image segmentation algorithms using the pareto front. In *European Conference on Computer Vision*, pages 34–48. Springer, 2002.

[EWvK+16] Mustafa Elattar, Esther Wiegerinck, Floortje van Kesteren, Lucile Dubois, Nils Planken, Ed Vanbavel, Jan Baan, and Henk Marquering. Automatic aortic root landmark detection in cta images for preprocedural planning of transcatheter aortic valve implantation. *The international journal of cardiovascular imaging*, 32(3):501–511, 2016.

[FKS+18] Camille P Figueiredo, Arnd Kleyer, David Simon, Fabian Stemmler, Isabelle d'Oliveira, Anja Weissenfels, Oleg Museyko, Andreas Friedberger, Axel J Hueber, Judith Haschka, et al. Methods for segmentation of rheumatoid arthritis bone erosions in high-resolution peripheral quantitative computed tomography (hr-pqct). In *Seminars in arthritis and rheumatism*, volume 47, pages 611–618. Elsevier, 2018.

[FM16] Maedeh Sadat Fasihi and Wasfy B Mikhael. Overview of current biomedical image segmentation methods. In *2016 International Conference on Computational Science and Computational Intelligence (CSCI)*, pages 803–808. IEEE, 2016.

[FS98] B. Falcidieno and M. Spagnuolo. A shape abstraction paradigm for modeling geometry and semantics. In *Proceedings of the Computer Graphics International 1998*, CGI '98, pages 646–656, Washington, DC, USA, 1998. IEEE Computer Society.

[GD15] Laura Gemme and Silvana Dellepiane. A new graph-based method for automatic segmentation. In *International Conference on Image Analysis and Processing*, pages 601–611. Springer, 2015.

[GG84] Stuart Geman and Donald Geman. Stochastic relaxation, gibbs distributions, and the bayesian restoration of images. *IEEE Transactions on pattern analysis and machine intelligence*, (6):721–741, 1984.

[GGM+16] Florin C Ghesu, Bogdan Georgescu, Tommaso Mansi, Dominik Neumann, Joachim Hornegger, and Dorin Comaniciu. An artificial agent for anatomical landmark detection in medical images. In *International conference on medical image computing and computer-assisted intervention*, pages 229–237. Springer, 2016.

[Gib08] Bernard Gibaud. The dicom standard: a brief overview. In *Molecular imaging: computer reconstruction and practice*, pages 229–238. Springer, 2008.

[GKT+14] Kirill Gromov, Mounim Korchi, Morten G Thomsen, Henrik Husted, and Anders Troelsen. What is the optimal alignment of the tibial and femoral components in knee arthroplasty? an overview of the literature. *Acta orthopaedica*, 85(5):480–487, 2014.

[GPM16] Shivanand S Gornale, Pooja U Patravali, and Ramesh R Manza. A survey on exploration and classification of osteoarthritis using image processing techniques. *International Journal of Scientific & Engineering Research*, 7(6):334–355, 2016.

[GTC+15] Vijay PB Grover, Joshua M Tognarelli, Mary ME Crossey, I Jane Cox, Simon D Taylor-Robinson, and Mark JW McPhail. Magnetic resonance imaging: principles and techniques: lessons for clinicians. *Journal of clinical and experimental hepatology*, 5(3):246–255, 2015.

[GWE04] Rafael C Gonzalez, Richard Eugene Woods, and Steven L Eddins. *Digital image processing using MATLAB*. Pearson Education India, 2004.

[HBGD18] Che-Wei Hu, Arnold Baca, Martin Groeber, and Peter Dabnichki. Geometrical model for characterization of foot deformity using 3d imaging. *IFAC-PapersOnLine*, 51(2):373–378, 2018.

[HFL12] R. Hu, L. Fan, and L. Liu. Co-segmentation of 3D shapes via subspace clustering. In *SGP'12: Proceedings of the 2012 Eurographics Symposium on Geometry Processing*, pages 1703–1713, 2012.

[HJHK19] Mohammad Hesam Hesamian, Wenjing Jia, Xiangjian He, and Paul Kennedy. Deep learning techniques for medical image segmentation: achievements and challenges. *Journal of digital imaging*, 32(4):582–596, 2019.

[HM09] Tobias Heimann and Hans-Peter Meinzer. Statistical shape models for 3d medical image segmentation: a review. *Medical image analysis*, 13(4):543–563, 2009.

[HS85] Robert M Haralick and Linda G Shapiro. Image segmentation techniques. *Computer vision, graphics, and image processing*, 29(1):100–132, 1985.

[HS97] Donald D Hoffman and Manish Singh. Salience of visual parts. *Cognition*, 63(1):29–78, 1997.

[HSKK01] M. Hilaga, Y. Shinagawa, T. Kohmura, and T. L. Kunii. Topology matching for fully automatic similarity estimation of 3D shapes. In *Conference on Computer Graphics and Interactive Techniques (SIGGRAPH)*, pages 203–212. ACM, 2001.

[HSS+13] S.-S. Huang, A. Shamir, C.-H. Shen, H. Zhang, A. Sheffer, S.-M. Hu, and D. Cohen-Or. Qualitative organization of collections of shapes via quartet analysis. *ACM Transactions on Graphics*, 32(4):71:1–71:10, July 2013.

[HVvdH+15] Yinghe Huo, Koen L Vincken, Désirée van der Heijde, Maria JH De Hair, Floris P Lafeber, and Max A Viergever. Automatic quantification of radiographic finger joint space width of patients with early rheumatoid arthritis. *IEEE Transactions on Biomedical Engineering*, 63(10):2177–2186, 2015.

[HWG14] Qixing Huang, Fan Wang, and Leonidas Guibas. Functional map networks for analyzing and exploring large shape collections. *ACM T. Graphic.*, 33(4):36:1–36:11, 2014.

[HZG+12] Qi-Xing Huang, Guo-Xin Zhang, Lin Gao, Shi-Min Hu, Adrian Butscher, and Leonidas Guibas. An optimization approach for extracting and encoding consistent maps in a shape collection. *ACM T. Graphic.*, 31(6):167:1–167:11, 2012.

[JKP+19] Yeseul Jo, JeongJae Kim, Chul Hwan Park, Jae Wook Lee, Jee Hye Hur, Dong Hyun Yang, Bae Young Lee, Dong Jin Im, Su Jin Hong, Eun Young Kim, et al. Guideline for cardiovascular magnetic resonance imaging from the korean society of cardiovascular imaging—part 1: standardized protocol. *Korean journal of radiology*, 20(9):1313–1333, 2019.

[JLBC15] Anand A Joshi, Richard M Leahy, Ramsey D Badawi, and Abhijit J Chaudhari. Registration-based morphometry for shape analysis of the bones of the human wrist. *IEEE Transactions on Medical Imaging*, 35(2):416–426, 2015.

[Kau96] Arie E Kaufman. Volume visualization. *ACM Computing Surveys (CSUR)*, 28(1):165–167, 1996.

[KBB+13] A. Kovnatsky, M. M. Bronstein, A. M. Bronstein, K. Glashoff, and R. Kimmel. Coupled quasi-harmonic bases. *Computer Graphics Forum*, 32(2pt4):439–448, 2013.

[KEA+18] Gurjit S Kaeley, Lihi Eder, Sibel Z Aydin, Marwin Gutierrez, and Catherine Bakewell. Enthesitis: a hallmark of psoriatic arthritis. In *Seminars in arthritis and rheumatism*, volume 48, pages 35–43. Elsevier, 2018.

[KHS10] E. Kalogerakis, A. Hertzmann, and K. Singh. Learning 3D mesh segmentation and labeling. *ACM Trans. Graph.*, 29:102:1–102:12, July 2010.

[Kle15] Hans-Martin Klein. *clinical low field strength magnetic resonance imaging: a practical guide to accessible MRI*. Springer, 2015.

[KLM+12] Vladimir G. Kim, Wilmot Li, Niloy J. Mitra, Stephen DiVerdi, and Thomas Funkhouser. Exploring collections of 3D models using fuzzy correspondences. *ACM T. Graphic.*, 31(4):54:1–54:11, 2012.

[KLM+13] Vladimir G. Kim, Wilmot Li, Niloy J. Mitra, Siddhartha Chaudhuri, Stephen DiVerdi, and Thomas Funkhouser. Learning part-based templates from large collections of 3d shapes. *ACM T. Graphic.*, 32(4):70:1–70:12, 2013.

[KvD92] Jan J Koenderink and Andrea J van Doorn. Surface shape and curvature scales. *Image and vision computing*, 10(8):557–564, 1992.

[KWT88] Michael Kass, Andrew Witkin, and Demetri Terzopoulos. Snakes: Active contour models. *International journal of computer vision*, 1(4):321–331, 1988.

[LC87] William E Lorensen and Harvey E Cline. Marching cubes: A high resolution 3d surface construction algorithm. *ACM siggraph computer graphics*, 21(4):163–169, 1987.

[Lev00] Michael Emmanuel Leventon. *Statistical models in medical image analysis*. PhD thesis, Massachusetts Institute of Technology, 2000.

[LHS+06] Kelvin K Leung, Mark Holden, Nadeem Saeed, Keith J Brooks, Jacky B Buckton, Ann A Williams, Simon P Campbell, Kumar Changani, David G Reid, Yong Zhao, et al. Automatic quantification of changes in bone in serial mr images of joints. *IEEE Transactions on Medical Imaging*, 25(12):1617–1626, 2006.

[LKB+17] Geert Litjens, Thijs Kooi, Babak Ehteshami Bejnordi, Arnaud Arindra Adiyoso Setio, Francesco Ciompi, Mohsen Ghafoorian, Jeroen Awm Van Der Laak, Bram Van Ginneken, and Clara I Sánchez. A survey on deep learning in medical image analysis. *Medical image analysis*, 42:60–88, 2017.

[LKD04] Xiang Liu, Wangdo Kim, and Burkhard Drerup. 3d characterization and localization of anatomical landmarks of the foot by fastscan. *Real-time imaging*, 10(4):217–228, 2004.

[LMS13] Hamid Laga, Michela Mortara, and Michela Spagnuolo. Geometry and context for semantic correspondences and functionality recognition in man-made 3D shapes. *ACM T. Graphic.*, 32(5):150:1–150:16, October 2013.

[LPBK08] Georg Langs, Philipp Peloschek, Horst Bischof, and Franz Kainberger. Automatic quantification of joint space narrowing and erosions in rheumatoid arthritis. *IEEE Transactions on Medical Imaging*, 28(1):151–164, 2008.

[LQZ15] Hao Liu, Hongbo Qian, and Jianning Zhao. Automatic extraction of 3d anatomical feature curves of hip bone models reconstructed from ct images. *Bio-Medical Materials and Engineering*, 26(s1):S1297–S1314, 2015.

[LYV+12] Xiaojuan Li, Andrew Yu, Warapat Virayavanich, Susan M Noworolski, Thomas M Link, and John Imboden. Quantitative characterization of bone marrow edema pattern in rheumatoid arthritis using 3 tesla mri. *Journal of Magnetic Resonance Imaging*, 35(1):211–217, 2012.

[Maga] Magnetic dipole moment questions and answers in mri. `https://mriquestions.com/magnetic-dipole-moment.html`. (Accessed on 10/02/2020).

[Magb] Magnetic resonance imaging (mri). `https://www.nibib.nih.gov/science-education/science-topics/magnetic-resonance-imaging-mri#:~:text=MRIs%20employ%20powerful%20magnets%20which,pull%20of%20the%20magnetic%20field`. (Accessed on 10/02/2020).

[MB05] Tom McReynolds and David Blythe. *Advanced graphics programming using OpenGL*. Elsevier, 2005.

[MBP+20] Shervin Minaee, Yuri Boykov, Fatih Porikli, Antonio Plaza, Nasser Kehtarnavaz, and Demetri Terzopoulos. Image segmentation using deep learning: A survey. *arXiv preprint arXiv:2001.05566*, 2020.

[MD03] Carsten Moenning and Neil A Dodgson. Fast marching farthest point sampling. In *Proc. EUROGRAPHICS*, 2003.

[MHT+18] Seiichi Murakami, Kazuhiro Hatano, JooKooi Tan, Hyoungseop Kim, and Takatoshi Aoki. Automatic identification of bone erosions in rheumatoid arthritis from hand radiographs based on deep convolutional neural network. *Multimedia Tools and Applications*, 77(9):10921–10937, 2018.

[ML17] Giulia Mantovani and Mario Lamontagne. How different marker sets affect joint angles in inverse kinematics framework. *Journal of biomechanical engineering*, 139(4), 2017.

[MMPL07] Nicholas A Morton, Lorin P Maletsky, Saikat Pal, and Peter J Laz. Effect of variability in anatomical landmark location on knee kinematic description. *Journal of Orthopaedic Research*, 25(9):1221–1230, 2007.

[MRB+16] Jonathan Masci, Emanuele Rodolà, Davide Boscaini, Michael M. Bronstein, and Hao Li. Geometric deep learning. In Niloy J. Mitra, editor, *SIGGRAPH ASIA 2016, Macao, December 5-8, 2016 - Courses*, pages 1:1–1:50. ACM, 2016.

[MSZ11] Mostafa Jabarouti Moghaddam and Hamid Soltanian-Zadeh. Medical image segmentation using artificial neural networks. *Artificial Neural Networks-Methodological Advances and Biomedical Applications*, pages 121–138, 2011.

[NK10] Maxwell Lewis Neal and Roy Kerckhoffs. Current progress in patient-specific modeling. *Briefings in bioinformatics*, 11(1):111–126, 2010.

[ØEM+] Mikkel Østergaard, J Edmonds, F McQueen, C Peterfy, M Lassere, B Ejbjerg, P Bird, P Emery, H Genant, and P Conaghan. *Annals of the rheumatic diseases*, (suppl 1):i3–i7.

[OLGM11] Maks Ovsjanikov, Wilmot Li, Leonidas Guibas, and Niloy J. Mitra. Exploration of continuous variability in collections of 3d shapes. *ACM T. Graphic.*, 30(4):33:1–33:10, 2011.

[Ots79] Nobuyuki Otsu. A threshold selection method from gray-level histograms. *IEEE transactions on systems, man, and cybernetics*, 9(1):62–66, 1979.

[PA06] Mihail Popescu and Gerald Arthur. Ontoquest: A physician decision support system based on ontological queries of the hospital database. In *AMIA Annual Symposium Proceedings*, volume 2006, page 639. American Medical Informatics Association, 2006.

[PB13] Bernhard Preim and Charl P Botha. *Visual computing for medicine: theory, algorithms, and applications*. Newnes, 2013.

[PBJ+09] Olivier Palombi, Guillaume Bousquet, David Jospin, Sahar Hassan, Lionel Reveret, and François Faure. My corporis fabrica: a unified ontological, geometrical and mechanical view of human anatomy. In *3D Physiological Human Workshop*, pages 209–219. Springer, 2009.

[PCVV14] Patrizia Parascandolo, Lorenzo Cesario, Loris Vosilla, and Gianni Viano. Computer aided diagnosis: state-of-the-art and application to musculoskeletal diseases. In *3D Multiscale Physiological Human*, pages 277–296. Springer, 2014.

[PGAN16] Karen Panetta, Chen Gao, Sos Agaian, and Shahan Nercessian. A new reference-based edge map quality measure. *IEEE Transactions on Systems, Man, and Cybernetics: Systems*, 46(11):1505–1517, 2016.

[PHAN06] KN Bhanu Prakash, Qingmao Hu, Aamer Aziz, and Wieslaw L Nowinski. Rapid and automatic localization of the anterior and posterior commissure point landmarks in mr volumetric neuroimages1. *Academic radiology*, 13(1):36–54, 2006.

[PP93] Ulrich Pinkall and Konrad Polthier. Computing discrete minimal surfaces and their conjugates. *Experimental mathematics*, 2(1):15–36, 1993.

[PS06] Konrad Polthier and Markus Schmies. Straightest geodesics on polyhedral surfaces. In *ACM SIGGRAPH 2006 Courses*, SIGGRAPH '06, pages 30–38, New York, NY, USA, 2006. ACM.

[Rid10] John P Ridgway. Cardiovascular magnetic resonance physics for clinicians: part i. *Journal of cardiovascular magnetic resonance*, 12(1):71, 2010.

[Rid15] John P Ridgway. Relaxation times, gradient echoes and spin echoes. In *Cardiovascular MR Manual*, pages 31–41. Springer, 2015.

[ROA+13] Raif M. Rustamov, Maks Ovsjanikov, Omri Azencot, Mirela Ben-Chen, Frédéric Chazal, and Leonidas Guibas. Map-based exploration of intrinsic shape differences and variability. *ACM T. Graphic.*, 32(4):72:1–72:12, 2013.

[RRSD19] Janick Rohrbach, Tobias Reinhard, Beate Sick, and Oliver Dürr. Bone erosion scoring for rheumatoid arthritis with deep convolutional neural networks. *Computers & Electrical Engineering*, 78:472–481, 2019.

[San00] O Sangha. Epidemiology of rheumatic diseases. *Rheumatology*, 39(suppl_2):3–12, 2000.

[SC18] William R Sherman and Alan B Craig. *Understanding virtual reality: Interface, application, and design*. Morgan Kaufmann, 2018.

[SCW12] Juan Shan, HD Cheng, and Yuxuan Wang. Completely automated segmentation approach for breast ultrasound images using multiple-domain features. *Ultrasound in medicine & biology*, 38(2):262–275, 2012.

[Sha08] Ariel Shamir. A survey on mesh segmentation techniques. In *Computer graphics forum*, volume 27, pages 1539–1556. Wiley Online Library, 2008.

[SHO+06] AK Scheel, KG A Hermann, S Ohrndorf, C Werner, C Schirmer, J Detert, M Bollow, B Hamm, GA Müller, GR Burmester, et al. Prospective 7 year follow up imaging study comparing radiography, ultrasonography, and magnetic resonance imaging in rheumatoid arthritis finger joints. *Annals of the Rheumatic Diseases*, 65(5):595–600, 2006.

[sit20] Anatomy Learning, 2020.

[SK07] KJ Shanthi and M Sasi Kumar. Skull stripping and automatic segmentation of brain mri using seed growth and threshold techniques. In *2007 International conference on intelligent and advanced systems*, pages 422–426. IEEE, 2007.

[SKH+09] Heiko Seim, Dagmar Kainmueller, Markus Heller, Stefan Zachow, and Hans-Christian Hege. Automatic extraction of anatomical landmarks from medical image data: An evaluation of different methods. In *2009 IEEE International Symposium on Biomedical Imaging: From Nano to Macro*, pages 538–541. IEEE, 2009.

[Spi] Spin questions and answers in mri. `https://mriquestions.com/what-is-spin.html`. (Accessed on 10/02/2020).

[SR17] Gleb Slobodin and Itzhak Rosner. Enthesis as a target organ in rheumatic diseases: an expanding frontier, 2017.

[SRA08] K Subburaj, B Ravi, and MG Agarwal. 3d shape reasoning for identifying anatomical landmarks. *Computer-Aided Design and Applications*, 5(1-4):153–160, 2008.

[SRA09] K Subburaj, Bhallamudi Ravi, and Manish Agarwal. Automated identification of anatomical landmarks on 3d bone models reconstructed from ct scan images. *Computerized Medical Imaging and Graphics*, 33(5):359–368, 2009.

[SRB+15] Gleb Slobodin, Doron Rimar, Nina Boulman, Lisa Kaly, Michael Rozenbaum, Itzhak Rosner, and Majed Odeh. Entheseal involvement in systemic disorders. *Clinical rheumatology*, 34(12):2001–2010, 2015.

[SS00] LG Shapiro and GC Stockman. Computer vision, march 2000, 2000.

[TCB+15] Veronica Tomatis, Marco A Cimmino, Francesca Barbieri, Giulia Troglio, Patrizia Parascandolo, Lorenzo Cesario, Gianni Viano, Loris Vosilla, Marios Pitikakis, Andrea Schiappacasse, et al. A database of segmented mri images of the wrist and the hand in patients with rheumatic diseases. In *International Conference on Image Analysis and Processing*, pages 143–150. Springer, 2015.

[TDVC13] Hedi Tabia, Mohamed Daoudi, Jean-Philippe Vandeborre, and Olivier Colot. A parts-based approach for automatic 3D shape categorization using belief functions. *ACM Trans. Intell. Syst. Technol.*, 4(2):33, 2013.

[TSS15] Rikin Trivedi, Luca Saba, and Jasjit S Suri. *3D imaging technologies in atherosclerosis*. Springer, 2015.

[VGWdB+99] Robert-Jan M Van Geuns, Piotr A Wielopolski, Hein G de Bruin, Benno J Rensing, Peter MA van Ooijen, Marc Hulshoff, Matthijs Oudkerk, and Pim J de Feyter. Basic principles of magnetic resonance imaging. *Progress in cardiovascular diseases*, 42(2):149–156, 1999.

[VP02] Tim Vernon and Daniel Peckham. The benefits of 3d modelling and animation in medical teaching. *Journal of Audiovisual media in Medicine*, 25(4):142–148, 2002.

[WAAV19] Justine Wallyn, Nicolas Anton, Salman Akram, and Thierry F Vandamme. Biomedical imaging: principles, technologies, clinical aspects, contrast agents, limitations and future trends in nanomedicines. *Pharmaceutical research*, 36(6):78, 2019.

[WAvK+12] Y. Wang, S. Asafi, O. van Kaick, H. Zhang, D. Cohen-Or, and B. Chen. Active co-analysis of a set of shapes. *ACM Transactions on Graphics*, 31(6):165:1–165:10, November 2012.

[WCK+14] Moritz C Wurnig, Maurizio Calcagni, David Kenkel, Magdalena Vich, Markus Weiger, Gustav Andreisek, Felix W Wehrli, and Andreas Boss. Characterization of trabecular bone density with ultra-short echo-time mri at 1.5, 3.0 and 7.0 t–comparison with micro-computed tomography. *NMR in Biomedicine*, 27(10):1159–1166, 2014.

[WD19] Lauren H Williams and Trafton Drew. What do we know about volumetric medical image interpretation?: A review of the basic science and medical image perception literatures. *Cognitive research: principles and implications*, 4(1):21, 2019.

[Web15] John G Webster. Strumentazione biomedica, 2015.

[WR06] Stefan Wörz and Karl Rohr. Localization of anatomical point landmarks in 3d medical images by fitting 3d parametric intensity models. *Medical image analysis*, 10(1):41–58, 2006.

[XDH+15] Ning Xue, Michael Doellinger, Charles P Ho, Rachel K Surowiec, and Raphael Schwarz. Automatic detection of anatomical landmarks on the knee joint using mri data. *Journal of Magnetic Resonance Imaging*, 41(1):183–192, 2015.

[YBH+10] Takeshi Yokoo, Won C Bae, Gavin Hamilton, Afshin Karimi, James P Borgstede, Brian C Bowen, Claude B Sirlin, Christine B Chung, John V Crues, William G Bradley, et al. A quantitative approach to sequence and image weighting. *Journal of Computer Assisted Tomography*, 34(3):317–331, 2010.

[YMB77] William A Yasnoff, Jack K Mui, and James W Bacus. Error measures for scene segmentation. *Pattern recognition*, 9(4):217–231, 1977.

[YZY+15] Dong Yang, Shaoting Zhang, Zhennan Yan, Chaowei Tan, Kang Li, and Dimitris Metaxas. Automated anatomical landmark detection ondistal femur surface using convolutional neural network. In *2015 IEEE 12th international symposium on biomedical imaging (ISBI)*, pages 17–21. IEEE, 2015.

[Z+17] Yujin Zhang et al. *Image analysis*. Walter de Gruyter GmbH & Co KG, 2017.

[ZBLR17] Pan Zheng, Bahari Belaton, Iman Yi Liao, and Zainul Ahmad Rajion. A functional pipeline framework for landmark identification on 3d surface extracted from volumetric data. *Plos one*, 12(11):e0187558, 2017.

[ZFG08] Hui Zhang, Jason E Fritts, and Sally A Goldman. Image segmentation evaluation: A survey of unsupervised methods. *computer vision and image understanding*, 110(2):260–280, 2008.

[Zho14] S Kevin Zhou. Discriminative anatomy detection: Classification vs regression. *Pattern Recognition Letters*, 43:25–38, 2014.

[ZYCO10] Jing Zhang, C-H Yan, C-K Chui, and S-H Ong. Fast segmentation of bone in ct images using 3d adaptive thresholding. *Computers in biology and medicine*, 40(2):231–236, 2010.